

Development of New Synthesis Routes for High
Temperature Thermoelectric Materials via Spark Plasma
Sintering Utilizing Solid-State Reaction, Liquid Phase
Sintering, and Gas/Solid Reaction

Son Hyoung-Won

April 2020

Development of New Synthesis Routes for High
Temperature Thermoelectric Materials via Spark Plasma
Sintering Utilizing Solid-State Reaction, Liquid Phase
Sintering, and Gas/Solid Reaction

Son Hyoung-Won

Doctoral Program in Materials Science and Engineering

Submitted to the Graduate School of

Pure and Applied Sciences

in Partial Fulfillment of the Requirements

for the Degree of Doctor of Philosophy in

Engineering

at the

University of Tsukuba

Acknowledgements

First of all I wish to express my deepest gratitude to Prof. Takao Mori for having accepted me into his research group and giving me the opportunity to work on this PhD thesis under his supervision. I would like to thank him for his guidance, suggestions, and encouragements throughout the course of my studies. His continuous support, inspirational suggestions, and many helpful discussions with sharing his incredible scientific knowledge are the cornerstones of this challenging work. I am also grateful to him for developing my writing skill, giving invaluable advices for improving it.

I would like to extend my gratitude to Prof. Yoshikazu Suzuki, Faculty of Pure and Applied Sciences, University of Tsukuba. He gave me the opportunity to study in Japan five years ago, and has continuously helped me greatly as my previous supervisor and present coauthor in experimental and theoretical questions. He introduced me into the ceramic processing area, and gave me special inspirations for reactive sintering technology.

I am also indebted to Prof. Young-Hwan Han. He first introduced me into the research area in undergraduate school, and generously supported and helped me in both research and life. He also helped me with his scientific knowledge about diffusion and sintering.

I wish to acknowledge the members of PhD committee, Prof. Yoshikazu Suzuki, Prof. Seiji Mitani and Prof. Naoki Fukata for their kind advice for the improvement of my PhD thesis.

I would like to thank Dr. Byung-Nam Kim, Material Processing Unit, National Institute for Materials Science. He introduced me into the world of spark plasma sintering and shared his scientific insight generously as a former supervisor at National Institute for Materials Science.

I wish to thank Dr. Quansheng Guo who has helped me as an instructor on thermoelectrics. He gave me many scientific advices, and supported me.

I am sincerely grateful Dr. David Berthebaud, CNRS-Saint Gobain-NIMS, National Institute for Materials Science, for his support and help with sharing his knowledge, scientific inspirations, and experimental experience while learning Rietveld refinement and carrying out boride works. I am thankful his help in the difficult times of my PhD.

I also want to express my thanks to Prof. Kunio Yubuta, Institute of Multidisciplinary Research for Advanced Materials, Tohoku University, for providing beneficial suggestions and supporting TEM observations on boride works. I would like to extent my thanks to Prof. Toetsu Shishido, Institute of Multidisciplinary Research for Advanced Materials, Tohoku University. He gave me many advices with his experience and knowledge for boride works. I wish to thank Keiko Suzuta for her supports with the measurement of specific heat capacities of $Y_xAl_yB_{14}$ ceramics by high temperature DSC.

I would like to express my thanks to Dr. Philipp Sauerschnig, who is a student of our laboratory. He helped me on the study about $YB_{22}C_2N$ as my coauthor, and lessen difficulties in PhD with me.

I would like to Prof. Sukyoung Kim and Prof. Kye Hyun Cho in Korea who gave me the opportunity to come to Japan five years ago. I also wish to thank Prof. Hidehiro Yoshida, Science and Engineering, The University of Tokyo, for his great support in both study and life in Japan.

I also want to thank Dr. Naoki Sato and the other members of our laboratory, postdoctoral researchers and students, who I was able to work with and who created a good laboratory environment.

I would like to thank Erika Arisumi-Guelou, Sayaka Latumeten, Yuki Yoshioka, Xiaoyin Wang and Kyoko Hirosawa for their kind support with the many administrative tasks.

Finally, I am ever grateful to my parents, Yoon Sik Son and Min Ja Oh, and my younger sister InAh Son for their love, support, encouragement, and dedicates throughout my life. They have filled my life with worthwhile and happiness. Without my family, I would not have been able to make this thesis. I would like to thank my family for all this glory.

Son Hyoung-Won

Abstract

Thermoelectric materials are of interest because they can realise the solid state conversion of heat to electricity. The performance of thermoelectric materials is determined by dimensionless figure of merit, $ZT=S^2\sigma T/\kappa$, where S is Seebeck coefficient, σ is electrical conductivity, T is absolute temperature, and κ is thermal conductivity. Hence, thermoelectric materials which exhibit high performances are comprised of high S , high σ , and low κ .

There are various attractive high temperature thermoelectric applications such as the topping cycle for power plants, steelworks, industrial furnaces, and so on. These can potentially have large effect to recover energy. To be used for such applications, the materials first of all have to have robust high temperature stability. In addition, mechanical properties are also critical for success of applications. For instance, at mid-high operational temperature range, the materials in thermoelectric generators are exposed to a thermal stress that can have a negative impact on their efficiency and durability. Suitable material groups for this are refractory ceramics like oxides, nitrides, and borides.

Oxides have been studied most extensively, however, the performance of n-type oxides still needs to be improved compared to p-type. Meanwhile, for borides, investigations have been particularly carried out on such boron icosahedral compounds such as boron carbide, β -rhombohedral boron, $B_{12}As_2$, $RB_{44}Si_2$, RB_{66} , $RAIB_{14}$, MB_6 , R-B-C (N) compounds, and so on. One big issue for the borides for thermoelectric applications is the difficulty of finding matching p-type and n-type compounds. The aforementioned compounds are predominantly p-type, with the exception of certain doped elements into β -boron, $RAIB_{14}$, and the R-B-C (N) compounds. Furthermore, for the synthesis of $RAIB_{14}$ and R-B-C (N) compounds, complex and time consuming processes are required. Densification of these complex borides are an even more difficult problem. For instance, relative densities of $Y_xAl_yB_{14}$ samples prepared by conventional synthesis process exhibited quite low values. For the metal borocarbonitrides, initial spark plasma sintering (SPS) experiments only yielded a maximum ~75% density. Several sintering conditions were tried with some effective sintering aids found, but which were detrimental to the properties.

In this thesis, we report on the first attempt of an n-type thermoelectric $MgTi_2O_5/TiN$ conductive composite, which overcame the traditional trade-off relationship between σ and κ , fully densified p-n controllable polycrystalline $Y_xAl_yB_{14}$, and directly synthesized $YB_{22}C_2N$ without additives for high temperature thermoelectric applications. Rapid and effective synthesis routes for these materials via reactive SPS were also newly developed. The new processes for preparation of $MgTi_2O_5/TiN$ composites, $Y_xAl_yB_{14}$ and $YB_{22}C_2N$ utilize solid-state reaction, liquid phase-assisted sintering, and gas/solid reaction technologies, respectively. These breakthrough techniques are expected to be applicable to the synthesis of other oxide-based composites, higher borides and rare earth borocarbonitrides. Furthermore, it is also expected that the newly developed direct synthesis technique by in-situ nitridation via reactive SPS utilizing N_2 gas/solid reaction could open the door for more accessible synthesis of not only borocarbonitrides but also other nitrides.

Contents

Acknowledgements	I
Abstract	III
Chapter 1 Introduction	1
1.1 Thermoelectricity	1
1.1.1 Background.....	1
1.1.2 Recent trends in thermoelectric materials	3
1.2 Sintering	6
1.2.1 Basic principle of sintering.....	6
1.2.2 Effect of curvature.....	6
1.2.3 Mass transport mechanisms in solid-state sintering.....	10
1.2.4 Stages of sintering during solid-state sintering	13
1.2.5 Liquid phase sintering	15
1.2.6 Sintering mechanism in liquid phase sintering	16
1.2.7 Reactive sintering	17
1.2.8 Spark plasma sintering (SPS)	18
1.3 References	20
Chapter 2 Thermoelectric Properties of MgTi₂O₅/TiN Conductive Composites Synthesized via Reactive Spark Plasma Sintering through Solid-State Reaction	24
2.1 Introduction	24
2.2 Experimental procedure.....	26
2.2.1 Synthesis.....	26
2.2.2 Characterizations	26
2.3 Results and discussion.....	27
2.3.1 Phase identification	27
2.3.2 Thermal properties	30
2.3.3 Microstructure	33
2.3.4 Thermoelectric properties	38
2.4 Summary	44

2.5 References	45
Chapter 3 New Synthesis Route for Complex Borides; Rapid Synthesis of Thermoelectric Yttrium	
Aluminoboride via Liquid-Phase Assisted Reactive Spark Plasma Sintering	47
3.1 Introduction	47
3.2 Experimental procedure.....	49
3.2.1 Synthesis.....	49
3.2.2 Characterizations	49
3.3 Results and discussion.....	51
3.3.1 Phase identification	51
3.3.2 Thermoelectric properties.....	57
3.3.3 Densities and thermal properties	64
3.3.4 Microstructure.....	67
3.3.5 Thermodynamic calculations.....	69
3.3.6 Power factor and ZT.....	71
3.4 Summary	73
3.5 References	74
Chapter 4 Rapid synthesis of thermoelectric YB₂₂C₂N via spark plasma sintering with gas/solid reaction	
technology.....	76
4.1 Introduction	76
4.2 Experimental procedure.....	78
4.2.1 Synthesis.....	78
4.2.2 Characterizations	79
4.3 Results and discussion.....	80
4.3.1 Development of N ₂ gas/solid reaction step	80
4.3.2 Development of reactive sintering process	83
4.3.3 Phase ratio and thermoelectric properties	85
4.4 Summary	88
4.5 References	89
Chapter 5 Conclusion.....	91
List of Publications	93

List of Figures 94

List of Tables 100

Chapter 1

Introduction

1.1 Thermoelectricity

1.1.1 Background

In modern society, fossil fuels including petroleum, coal and natural gas are widely used as primary energy sources in various areas such as industry, transportation, power generation, and so on [1,2]. In comparison to other energy sources, the fossil fuels are relatively cheap, reliable and easy to use. However, the fossil fuels are non-renewable resources, and their deposits are limited. Furthermore, by-products such as fumes, sulfur dioxide, carbon monoxide, nitrogen oxides, carbon dioxide, etc. emitted by combustion of fossil fuels cause environmental degradation and global warming [1,2]. Hence, since the turn of the 20th century, there has been a growing need for developing environmentally friendly and renewable alternative energy such as solar power, wind power, hydroelectric power, geothermal power, biomass, thermoelectric conversion technology, and so on [2,3]. Amongst them, thermoelectric conversion technology can convert waste heat to electricity directly (**Fig. 1.1**), thus a number of researches have been carried out all over the world [4-6].

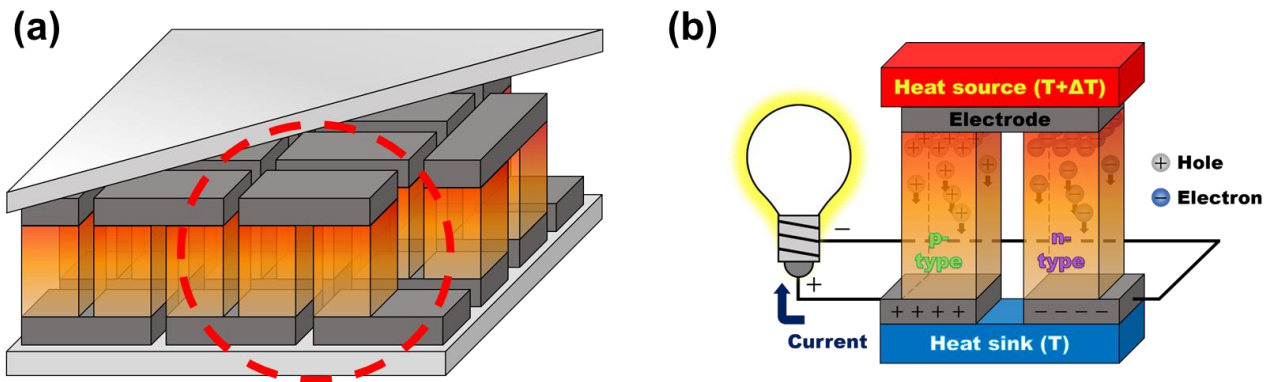


Figure 1.1. Schematic diagram of (a) a thermoelectric generator module and (b) a single thermoelectric couple. The red circle at the thermoelectric generator module indicates the single thermoelectric couple.

The performance of thermoelectric materials is determined by dimensionless figure of merit [5-9],

$$ZT = \frac{S^2 \sigma}{\kappa} T = \frac{S^2 \sigma}{\kappa_e + \kappa_{lat}} T \quad (1.1)$$

where S is Seebeck coefficient, σ is electrical conductivity, κ is thermal conductivity, T is absolute temperature, κ_e is electronic thermal conductivity, and κ_{lat} is lattice thermal conductivity. Thus, thermoelectric materials which exhibit high performances are comprised of large Seebeck coefficient, high electrical conductivity, and low thermal conductivity. These thermoelectric properties are strongly dependent on the charge carrier concentration [5].

Figure 1.2 shows correlations between each thermoelectric property and the charge carrier concentration. For metals or degenerate semiconductors, the Seebeck coefficient is determined by [5]:

$$S = \frac{8\pi^2 k^2}{3eh^2} m^* T \left(\frac{\pi}{3n}\right)^{2/3} \quad (1.2)$$

where k is Boltzmann constant, e is carrier charge, h is Planck constant, m^* is the effective mass of the carrier, n is the carrier concentration. It can be seen from Eq. 1.2 that the Seebeck coefficient is proportional to m^* , while inversely proportional to the $2/3$ power of n .

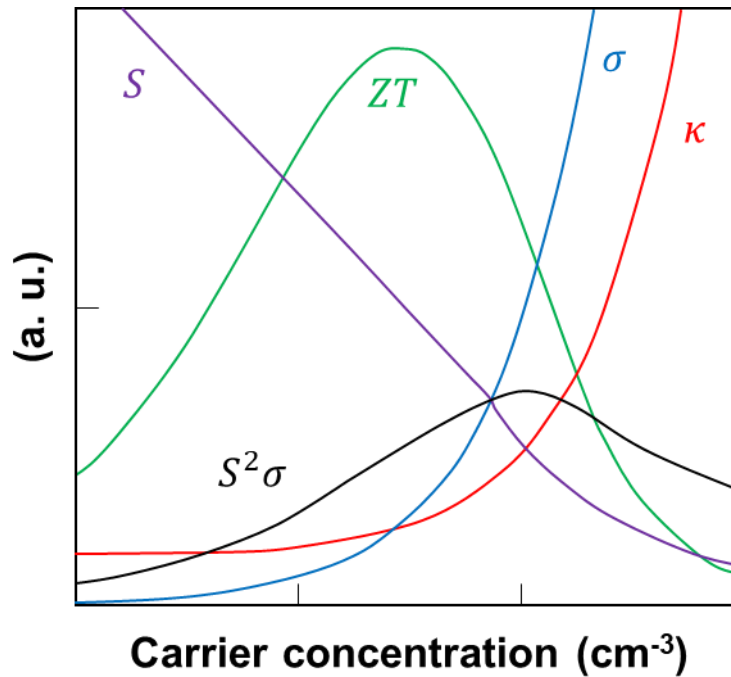


Figure 1.2. Correlations between thermoelectric properties and the charge carrier concentration. Copyright Nature Publishing Group [5].

Meanwhile, thermal conductivity is composed of two terms; electronic thermal conductivity (κ_e) and lattice thermal conductivity (κ_{lat}), as shown in Eq. 1.1. Herein, the electronic thermal conductivity is related to the electrical conductivity:

$$\kappa_e = L\sigma T \quad (1.3)$$

where L is the Lorenz factor, which can vary with carrier concentration. Also, the electrical conductivity is given by [5]:

$$\sigma = ne\mu \quad (1.4)$$

where μ is the carrier mobility. Substituting Eq. 1.4 into Eq. 1.3 yields:

$$\kappa_e = L\sigma T = ne\mu LT \quad (1.5)$$

Therefore, when the charge carrier concentration increases, the electrical conductivity is improved, whereas thermal conductivity increases and Seebeck coefficient decreases. To overcome these trade-off relationships in thermoelectrics, new approaches are required.

1.1.2 Recent trends in thermoelectric materials

Recently, developing energy harvesting technologies to power IoT (Internet of Things) sensors and devices is an important topic [10,11]. For such targets, organic, organic-inorganic hybrid, and inorganic materials are being developed to use near room temperature as flexible or micro-sized thermoelectric power generation modules [12,13]. On the other hand, at the other extreme of very high temperatures above 1000 K, there are various attractive high temperature thermoelectric applications such as topping cycle for power plants, steelworks, industrial furnaces, and so on [14-18]. To be used for such applications, the materials need to possess robust high temperature stability. In addition, mechanical properties are also critical for success of applications. For instance, at mid-high operational temperature range, the materials in thermoelectric generators are exposed to a thermal stress that can have a negative impact on their efficiency and durability [19]. Suitable material groups for this are refractory ceramics like oxides [20-28], nitrides [29,30], and borides [31-52].

Figure 1.3 shows literature ZT values of representative high temperature thermoelectric materials. Oxides, for instance, ZnO-based, $\text{Na}_x\text{CoO}_{2-\delta}$, SrTiO_3 -based and others have been studied most extensively [20-26], however, the performance of n-type oxides still needs to be improved compared to p-type. Meanwhile, for borides, investigations have been particularly carried out on such boron icosahedral compounds such as boron carbide [31-35], β -rhombohedral boron [36,37], B_{12}As_2 [38,39], $\text{RB}_{44}\text{Si}_2$ [40,41], RB_{66} [42,43], MB_6 [44,45], RAlB_{14} [46-49], R-B-C (N) compounds [50-53], and so on.

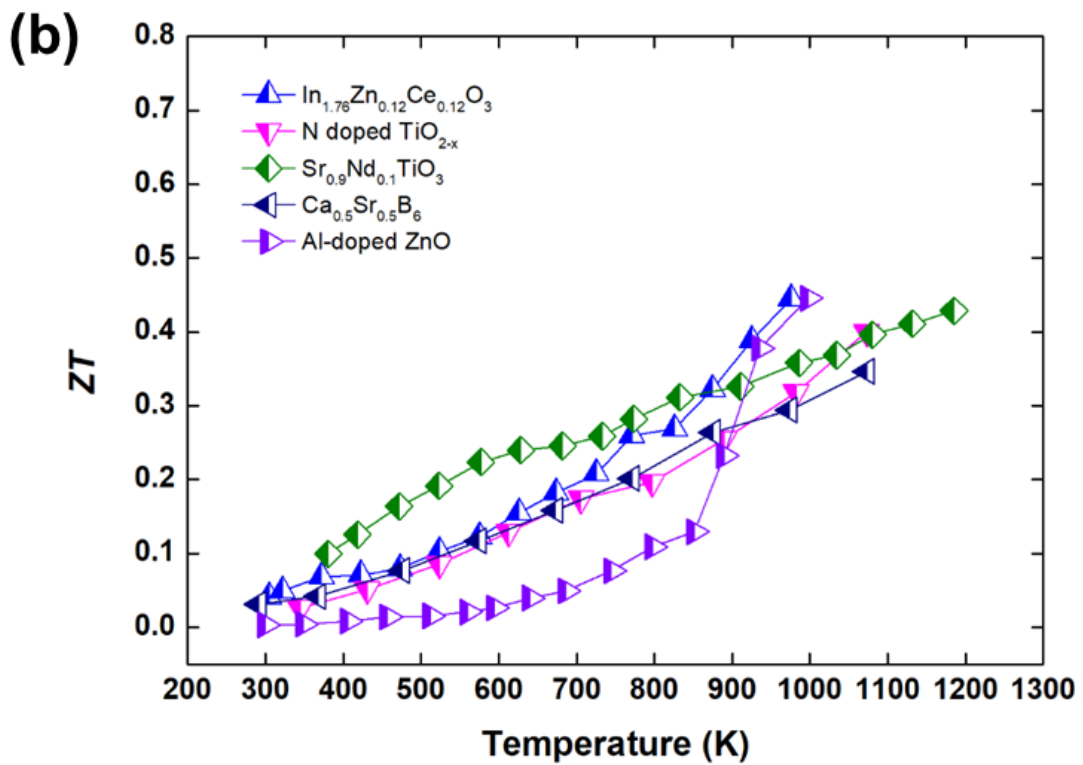
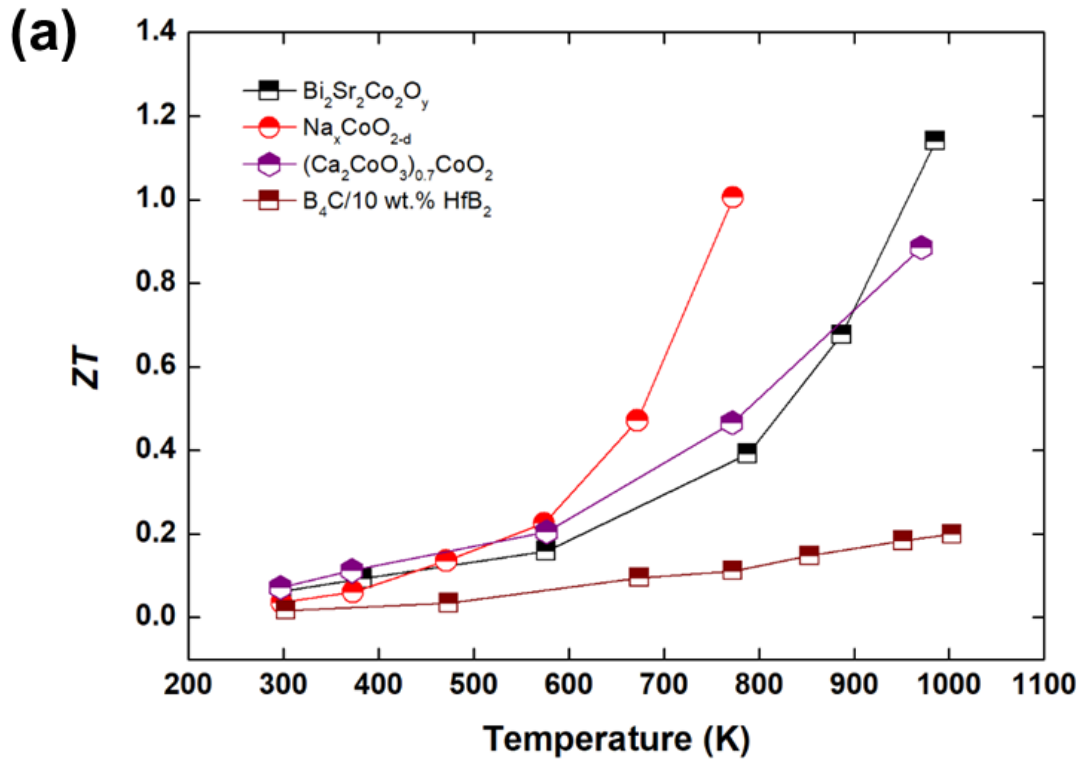


Figure 1.3. Literature ZT values of representative (a) p-type and (b) n-type high temperature thermoelectric materials [20-26,35,44].

One big issue for the borides for thermoelectric applications is the difficulty of finding matching p-type and n-type compounds. The aforementioned compounds are predominantly p-type, with the exception of certain doped elements into β -boron, $RAIB_{14}$, and the R-B-C (N) compounds [46-50]. Furthermore, for the synthesis of $RAIB_{14}$ and R-B-C (N) compounds, complex and time consuming processes are required [46-53]. Densification of these complex borides are an even more difficult problem. For instance, relative densities of $Y_xAl_yB_{14}$ samples prepared by conventional synthesis process exhibited quite low values (71.1-89.4%) [43]. For the metal borocarbonitrides, initial spark plasma sintering (SPS) experiments only yielded a maximum ~75% density [53]. Several sintering conditions were tried with some effective sintering aids found, but which were detrimental to the properties [51,54]. This synthesis issue can be said to be a problem for many complex borides discovered with interesting electrical, magnetic, thermoelectric, and mechanical properties [55,56]. It is thus needed to develop a new, simple and reasonable synthesis process.

1.2 Sintering

1.2.1 Basic principle of sintering

Sintering is the process in which individual particles in powder materials bond each other and produce a consolidated component [57]. Basically, sintering is occurred by a mass transfer in materials below their melting point. However, in many actual cases, sintering process often accompanies a formation of a partial liquid phase, which could be caused by a partial compositional inhomogeneity, presence of multiple components, contamination, additives, and so on [58-60]. The sintering occurred without and with a liquid phase are called solid-state sintering and liquid phase sintering, respectively [58].

The driving force for the sintering is lowering the total free energy in the system by lowering excessive energy such as surface free energy and grain boundary energy with decreasing surface area [57]. In the system including multiple phases such as composites, lowering an interfacial energy also can be the driving force for sintering [61]. Thus, the driving force for the sintering can be expressed as follows:

$$\Delta G_T = \Delta G_v + \Delta G_s + \Delta G_{gb} + \Delta G_i \quad (1.6)$$

where ΔG_T is the total free energy, ΔG_v is the volume free energy, ΔG_s is the surface free energy, ΔG_{gb} is the grain boundary free energy, and ΔG_i is the interfacial free energy in the system. The surface area per unit volume increases with decreasing particle size. The total contact areas amongst particles, which act as paths for the mass transfer, also increases with decreasing particle size if the particles are well packed and not severely agglomerated, thereby the fine particles can be more easily sintered than coarse particles.

1.2.2 Effect of curvature

Sintering is driven by chemical potential gradient [62]. At elevated temperature, atoms and ions diffuse from a high chemical potential region to a low chemical potential region if the temperature is high enough to overcome an activation energy for diffusion. The chemical potential is dependent on the curvature of a surface. To understand the effect of curvature, several models can be considered.

Figure 1.4 shows a gas bubble with radius r surrounded by a fluid. The gas bubble takes a spherical shape due to its surface tension. As a result, the surface tension applied to the spherical bubble reduces its surface area and volume, while increases its internal pressure as ΔP [63]. At the equilibrium, the work done on the system, dW , is:

$$dW = \Delta P dV - \gamma_s dA = \Delta P 4\pi r^2 dr - \gamma_s 8\pi r dr = 0 \quad (1.7)$$

where γ_s is the surface energy, and dV and dA are the volume change and surface area change, respectively.

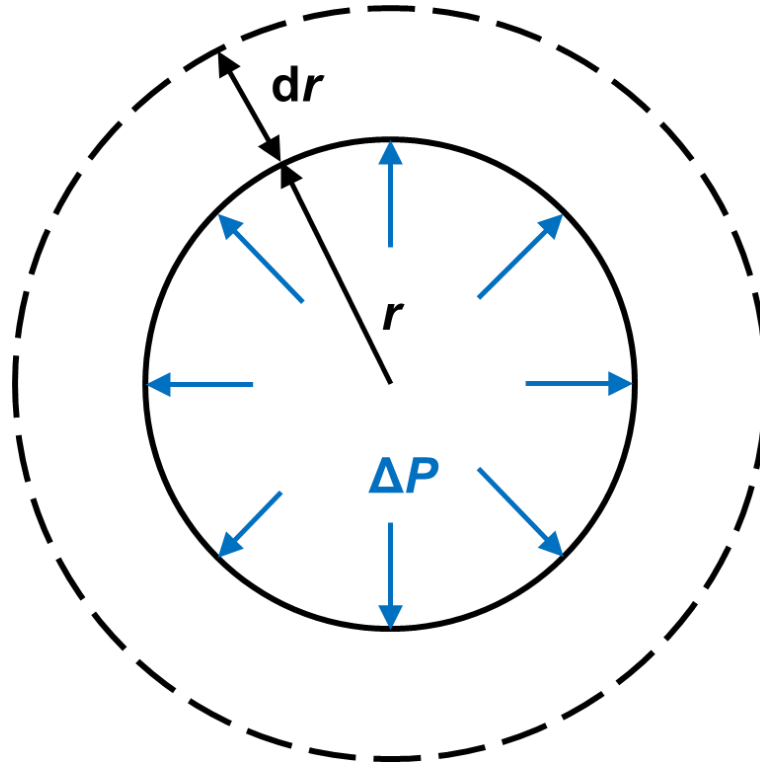


Figure 1.4. The model for calculating the pressure in a bubble produced by surface tension and positive surface curvature.

Then, ΔP is calculated as:

$$\Delta P = \frac{2\gamma_s}{r} \quad (1.8)$$

This equation is known as Young-Laplace equation [64]. The Eq. 1.8 can be generalized for a curved surface which has two principal radii of curvature, r_1 and r_2 , as follows:

$$\Delta P = \gamma_s \left(\frac{1}{r_1} + \frac{1}{r_2} \right) \quad (1.9)$$

For an ideal sphere, r_1 is equal to r_2 . From Eq. 1.9, we can know that a bubble with a smaller r has a higher ΔP than that with a larger r . Therefore, when two bubbles of different sizes are contacted each other, the large bubble will be grown by consuming the smaller bubble, as shown in **Fig. 1.5**. During sintering, a similar stress associated with a curvature is also applied to the surface of particles. The mechanical stress, σ , produced on the curved surface of each particle by their surface tension is termed as sintering stress (or sintering potential), and expressed as [62,65]:

$$\sigma = \gamma_s \left(\frac{1}{r_1} + \frac{1}{r_2} \right) \quad (1.10)$$

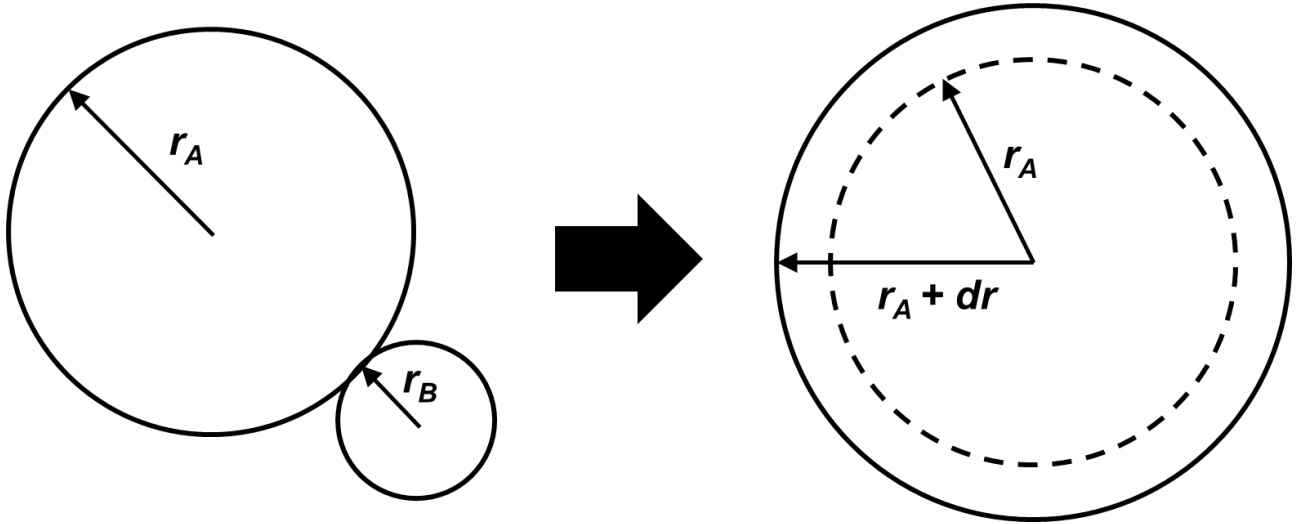


Figure 1.5. The model for bubble growth. Each bubble is ideally spherical, and $r_A > r_B$.

Then, let us consider the chemical potential of atoms under a curved surface. **Figure 1.6** shows the conventional model which has been used to derive the chemical potential [62,64,65]. The model is composed of two surfaces; a flat surface of a semi-infinite solid and a curved surface of a spherical solid particle with a radius r . In addition, there is only one type of mobile particle.

If it is assumed that atoms move from the flat surface of the semi-infinite solid to the spherical particle, the particle will be grown, and thereby the change in volume of the particle, dV , can be considered as the product of the atomic volume, Ω , and a number of transferred atoms, dN . Thus:

$$dV = 4\pi r^2 dr = \Omega dN \quad (1.11)$$

Meanwhile, at equilibrium, the energy change caused by the addition of atoms to the particle is equal to the energy change caused by increasing in the surface area. Thus, the chemical potential change brought by the transfer of an atom is given by [64,65]:

$$\Delta\mu dN = (\mu_c - \mu_0)dN = \gamma_s dA = \gamma_s 8\pi r dr \quad (1.12)$$

where μ_c and μ_0 are the chemical potential on the particle surface and on the flat surface of the solid, respectively. Substituting Eq. 1.12 into Eq. 1.11, we can obtain:

$$\Delta\mu = \frac{2\gamma_s\Omega}{r} \quad (1.13)$$

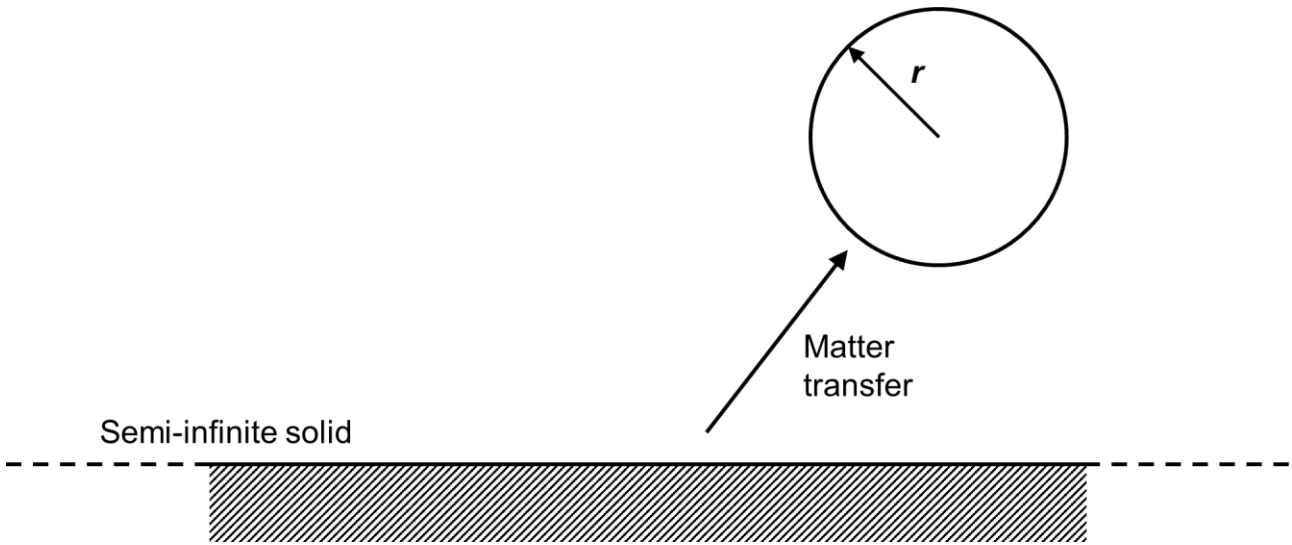


Figure 1.6. The conventional model which has been used to derive the chemical potential of atoms under a curved surface [62,64,65]. In this model, atoms move from the flat surface of a semi-infinite solid to the curved surface of a spherical solid particle with a radius r .

Consequently, the correlation between the sintering potential and chemical potential of atoms under a curved surface is established as follows:

$$\sigma = \frac{\Delta\mu}{\Omega} \quad (1.14)$$

For a convex surface, the curvature is positive ($r > 0$), and the chemical potential of atoms on such surface is higher than that on the flat surface. Thus, the transfer of atoms from the flat surface to the convex surface in aforementioned model results in an increase of chemical potential ($\Delta\mu > 0$). On the other hand, a transfer of atoms from the flat surface to a concave surface, which possesses a negative curvature ($r < 0$), results in a decrease of chemical potential ($\Delta\mu < 0$). Therefore, when a solid has both convex and concave surfaces, the atoms under a convex surface move to a concave surface at elevated temperature, and hence the both of surfaces will be changed to flat surface ultimately.

1.2.3 Mass transport mechanisms in solid-state sintering

During solid-state sintering, atoms and/or ions diffuse from a high chemical potential region to a low chemical potential region through several paths. The mass transport can be broadly classified into two types: surface transport and bulk transport. **Figure 1.7** gives the seven common possible sintering mechanisms in solid-state sintering [62,66,67].

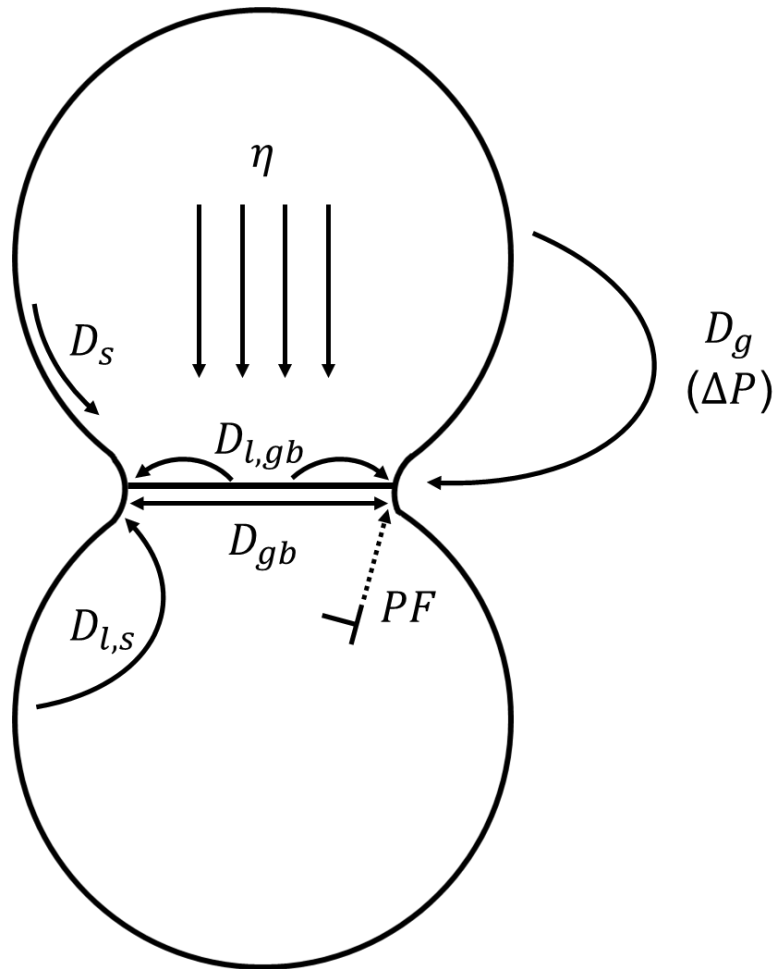


Figure 1.7. The seven common possible sintering mechanisms in solid-state sintering. Herein, D_g , D_s , D_{gb} , $D_{l,gb}$, $D_{l,s}$, η , and PF indicate evaporation-condensation, surface diffusion, grain boundary diffusion, lattice diffusion from grain boundary, lattice diffusion from surface, viscous flow, and plastic flow, respectively [62,66,67].

All mechanisms lead to neck growth. However, the surface transport results in coarsening without densification, whereas the bulk transport results in densification. Evaporation-condensation, surface diffusion, lattice diffusion from the surface to neck mechanisms are classified as the surface transport. Evaporation-condensation is occurred

by a difference of vapor pressure between the surface and neck regions. From the Kelvin equation, the vapor pressure of a curved surface is given by [63,64]:

$$\ln \frac{P}{P_0} = \frac{2V\gamma_s}{rRT} \quad (1.15)$$

Herein, P is the vapor pressure on the curved surface, P_0 is the vapor pressure on the flat surface, V is the molar volume, γ_s is the surface free energy, r is the radius of curvature, R is gas constant, and T is absolute temperature.

Since the convex surface has a positive radius ($r > 0$), the vapor pressure on the convex surface is higher than P_0 . On the other hand, the concave surface has a negative radius ($r < 0$), and hence the vapor pressure on the concave surface is lower than P_0 . Therefore, during sintering, the atoms on the surface of the particle are evaporated, and then condensed on the neck region.

Surface diffusion is occurred by the motion of atoms on the surface of the particle. They move along the surface, and then finally settle in the neck region. The surface diffusion is a predominant mechanism at low temperature because the contribution of the surface free energy ($\gamma_s dA$) is the most significant. It also requires the smallest activation energy compared to other mass transport processes [58,64].

Meanwhile, grain boundary diffusion, lattice diffusion from the grain boundary to neck, viscous flow, and plastic flow are classified as the bulk transport. For grain boundary diffusion, atoms on a flat grain boundary possess higher chemical potential than those on a neck region. Therefore, the atoms move from grain boundary to the neck region through grain boundary to reduce the total energy of the system, as a result, densification is occurred by consuming inside atoms [68]. In general, grain boundary diffusion is the dominant mechanism at intermediate temperature because the contribution of the grain boundary free energy becomes more significant than the surface free energy.

At high temperature, the surface area and grain boundary area decrease, then the lattice diffusion becomes the dominant mass transport mechanism. Two types of lattice diffusion mechanisms are suggested; 1) atoms and/or ions on the surface move to the neck region through volume ($D_{l,s}$), and 2) vacancies move from the neck to the grain boundary ($D_{l,gb}$). Both mechanisms are also originated from the chemical potential distribution and sintering stress.

The vacancy concentration, C , is dependent on the curvature as follows [58]:

$$C = C_0 \left[1 - \frac{\gamma_s \Omega}{kT} \right] \left(\frac{1}{r_1} + \frac{1}{r_2} \right) \quad (1.16)$$

where k is Boltzmann constant, and C_0 is an equilibrium vacancy concentration. The vacancy concentration increases with decreasing radius of a concave surface. Furthermore, the vacancy concentration under a concave surface is higher than the equilibrium vacancy concentration, while that under a convex surface is lower than the equilibrium vacancy concentration, as shown in **Fig. 1.8**.

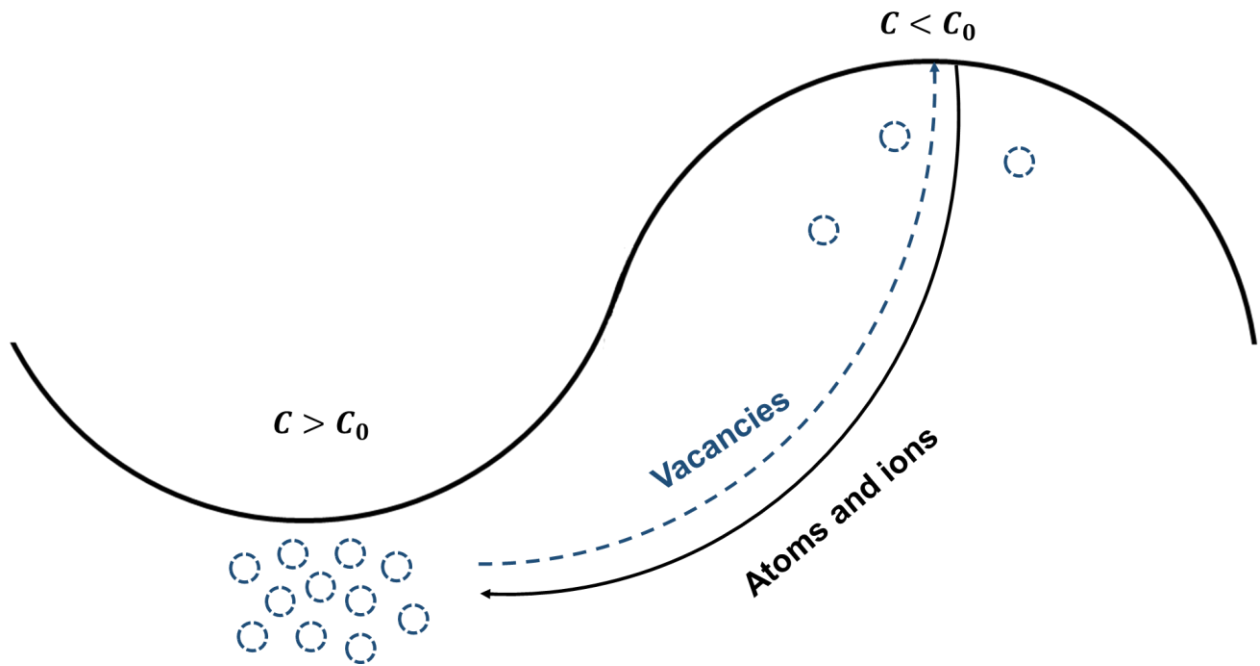


Figure 1.8. Schematic diagram of vacancy concentrations under the convex and concave surfaces. The blue and black arrows indicate vacancy flow, and diffusion of atoms and ions, respectively.

Due to the vacancy concentration gradient induced by the curvatures, the vacancies flow from the neck region to the particle surface through lattice with exchanging their positions with atoms and/or ions during sintering. However, as aforementioned, this process does not result in the densification since the distance between two particles are not changed [69]. On the contrary, when the lattice diffusion is occurred from grain boundary, the particles are closed to each other, and thus it leads to the densification [68,69].

Viscous flow is occurred when amorphous materials are sintered above its glass transition point. It is also possible to be occurred when a liquid phase is positioned at grain boundaries [58,64]. Meanwhile, plastic flow is occurred when the powders are compacted, which have high dislocation density. It is considered that dislocations act as one of various vacancy sinks. Densification behavior in this mechanism is proceeded by dislocation glide-climb [67]. The plastic flow is dominantly occurred in early (and intermediate) stages of sintering, which will be described in the next section. The correlations between each mass transport mechanism and densification behavior in solid-state sintering are summarized in **Table 1.1**.

Table 1.1. The correlations between each mass transport mechanism and densification behavior in solid-state sintering. The routes for each mass transport mechanism are illustrated in **Fig. 1.7**.

Mass transport mechanisms	Routes	Classifications	Densification behavior
Evaporation-condensation	D_g	Surface transport	No
Surface diffusion	D_s	Surface transport	No
Grain boundary diffusion	D_{gb}	Bulk transport	Yes
Lattice diffusion from grain boundary	$D_{l,gb}$	Bulk transport	Yes
Lattice diffusion from surface	$D_{l,s}$	Surface transport	No
Viscous flow	η	Bulk transport	Yes
Plastic flow	PF	Bulk transport	Yes

1.2.4 Stages of sintering during solid-state sintering

The whole stages of sintering are divided into three stages based on the geometrical evolution of microstructure during the densification process; 1) initial stage, 2) intermediate stage and 3) final stage [57,58,70]. **Figure 1.9** shows the schematic diagram for stages of sintering. At the initial stage, necks are forming at the contact points between adjacent particles. The dominant mass transport mechanism during the early stage for neck growth is usually surface diffusion.

At the intermediate stage, the necks are growing with time, and densification is proceeded. Most of shrinkage is obtained during the intermediate state. These processes are driven by the chemical potential gradient generated from the different curvatures, as discussed in *section 1.2.3*. The pore channels are three dimensionally interconnected, and grain boundaries are connected amongst open pores. In general, the dominant mass transport mechanisms accompanying densification during the intermediate stage are grain boundary diffusion and lattice diffusion from grain boundary. Surface diffusion and lattice diffusion from surface also can be occurred, but these do not contribute to the densification process, as described in *section 1.2.3*. For fine grains at low and moderate temperature, densification is dominantly proceeded by grain boundary diffusion, while for coarse grain at high temperature, densification is mainly proceeded by lattice diffusion. Since pores are still opened, they can be eliminated during intermediate stage.

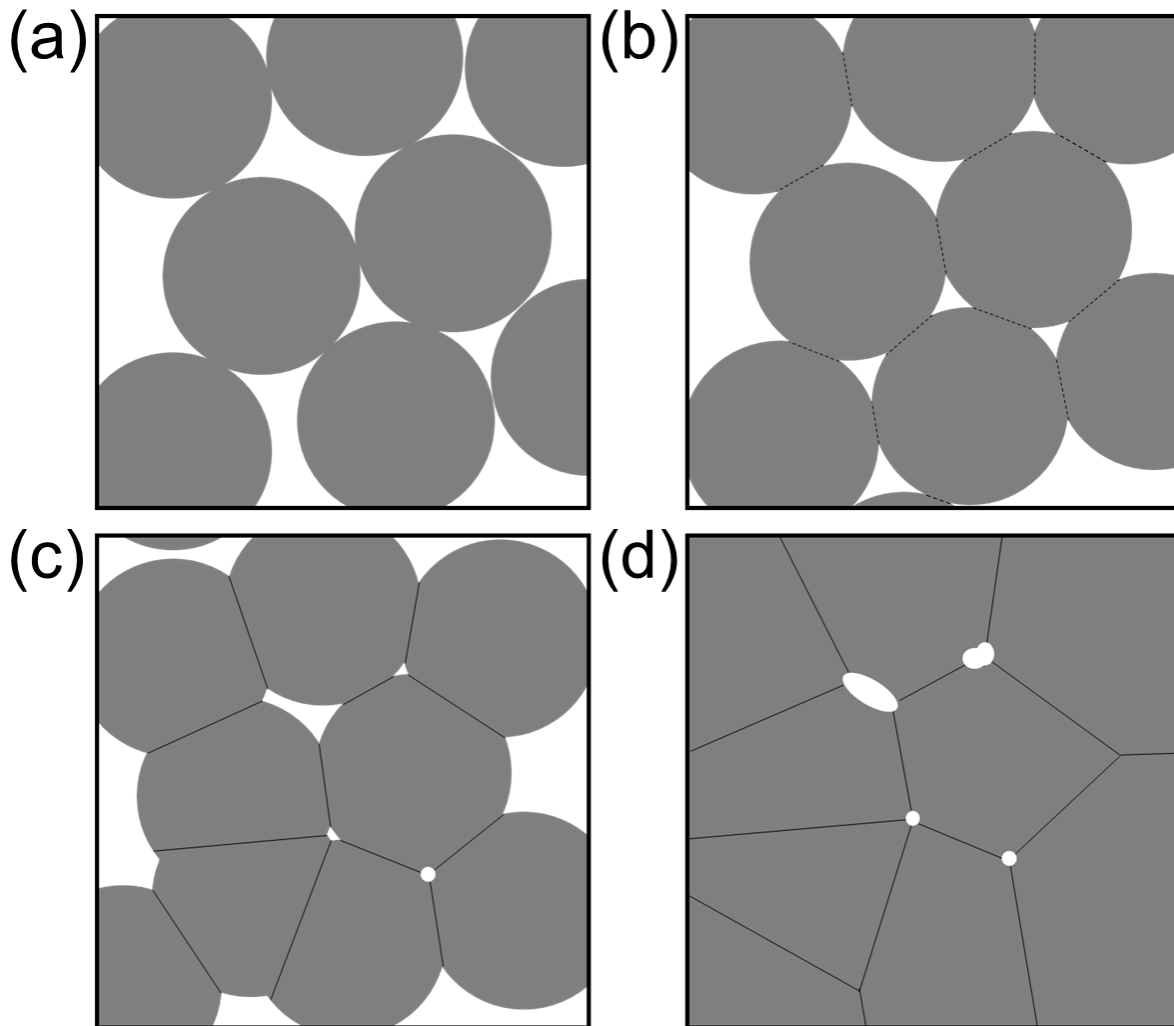


Figure 1.9. Schematic diagram for stages of sintering; (a) packed particles before sintering, (b) initial stage, (c) intermediate stage, and (d) final stage [57,58,70].

At the final stage, the pores are closed or isolated, and grains are growing to reduce grain boundary energy. The isolated pores are pre-dominantly positioned at grain boundaries and/or triple junctions to reduce the surface energy. The pores at grain boundaries and triple junctions form special shape with the equilibrium dihedral angle as shown in **Fig. 1.10**, which is a result of a balance between grain boundary energy and solid-vapor interfacial energy [58]. The pores shrink until the time when the inner pressure of the pore becomes equal to ΔP .

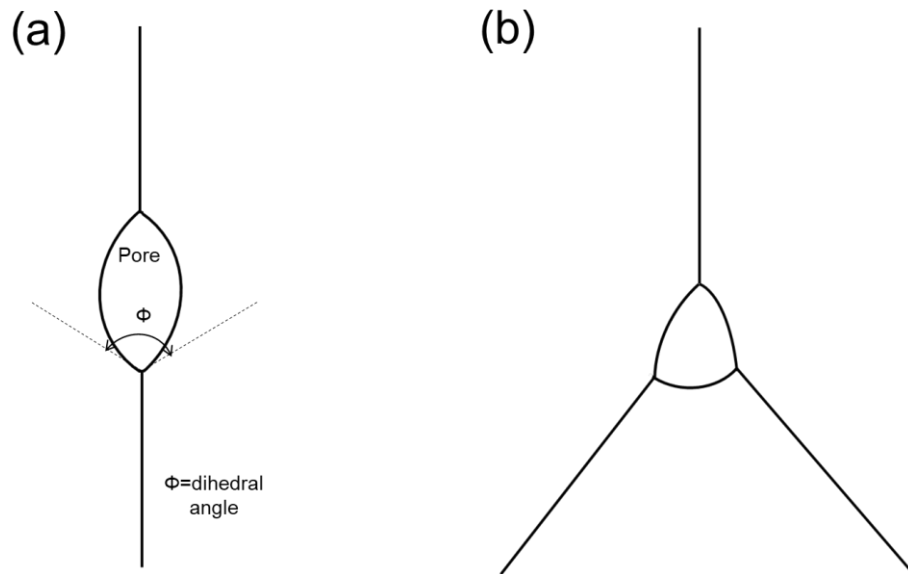


Figure 1.10. Schematic diagram of isolated pores positioned at (a) grain boundary, and (b) triple junction [58].

1.2.5 Liquid phase sintering

As mentioned in *section 1.2.1*, sintering process often accompanies a formation of a partial liquid phase. The presence of the liquid phase formed during sintering significantly accelerates diffusion rates, and thus the liquid phase sintering techniques give short sintering times or lower sintering temperatures, or both [58,60]. For liquid phase sintering, the most important point is wetting property. Good wetting provides a capillary force for particles, which pulls the grains together, as a result, the densification behavior can be additionally accelerated. From these attractive advantages, liquid phase sintering is widely applied for sintering of materials possessing poor sinterability.

In real systems, the microstructure consists of solid, liquid, and gas phases; where the component of the gas phase depends on the sintering atmosphere. The wetting property is associated with the balance amongst solid-gas interfacial energy (γ_{sg}), solid-liquid interfacial energy (γ_{sl}), and liquid-gas interfacial energy (γ_{lg}), and hence for liquid phase sintering, three interfacial energies must be considered. **Figure 1.11** shows two droplets of different liquids on a solid surface with contact angle (wetting angle) [58,60].

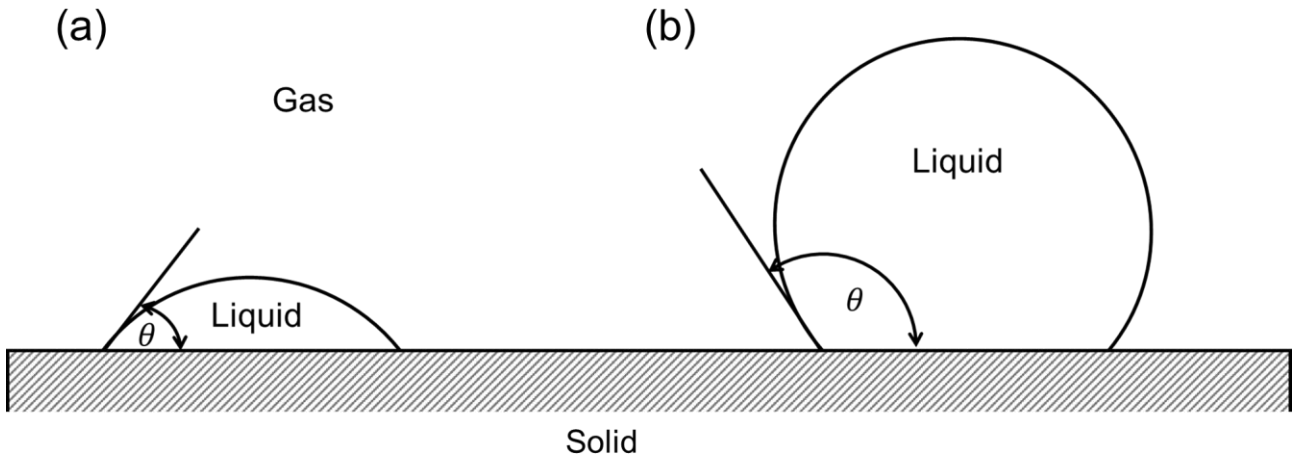


Figure 1.11. The wetting behavior for two droplets of different liquids on a horizontal solid surface with contact angle θ ; (a) good wetting with low θ , and (b) poor wetting with high θ [58,60].

On the horizontal plane, the wetting angle, θ , is defined as:

$$\gamma_{sg} = \gamma_{sl} + \gamma_{lg} \cos\theta \quad (1.17)$$

A low wetting angle induces the droplet spreading over the solid surface, whereas a large angle makes the droplet retreat from the solid surface. This indicates that the small θ is favorable for liquid phase sintering. In addition, an appreciable solubility for the solid and low viscosity are also important for good wetting and rapid matter transport through the liquid, respectively.

1.2.6 Sintering mechanism in liquid phase sintering

The main mechanism in liquid phase sintering is dissolution-precipitation, but the evolution of the microstructure during liquid phase sintering takes place in several steps; preliquid stage, incipient liquid formation, solution-precipitation, and final stage [60]. A model for liquid phase sintering is shown in **Fig. 1.12**.

At the preliquid stage, the temperature is lower than melting point of an additive, and necks are formed at the contacted points between adjacent particles. This process is equivalent to an initial stage of solid-state sintering. When the temperature is over the melting point of additive during heating process, the liquid phase is formed. The liquid phase wets the surface of particles, and spreads to fill pores. This process induces a particle rearrangement phenomenon, which forces the solid grains pack to a higher coordination.

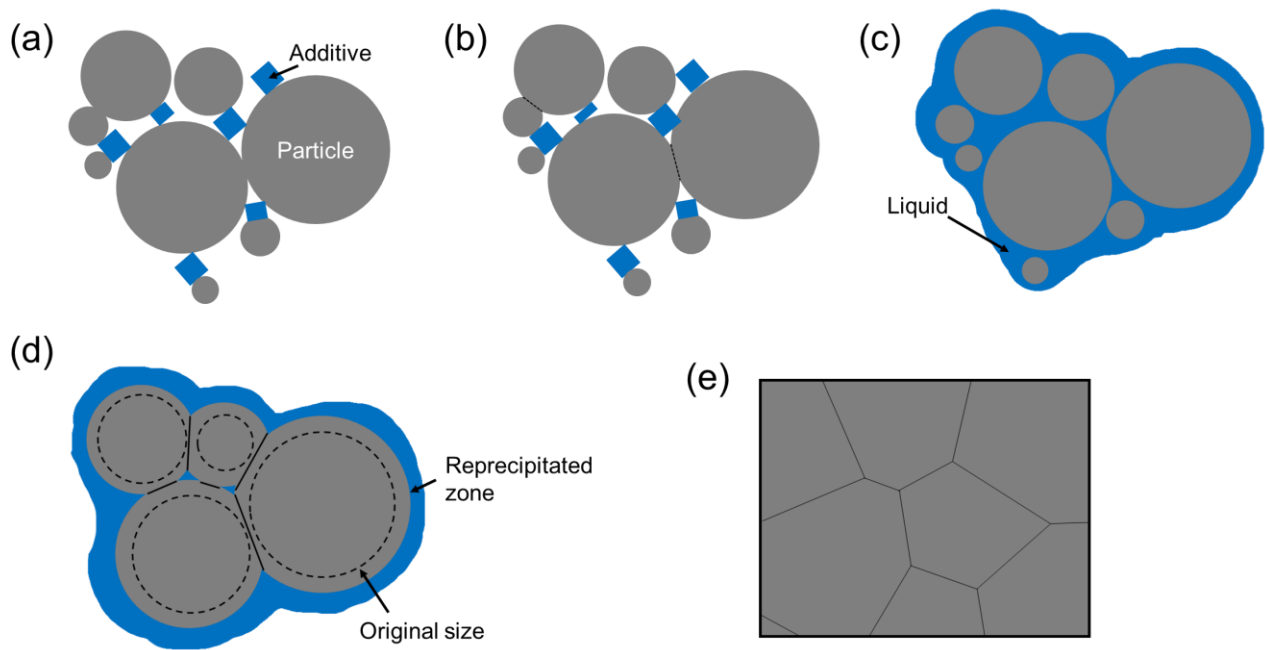


Figure 1.12. Simple model for the evolution of the microstructure during liquid phase sintering; (a) packed mixtures before sintering, (b) preliquid stage, (c) incipient liquid formation, (d) solution-precipitation, and (e) final stage. For this model, it is assumed that 1) the liquid phase was completely removed during sintering, 2) the sintered body is fully densified, and 3) the additive has lower melting point than particles.

The dissolution-precipitation is occurred when the material is soluble in the liquid phase. The dissolution of solid process is preferential from higher energy regions such as convex points, small grains, etc. The dissolved atoms are diffusing via liquid, and precipitated onto concave regions or larger grains. The final stage corresponds to connected grains with liquid filled in the space amongst grains. Grain growth continues until the microstructure is fully densified, or inner pressure of gas trapped in the pores becomes equal to ΔP . By controlling the sintering atmosphere and volume fraction of liquid phase formed by sintering additive, it is possible to obtain fully densified structure.

1.2.7 Reactive sintering

Reactive sintering is one of the sintering techniques, which can synthesize final products by carrying out single or multiple reactions during sintering with using unreacted raw materials. In the conventional method, the starting materials are synthesized by heat treatments (or sintering) at the reaction temperature, and then pulverized by milling process such as planetary ball milling, etc.

However, this process results in contamination in the synthesis materials, and moreover, the sinterability is deteriorated due to lowering driving force originated from their non-spherical shape and coarsening of average

particle size. In contrast, reactive sintering does not cause deterioration in sinterability because it can skip the pre-synthesis and pulverization processes. It also has other advantages such as effective sintering and forming porous structure using chemical reaction during sintering [71].

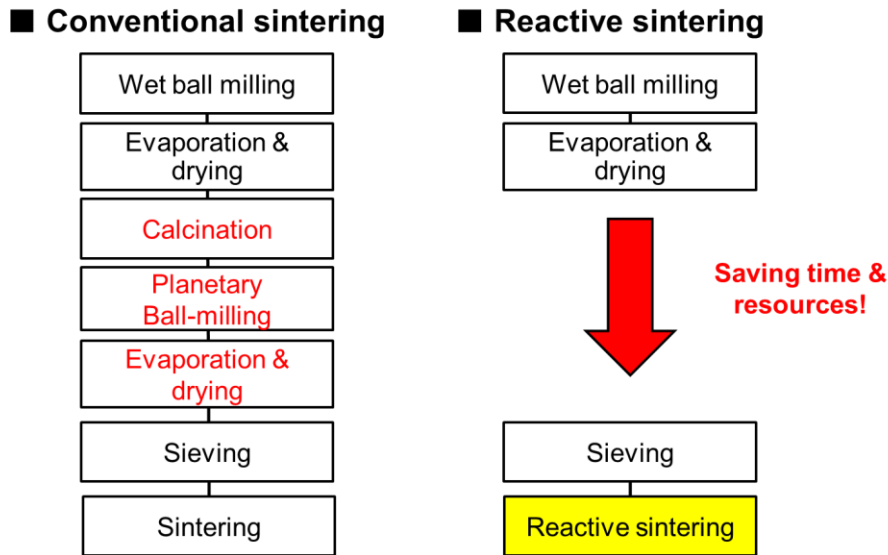


Figure 1.13. Flow chart of whole processes of conventional sintering (left) and reactive sintering (right).

1.2.8 Spark plasma sintering (SPS)

Spark plasma sintering (SPS) is one of the advanced sintering techniques. The SPS machine is composed of a vacuum chamber, DC power supplies, vacuum pumping system, top and bottom electrodes, pressing system, water circulation system, a gas inlet system, a thermocouple, and an external IR pyrometer (**Fig. 1.14**) [72]. In practice, the powders are poured into a die, such as a graphite, WC, SiC, etc. [73], and then heated by pulsed DC under a uniaxial pressure. During heating, the pulsed DC is passing through the electrode and die. In appropriate cases, the current can also be passing through the powder compact.

Compared to conventional sintering techniques, the application of both pressure and electric field during SPS enables rapid heating ($\sim 200^\circ\text{C}/\text{min}$), short sintering time, surface refining, and densification at low temperatures. These features of SPS can suppress grain growth during sintering to yield small grain sizes for improved mechanical properties [72,74-76]. For a sintering atmosphere, Ar gas, N_2 gas, low or high level vacuum can be used. It is selected with considering materials and objective of sintering.

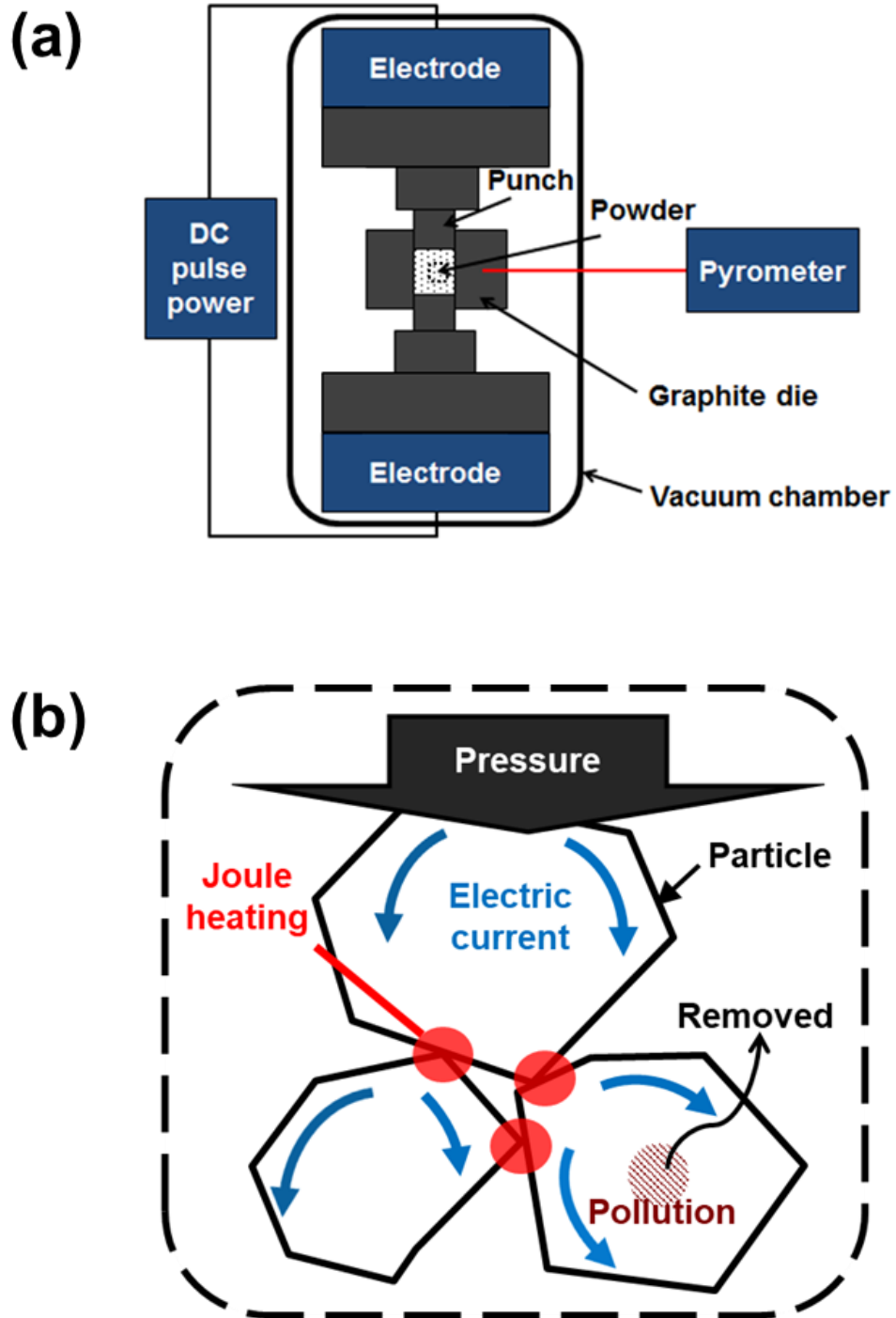


Figure 1.14. Schematic diagram of (a) SPS machine and (b) mechanism during SPS.

1.3 References

- [1] E. Worrell, L. Bernstein, J. Roy, L. Price, J. Harnisch, *Energ. Effic.*, **2** (2009) 109-123.
- [2] N. Abas, A. Kalair, N. Khan, *Futures*, **69** (2015) 31-49.
- [3] J. Mohtasham, *Energy Procedia*, **74** (2015) 1289-1297.
- [4] X. Zhang, L.-D. Zhao, *J. Materiomics*, **1** (2015) 92-105.
- [5] G.J. Snyder, in: D.M. Rowe (Ed.), *Thermoelectrics Handbook: Macro to Nano*, CRC Taylor and Francis (2006) 9-1-26.
- [6] T. Mori, *Small*, **13** (2017) 1702013.
- [7] J. Mao, Z. Liu, J. Zhou, H. Zhu, Q. Zhang, G. Chen, Z. Ren, *Adv. Phys.*, **67** (2018) 69-147.
- [8] J.-B. Vaney, S.A. Yamini, H. Takaki, K. Kobayashi, N. Kobayashi, T. Mori, *Mater. Today Phys.*, **9** (2019) 100090.
- [9] N. Tsujii, A. Nishide, J. Hayakawa, T. Mori, *Sci. Adv.*, **5** (2019) eaat5935.
- [10] T. Mori, S. Priya, *MRS Bull.*, **43** (2018) 176-180.
- [11] H. Akinaga, H. Fujita, M. Mizuguchi, T. Mori, *Sci. Tech. Adv. Mater.*, **19** (2018) 563-544.
- [12] R. Tian, C. Wan, N. Hayashi, T. Aoi, K. Koumoto, *MRS Bull.*, **43** (2018) 193-198.
- [13] I. Petsagkourakis, K. Tybrandt, X. Crispin, I. Ohkubo, N. Satoh, T. Mori, *Sci. Tech. Adv. Mater.*, **19** (2018) 836-862.
- [14] T. Mori, *JOM*, **68** (2016) 2673-2679.
- [15] K. Yazawa, Y.R. Koh, A. Shakouri, *Appl. Energy.*, **109** (2013) 1-9.
- [16] K. Yazawa, A. Shakouri, *Scr. Mater.*, **111** (2016) 58-63.
- [17] T. Kuroki, K. Kabeya, K. Makino, H. Kaibe, H. Hachiuma, A. Fujibayashi, Waste heat recovery in steelworks using a thermoelectric generator, in: A. Amaldi, F. Tang (Eds.), *Proceedings of the 11th European Conference on Thermoelectrics: ETC 2013*, Springer (2014) 143-149.
- [18] V. Andrei, K. Bethke, K. Rademann, *Energy Environ. Sci.*, **9** (2016) 1528-1532.
- [19] T. Dahal, S. Gahlawat, Q. Jie, K. Dahal, Y. Lan, K. White, Z. Ren, *J. Appl. Phys.*, **117** (2015) 055101.

- [20] R. Funahashi, M. Shikano, *Appl. Phys. Lett.*, **81** (2002) 1459-1461.
- [21] K. Fujita, T. Mochida, K. Nakamura, *Jpn. J. Appl. Phys.*, **40** (2001) 4644-4647.
- [22] M. Shikano, R. Funahashi, *Appl. Phys. Lett.*, **82** (2003) 1851-1853.
- [23] J.-L. Lan, Y. Liu, Y.-H. Lin, C.-W. Nan, Q. Cai, X. Yang, *Sci. Rep.*, **5** (2015) 7783.
- [24] M. Mikami, K. Ozaki, *J. Phys.: Conf. Ser.*, **379** (2012) 012006.
- [25] A.V. Kovalevsky, A.A. Yaremchenko, S. Populoh, P. Thiel, D.P. Fagg, A. Weidenkaffbd, J.R. Fradea, *Phys. Chem. Chem. Phys.*, **16** (2014) 26946-26954.
- [26] P. Jood, R.J. Mehta, Y. Zhang, G. Peleckis, X. Wang, R.W. Siegel, T. Borca-Tasciuc, S.X. Dou, G. Ramanath, *Nano Lett.*, **11** (2011) 4337-4342.
- [27] Y. Michiue, T. Mori, A. Prytuliak, Y. Matsushita, M. Tanaka, N. Kimizukac, *RSC Adv.*, **1** (2011) 1788-1793.
- [28] R.S.S. Maki, S. Mitani, T. Mori, *Mater. Renew. Sustain. Energy*, **6:2** (2017) 1-8.
- [29] I. Ohkubo, T. Mori, *APL Mater.*, **4** (2016) 104808.
- [30] I. Ohkubo, T. Mori, *Chem. Mater.*, **27** (2015) 7265-7275.
- [31] T.L. Aselage, D. Emin, S.S. McCready, R.V. Duncan, *Phys. Rev. Lett.*, **81** (1998) 2316.
- [32] A.N. Caruso, S. Balaz, B. Xu, P.A. Dowben, A.S. McMullen-Gunn, J.I. Brand, Y.B. Losovyj, D.N. McIlroy, *Appl. Phys. Lett.*, **84** (2004) 1302.
- [33] V. Domnich, S. Reynaud, R.A. Haber, M. Chhowalla, *J. Am. Ceram. Soc.*, **94** (2011) 3605-3628.
- [34] K. Rasim, R. Ramlau, A. Leithe-Jasper, T. Mori, U. Burkhardt, H. Borrmann, W. Schnelle, C. Carbogno, M. Scheffler, Y. Grin, *Angew. Chem. Int. Ed.*, **57** (2018) 6130-6135.
- [35] J.-L. Innocent, D. Portehault, G. Gouget, S. Maruyama, I. Ohkubo, T. Mori, *Mater. Renew. Sustain Energy*, **6:6** (2017) 1-7.
- [36] T. Nakayama, J. Shimizu, K. Kimura, *J. Solid State Chem.*, **154** (2000) 13-19.
- [37] O. Sologub, L. Salamakha, B. Stöger, Y. Michiue, T. Mori, *Acta Mater.*, **122** (2017) 378-385.
- [38] Y. Gong, Y. Zhang, M. Dudley, Y. Zhang, J. H. Edgar, P. J. Heard, M. Kuball, *J. Appl. Phys.*, **108** (2010) 084906.

- [39] C.D. Frye, J.H. Edgar, I. Ohkubo, T. Mori, *J. Phys. Soc. Jpn.*, **82** (2013) 095001.
- [40] T. Mori, *J. Appl. Phys.*, **97** (2005) 093703.
- [41] M.A. Hossain, I. Tanaka, T. Tanaka, A.U. Khan, T. Mori, *J. Solid State Chem.*, **233** (2016) 1-7.
- [42] A. Sussardi, T. Tanaka, A.U. Khan, L. Schlapbach, T. Mori, *J. Materiomics.*, **1** (2015) 196-204.
- [43] T. Mori, T. Tanaka, *J. Solid State Chem.*, **179** (2006) 2889-2894.
- [44] M. Takeda, M. Terui, N. Takahashi, N. Ueda, *J. Solid State Chem.*, **179** (2006) 2823-2826.
- [45] M. Gürsoy, M. Takeda, B. Albert, *J. Solid State Chem.*, **221** (2015) 191-195.
- [46] S. Maruyama, Y. Miyazaki, K. Hayashi, T. Kajitani, T. Mori, *Appl. Phys. Lett.*, **101** (2012) 152101.
- [47] S. Maruyama, A. Prytuliak, Y. Miyazaki, K. Hayashi, T. Kajitani, T. Mori, *J. Appl. Phys.*, **115** (2014) 123702.
- [48] R. Sahara, T. Mori, S. Maruyama, Y. Miyazaki, K. Hayashi, T. Kajitani, *Sci. Technol. Adv. Mater.*, **15** (2014) 035012.
- [49] S. Maruyama, T. Nishimura, Y. Miyazaki, K. Hayashi, T. Kajitani, T. Mori, *Mater. Renew. Sustain Energy.*, **3:31** (2014) 1-6.
- [50] T. Mori, T. Nishimura, *J. Solid State Chem.*, **179** (2006) 2908-2915.
- [51] D. Berthebaud, T. Nishimura, T. Mori, *J. Electron. Mater.*, **40** (2011) 682-686.
- [52] T. Mori, T. Nishimura, W. Schnelle, U. Burkhardt, Y. Grin, *Dalton Trans.*, **43** (2014) 15048-15054.
- [53] T. Mori, T. Nishimura, K. Yamaura, E. Takayama-Muromachi, *J. Appl. Phys.*, **101** (2007) 093714.
- [54] D. Berthebaud, T. Nishimura, T. Mori, *J. Mater. Res.*, **25** (2010) 665669.
- [55] T. Mori, Higher Borides, in: K.A. Gschneidner Jr., J.-C.G. Bünzli, V.K. Pecharsky (Eds.), *Handbook on the Physics and Chemistry of Rare Earths*, Elsevier Science (2008) 105-173.
- [56] T. Mori, *J. Sol. Stat. Chem.*, **275** (2019) 70-82.
- [57] 掛川一幸, 山村博, 守吉祐介, 門間英毅, 植松敬三, 松田元秀, 朝倉書店, 52, (2000).
- [58] R.M. German, *Powder Metallurgy & Particulate Materials Processing*, Metal Powder Industry (2005).
- [59] H.-W. Son, B.-N. Kim, T.S. Suzuki, Y. Suzuki, *J. Am. Ceram. Soc.*, **101** (2018) 4430-4433.

- [60] R.M.German, P. Suri, S.J. Park, *J. Mater. Sci.*, **44** (2009) 1-39.
- [61] D. Gupta, *Diffusion Processes in Advanced Technological Materials*, Springer (2004).
- [62] M.N. Rahaman, *Ceramic Processing*, CRC Press (2006).
- [63] J.S. Reed, *Principles of ceramics processing*, JOHN WILEY & SONS, INC. (1995).
- [64] G. Cao, Y. Wang, *Nanostructures & Nanomaterials: Synthesis, Properties & Applications*, World Scientific (2011).
- [65] M.N. Rahaman, *Sintering of Ceramics*, CRC Press (2007).
- [66] R. German, *Sintering: From Empirical Observations to Scientific Principles*, Butterworth-Heinemann (2014).
- [67] L.U.J.T. Ogbuji, *Ceram. Int.*, **12** (1986) 195-202.
- [68] R.A. Dorey, *Ceramic Thick Films for MEMS and Microdevices*, William Andrew (2011).
- [69] S. Tanaka, *Solid State Reactions and Sintering*, in: J. Honor (Ed.), *Materials Chemistry of Ceramics*, Springer Nature Singapore Pte Ltd. (2019).
- [70] C.V. Nguyen, S.K. Sistla, S.V. Kempen, N.A. Giang, A. Bezold, C. Broeckmann, F. Lange, *J. Ceram. Soc. Jpn.*, **124** (2016) 301-312.
- [71] Y. Suzuki, Y. Shinoda, K. Yoshida, *Adv. Eng. Mater.*, **14** (2012) 1134-1138.
- [72] P. Cavaliere, B. Sadeghi, A. Shabani, *Spark Plasma Sintering of Materials*, Springer (2019).
- [73] H. Ono, N. Waki, T. Sugiyama, M. Shimada, A. Fujiki, H. Yamamoto, M. Tani, *J. Magn. Soc. Jpn.*, **25** (2001) 679-682.
- [74] O. Guillon, J. Gonzalez-Julian, B. Dargatz, T. Kessel, G. Schierning, J. Räthel, M. Herrmann, *Adv. Eng. Mater.*, **16** (2014) 830-849.
- [75] K. Sairam, J.K. Sonber, T.S.R.Ch. Murthy, C. Subramanianm R.K. Fotedar, P. Nanekar, R.C. Hubli, *Int. J. Refract. Met. Hard. Mater.*, **42** (2014) 185-192.
- [76] B.-N. Kim, E. Prajatelista, Y.-H. Han, H.-W. Son, Y. Sakka, S. Kim, *Scr. Mater.*, **69** (2013) 366-369.

Chapter 2

Thermoelectric Properties of MgTi₂O₅/TiN Conductive Composites Synthesized via Reactive Spark Plasma Sintering through Solid-State Reaction

2.1 Introduction

Pseudobrookite-type MgTi₂O₅ possesses orthorhombic structure with a *Cmcm* space group (**Fig. 2.1**) [1]. The crystal structure of MgTi₂O₅ consists of two kinds of MO₆ octahedra (M1 and M2), edge-sharing and corner-sharing, where M refers to Mg²⁺/Ti⁴⁺ cations. M1 site is larger than M2 site, thereby M1 sites are preferentially occupied by Mg²⁺ ions, while M2 sites are preferentially occupied by Ti⁴⁺ ions. Since the sizes of cations are larger than the octahedral sites, the sites are highly distorted, as a result, MgTi₂O₅ exhibits strong anisotropic thermal expansion.

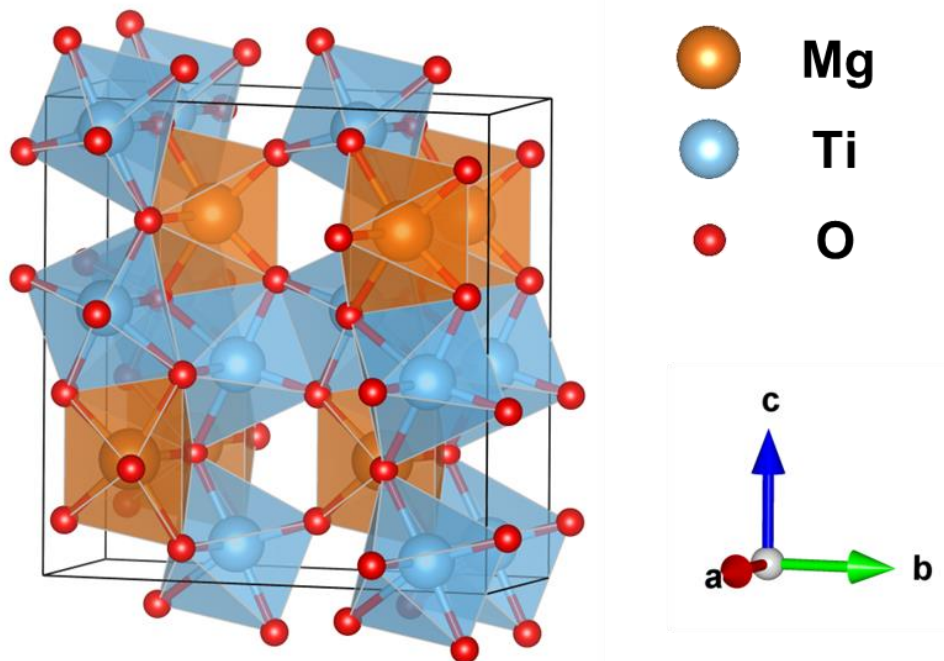


Figure 2.1. Crystal structure of MgTi₂O₅ (in the *Cmcm* space group notation) [1].

The coefficients of thermal expansion (CTE) of MgTi₂O₅ are very small in the *a*-direction, moderate in *b*-direction and rather large in *c*-direction [1-4] (**Table 2.1**). Since this large thermal expansion anisotropy results in a formation of extensive internal microcracks in bulk during cooling in the sintering process, polycrystalline MgTi₂O₅ has low thermal expansion, low thermal conductivity and high thermal shock resistance [1]. Moreover, it has not only attractive thermomechanical properties, but also high temperature stability, high melting point (~1950 K) and

reasonable price, hence it might be a promising material for high temperature applications [4]. However, due to its extremely low electrical conductivity ($\sim 2.0 \times 10^{-2}$ S/m at 1273 K) [5], MgTi_2O_5 has not been studied for thermoelectric materials.

Table 2.1. Coefficients of thermal expansion (CTE) of pseudobrookite-type MgTi_2O_5 , shown within $Cmcm$ (63) space group [1].

CTE in directions	CTE at 293-793 K ($\times 10^{-6}$ K $^{-1}$)	CTE at 293-1293 K ($\times 10^{-6}$ K $^{-1}$)
α_a	2.3 ± 0.2	2.3 ± 0.2
α_b	8.1 ± 0.4	10.8 ± 0.5
α_c	13.2 ± 0.7	15.9 ± 0.8

Herein, to increase its poor electrical conductivity, we designed MgTi_2O_5 -based composites having low thermal conductivities and good thermomechanical properties of the matrix phase converged with high electrical conductivity of a reinforcement phase. For the conductive reinforcement phase, TiN was selected. TiN possesses metallic electrical conductivity and excellent thermal resistivity, and furthermore, can make composites with TiO_2 [6-8]. However, it exhibits a relatively high thermal conductivity, and more importantly, its Seebeck coefficient takes very small values (~ 10 $\mu\text{V/K}$ at 400 K) [6,8]. Hence, pure TiN itself is also not suitable for thermoelectric applications.

In this study, as a new n-type thermoelectric oxide-based material for high temperature functional applications, thermoelectric properties of $\text{MgTi}_2\text{O}_5/\text{TiN}$ conductive composite materials prepared by spark plasma sintering were investigated. **Figure 2.2** demonstrates the schematic diagram of designed $\text{MgTi}_2\text{O}_5/\text{TiN}$ conductive composite materials for a new type thermoelectric material. It is expected that this new approach could enhance its thermoelectric properties through combining the advantages of each material.

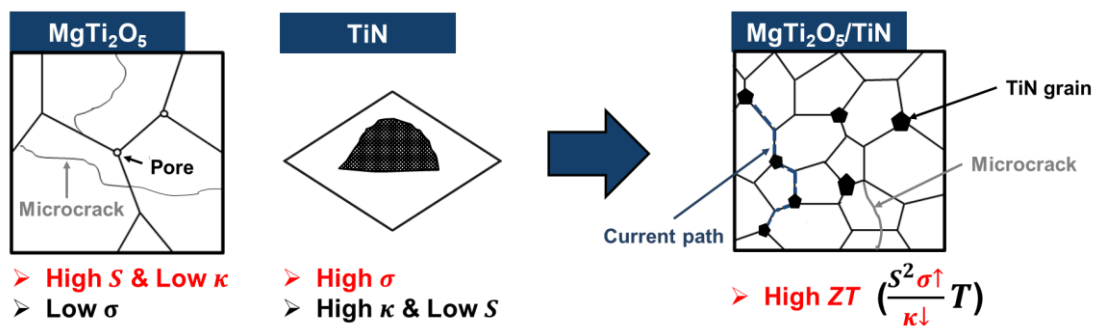


Figure 2.2. Schematic diagram of $\text{MgTi}_2\text{O}_5/\text{TiN}$ conductive composites for a new type thermoelectric material.

2.2 Experimental procedure

2.2.1 Synthesis

To enhance the reactivity and shorten reaction time, commercially available MgO (99.9%, 0.05 μm , Wako Co., Ltd.), TiO₂ rutile (99.5%, <100 nm, Sigma-Aldrich Co., Ltd.) and TiN (1.0-1.5 μm , Wako Co., Ltd.) powders were used as the starting materials. The powders of MgO, TiO₂ and 0-30 vol.% TiN were simply mixed under ethanol using SiO₂ mortar with various molar ratios of TiO₂/MgO, where the molar ratios are 2.00, 2.50 and 2.67 (**Table 2.2**).

Table 2.2. Initial molar ratio of TiO₂/MgO and TiN content of each sample.

Sample name	Molar ratio of TiO ₂ /MgO	TiN content (vol.%)
M1N0	2.00	0
M1N10	2.00	10
M1N20	2.00	20
M1N30	2.00	30
M2N10	2.50	10
M3N10	2.67	10

The powder mixtures were dried in oven at 100°C for 6 h, and then poured into a 10 mm diameter graphite die. The mixtures were reactively sintered using a SPS machine (Dr. Sinter, Fuji Denpa Koki Co., Ltd.) at 1100°C for 10 min under a uniaxial pressure of 80 MPa in vacuum (~2-4 Pa). Finally, the sintered discs, 10 mm diameter and ~2 mm thickness, were obtained.

2.2.2 Characterizations

The constituent phases of sintered samples were analyzed by X-ray diffraction (XRD, Smart lab 3, Rigaku) with Cu K α radiation ($\lambda=1.5418 \text{ \AA}$). In order to determine thermal conductivities, the thermal diffusivities and the specific heats of all samples were measured from 300 to 773 K by using a laser flash analysis (LFA-467, NETZSCH Japan Co., Ltd.). The electrical resistivities and Seebeck coefficients were evaluated using a thermoelectric tester (ZEM-2, ADVANCE RIKO, Inc.) at the temperature range of 373-973 K. Microstructure of fracture surface for each sample was observed by scanning electron microscopy (SEM, S-8000, Hitachi High-Technologies Co.).

2.3 Results and discussion

2.3.1 Phase identification

Figure 2.3 shows XRD patterns of the MgTi_2O_5 and $\text{MgTi}_2\text{O}_5/\text{TiN}$ composites prepared by reactive SPS at 1100°C for 10 min with 2:1 molar ratio of $\text{TiO}_2:\text{MgO}$. The MgTi_2O_5 sample sintered without TiN, M1N0, mainly consisted of MgTi_2O_5 with trace amount of secondary phases, MgTiO_3 and rutile. It indicates that MgTi_2O_5 was successfully synthesized by reactive SPS. In contrast, the MgTi_2O_5 samples sintered with 10-30 vol.% TiN, M1N10, M1N20 and M1N30, did not contain rutile phase, but they contained a rather large amount of MgTiO_3 phase. The ratio of MgTiO_3 phase to MgTi_2O_5 phase increased with increasing TiN content.

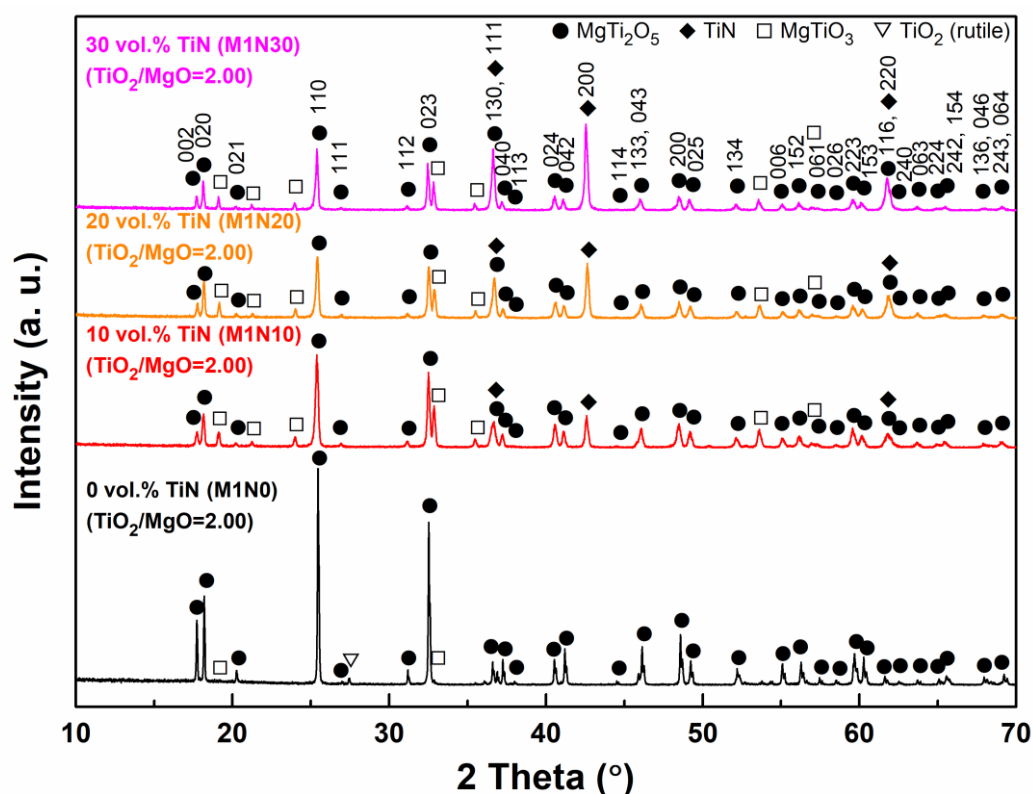


Figure 2.3. XRD patterns of the MgTi_2O_5 (M1N0) and $\text{MgTi}_2\text{O}_5/\text{TiN}$ samples (M1N10, M1N20 and M1N30) prepared by reactive SPS at 1100°C for 10 min under a uniaxial pressure of 80 MPa in vacuum ($\sim 2-4$ Pa). The TiN contents in M1N10, M1N20 and M1N30 are 10, 20 and 30 vol.%, respectively. The initial molar ratio of TiO_2/MgO of all samples is 2.00.

For TiO_2 , a relatively wide range of stoichiometry can be allowed, ranging from TiO to TiO_2 . It implies that oxygen vacancies and planar defects can be easily introduced in rutile structure under a reductive atmosphere. The defects are also able to cause a corresponding crystallographic structure change, from TiO_2 rutile to $\text{Ti}_n\text{O}_{2n-1}$ ($n=4-38$), which is known as Magnéli phase [9,10,11-13]. Nitrogen is one of the strong candidates as a reducing agent for TiO_2 [18]. It thus can be considered that the increase of amount of MgTiO_3 phase with increasing TiN content is attributed to the reaction between TiO_2 and TiN during sintering.

Figure 2.4 shows XRD patterns of the $\text{MgTi}_2\text{O}_5/10$ vol.% TiN composites prepared by reactive SPS at 1100°C for 10 min with three different initial molar ratios of TiO_2/MgO , 2.00, 2.50 and 2.67. The amount of MgTiO_3 phase remarkably decreased with increasing the initial ratio of TiO_2/MgO . The $\text{MgTi}_2\text{O}_5/\text{TiN}$ composite with the least amount of secondary phase was obtained for M3N10, whose initial molar ratio of TiO_2/MgO is 2.67. All samples did not exhibit any peak for rutile phase or Magnéli phase. It indicates that the TiO_2 loss during sintering is well compensated by adding excess TiO_2 .

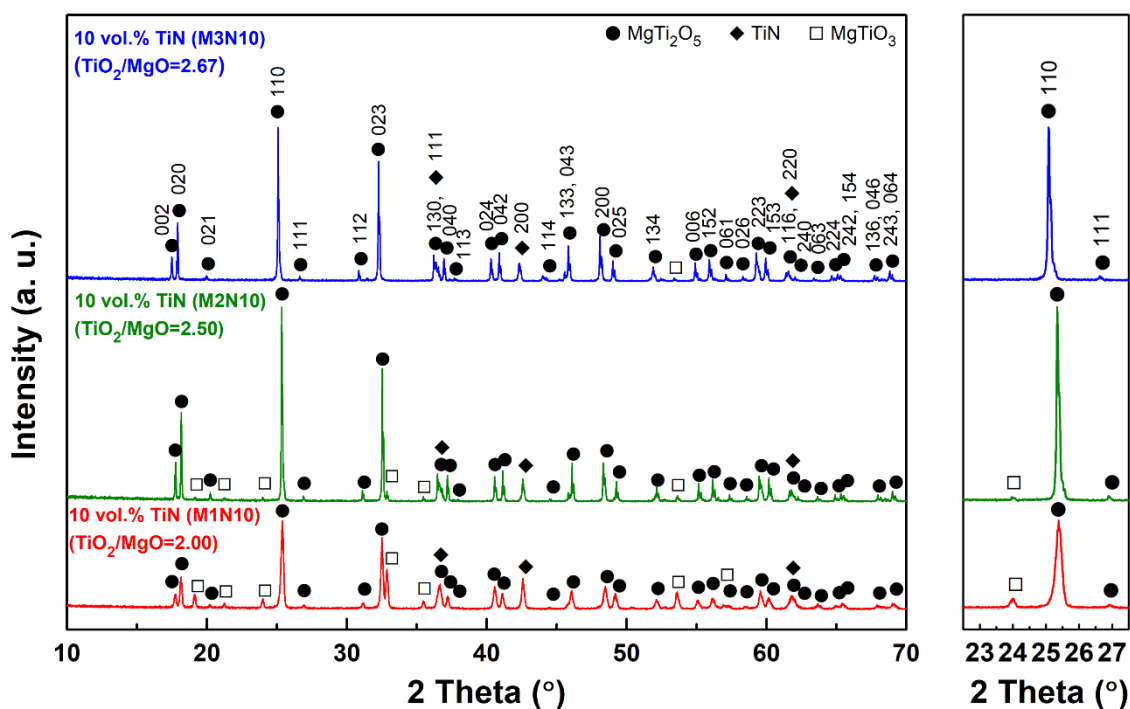


Figure 2.4. XRD patterns of the $\text{MgTi}_2\text{O}_5/10$ vol.% TiN samples sintered with various molar ratio of TiO_2/MgO . The samples were prepared by reactive SPS at 1100°C for 10 min under a uniaxial pressure of 80 MPa in vacuum ($\sim 2-4$ Pa). The initial molar ratios of TiO_2/MgO of M1N10, M2N10 and M3N10 are 2.00, 2.50 and 2.67, respectively. The TiN content in all samples is fixed as 10 vol.%.

For M1N10, M2N10 and M3N10, the positions of XRD peaks of MgTi_2O_5 and MgTiO_3 are shifted to the lower angle with increasing molar ratio of TiO_2/MgO . In $\text{MgTi}_2\text{O}_5\text{-Ti}_n\text{O}_{2n-1}$ ($n=3$) system, the phase equilibrium involves pseudobrookite-type solid solution series, $\text{Mg}_{1-x}^{2+}\text{Ti}_{2-x}^{4+}\text{Ti}_{2x}^{3+}\text{O}_5$ [14-16]. For these series, when $x=0$, the lattice parameters in $Cmcm$ space group notation, a , b , and c are 3.7481, 9.7333 and 10.0022 Å, respectively [15]. The lattice is expanded along a - and b -directions with increasing x value, whereas it is shrunk along c -direction. The observed pattern, calculated pattern, and difference of the XRD profiles of the M3N10 sample is shown in **Fig. 2.5**. The estimated lattice parameters of the M3N10 sample from Rietveld analysis with profile matching technique, a , b and c are 3.7587, 9.7497 and 9.9768 Å, respectively. These parameter values imply that the composition range of M3N10 is in $\text{Mg}_{1-x}^{2+}\text{Ti}_{2-x}^{4+}\text{Ti}_{2x}^{3+}\text{O}_5$ ($0 < x < 0.1$). It is therefore considered that M3N10 sample contains extra Ti^{3+} cations in MgTi_2O_5 lattice, which is originated from the reduction of the excess TiO_2 during sintering. Moreover, this also suggests a possibility that the doping level of Ti^{3+} cations in this system can be controlled by reactive SPS process.

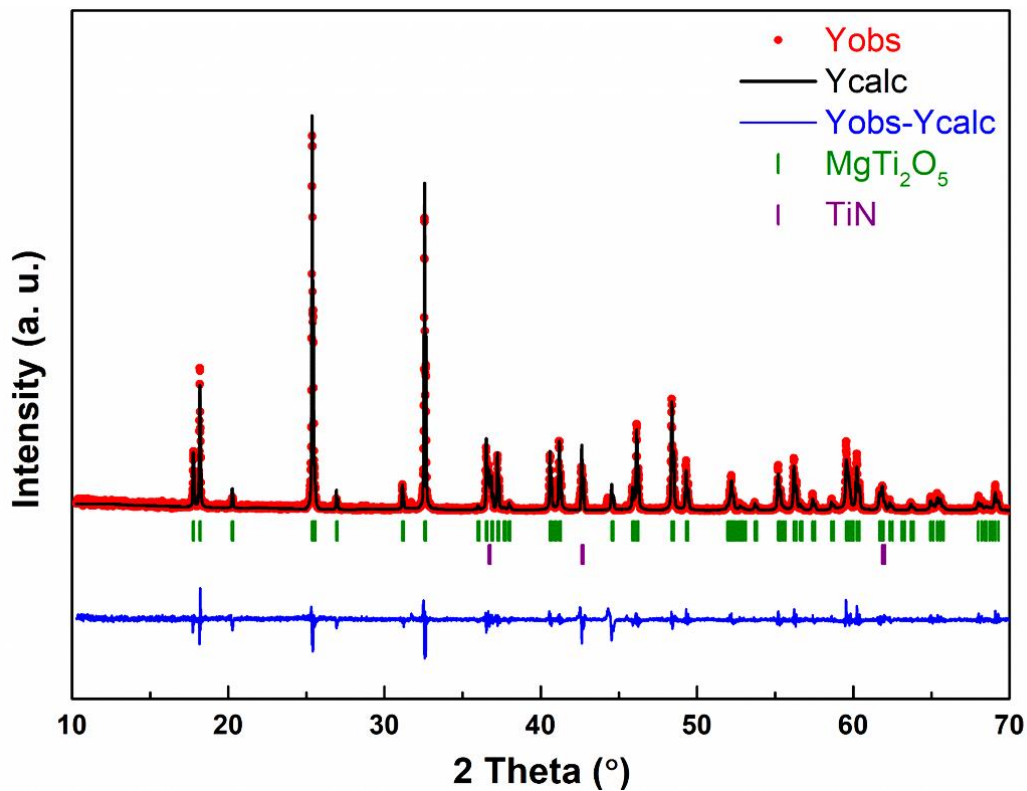


Figure 2.5. The observed pattern, calculated pattern, and differences between observed and calculated patterns of the XRD profiles of the M3N10 sample; (•) symbols represent the observed pattern; the black solid line represents the calculated pattern; the blue solid line represents the difference between observed and calculated patterns. The green and purple vertical bars indicate the Bragg positions of MgTi_2O_5 -based solid solution and TiN, respectively.

2.3.2 Thermal properties

The thermal diffusivities and thermal conductivities of the samples are shown in **Fig. 2.6** and **2.7**. Although the secondary phase TiN is a very high thermal conductivity material (28.9 W/mK at 298 K) [6], the MgTi₂O₅/TiN composites did not exhibit such high thermal conductivity values.

At room temperature, the thermal diffusivity of non-doped MgTi₂O₅, M1N0, prepared by reactive SPS was slightly lower than the reported thermal diffusivity value (~1.3 mm²/s) of MgTi₂O₅ prepared at 1473 K for 1 h by hot pressing. Internal microcracks and oxygen vacancies in composites appear to effectively inhibit thermal conduction by scattering phonons, which will be discussed later with microstructure analysis and electrical conductivities.

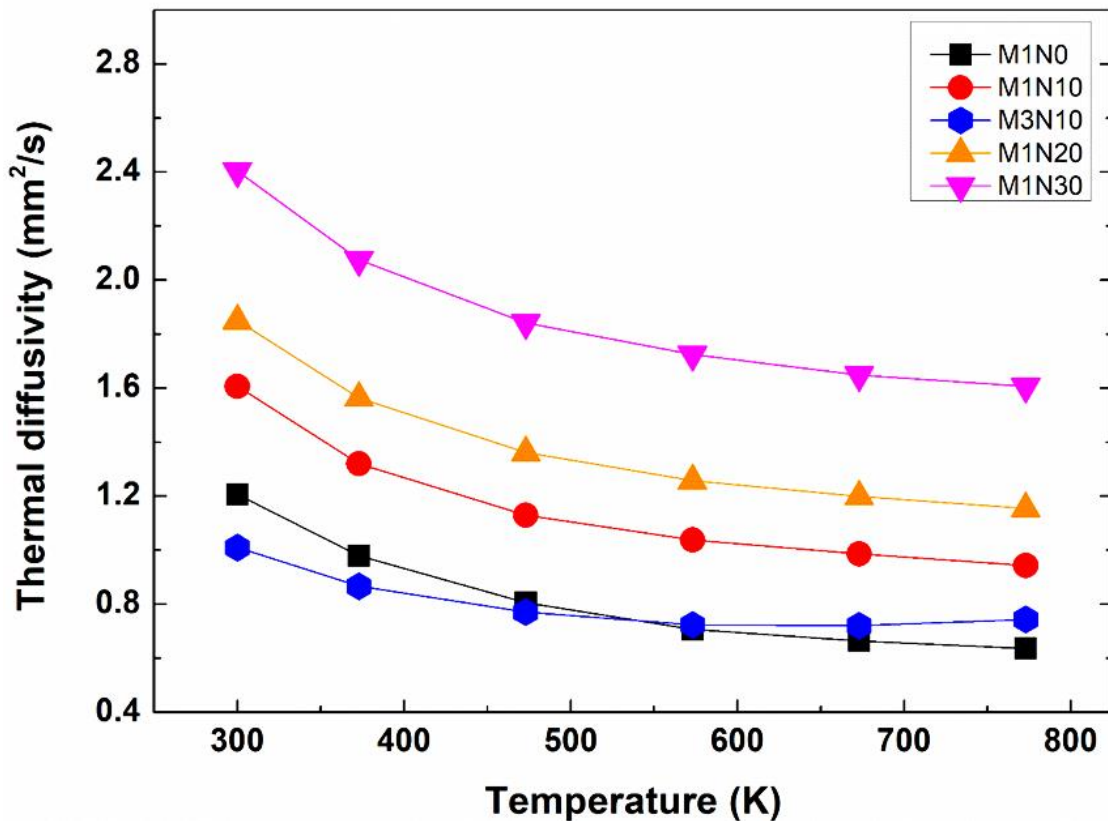


Figure 2.6. The temperature dependence of thermal diffusivities of sintered samples. The maximum measured temperature, 773 K is the measurement limit of the equipment.

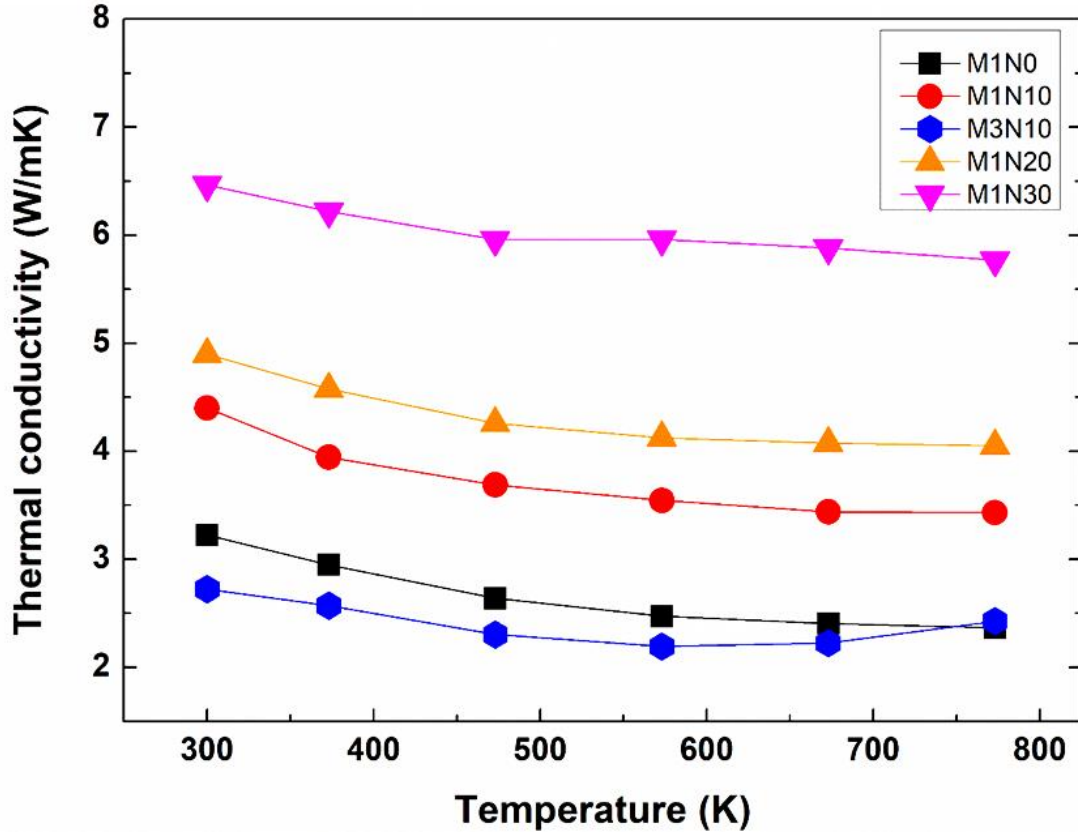


Figure 2.7. The temperature dependence of thermal conductivities of sintered samples. The maximum measured temperature, 773 K is the measurement limit of the equipment.

Thermal diffusivity and conductivity of $\text{MgTi}_2\text{O}_5/\text{TiN}$ composite generally increased with increasing TiN content. However, M3N10 exhibited lower thermal conductivity values at low temperatures, than even non-doped M1N0 although it contains 10 vol.% TiN. The origin of this can be elucidated by considering defect engineering in MgTi_2O_5 .

Figure 2.8 shows the crystal structures of ordered MgTi_2O_5 , disordered MgTi_2O_5 , and disordered MgTi_2O_5 -based solid solution. As introduced in *section 2.1*, the orthorhombic pseudobrookite-type MgTi_2O_5 contains two octahedral sites, which are the larger M1 site (4c) and smaller M2 site (8f). In the fully ordered MgTi_2O_5 , M1 site is fully occupied by Mg^{2+} ions, while M2 site is fully occupied by Ti^{4+} ions ($[\text{Mg}_1^{2+}]^{4c}[\text{Ti}_1^{4+}]_2^{8f}\text{O}_5$), as shown in **Fig. 2.8 (a)**.

However, at high temperature, $\text{Mg}^{2+}/\text{Ti}^{4+}$ cation disordering ($[\text{Mg}_{1-2x}^{2+}\text{Ti}_{2x}^{4+}]^{4c}[\text{Mg}_x^{2+}\text{Ti}_{1-x}^{4+}]_2^{8f}\text{O}_5$) can easily be introduced due to a large configurational entropy of MgTi_2O_5 (**Fig. 2.8 (b)**) [15,17,18]. The fully disordered structure is obtained when $x=1/3$. The $\text{Mg}^{2+}/\text{Ti}^{4+}$ cation disordering also depends on the cooling rate after heating due to slow kinetics of $\text{Mg}^{2+}/\text{Ti}^{4+}$ interchange. Hence, rapid cooling from high temperatures can keep the disordered structure, whereas slow cooling from high temperatures and annealing at lower temperature lead to a decrease of

the cation disorder [19].

The cation disordering shortens average M1-O bond distance while lengthening M2-O bond distance due to the size difference between cations and octahedral sites, as a result, it induces a stronger lattice distortion [20,21]. Moreover, $\text{Ti}^{3+}/\text{Ti}^{4+}$ cation disordering ($[\text{Ti}^{3+}]^{4c}[\text{Ti}^{3+}, \text{Ti}^{4+}]_2^{8f}\text{O}_5$) in $\text{Mg}_{1-x}\text{Ti}_{2+x}\text{O}_5$ solid solution also induces further lattice distortion (**Fig. 2.8 (c)**) [15].

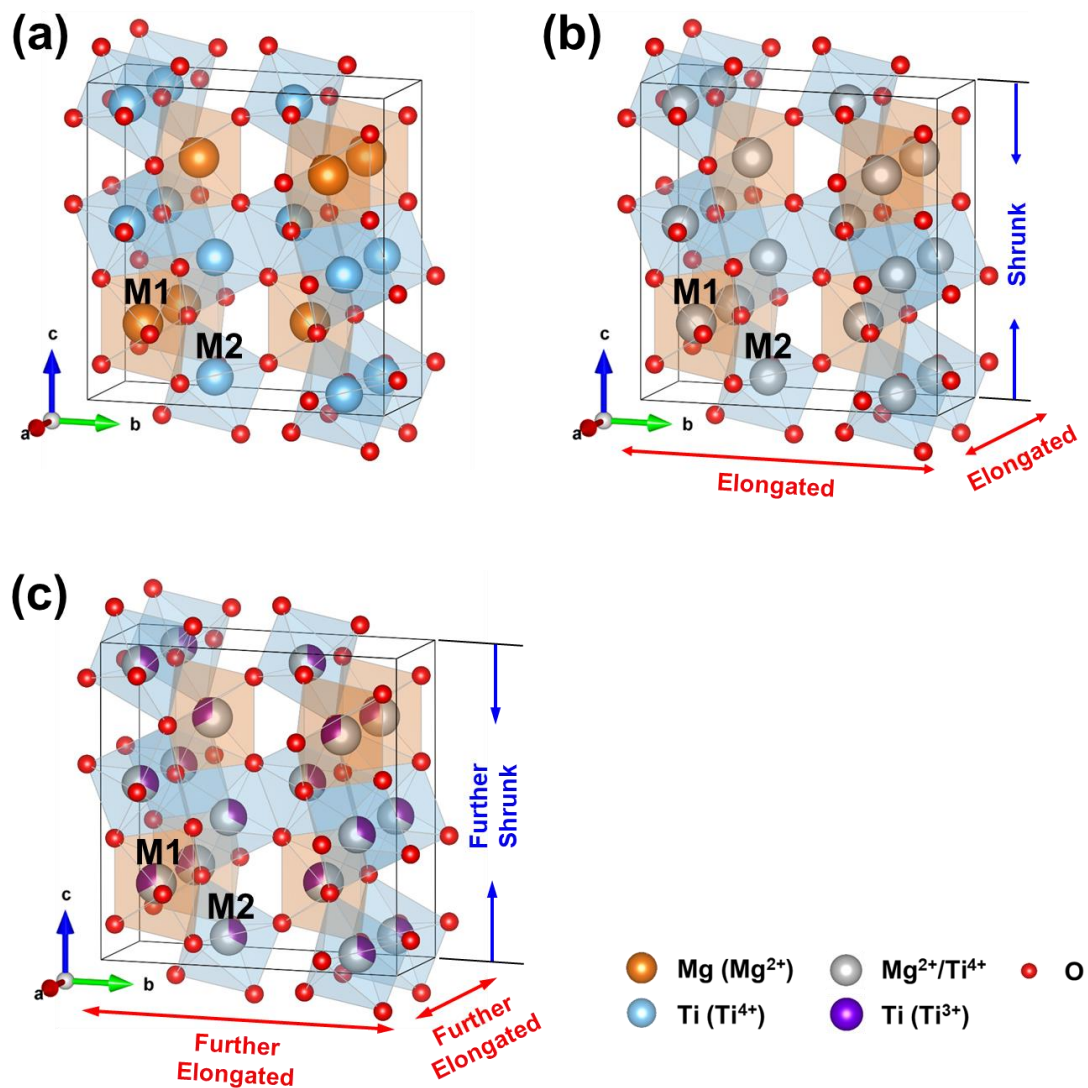


Figure 2.8. The crystal structure of (a) ordered MgTi_2O_5 , (b) disordered MgTi_2O_5 and (c) disordered $\text{Mg}_{1-x}\text{Ti}_{2+x}\text{O}_5$.

The local lattice distortion introduced by two kinds of cation disordering acts as a phonon scattering center, and thus it leads to a decrease of lattice thermal conductivity [10]. The thermal conductivity of these oxides are dominated by lattice thermal conductivity, and it is therefore indicated that the low thermal conductivity of the M3N10 sample is mainly attributed to the phonon scattering by lattice distortion induced by Mg^{2+}/Ti^{4+} and Ti^{3+}/Ti^{4+} cation disordering. The grain boundaries, microcracks and oxygen vacancies are also able to act as phonon scattering centers, as shown in **Fig. 2.9**.

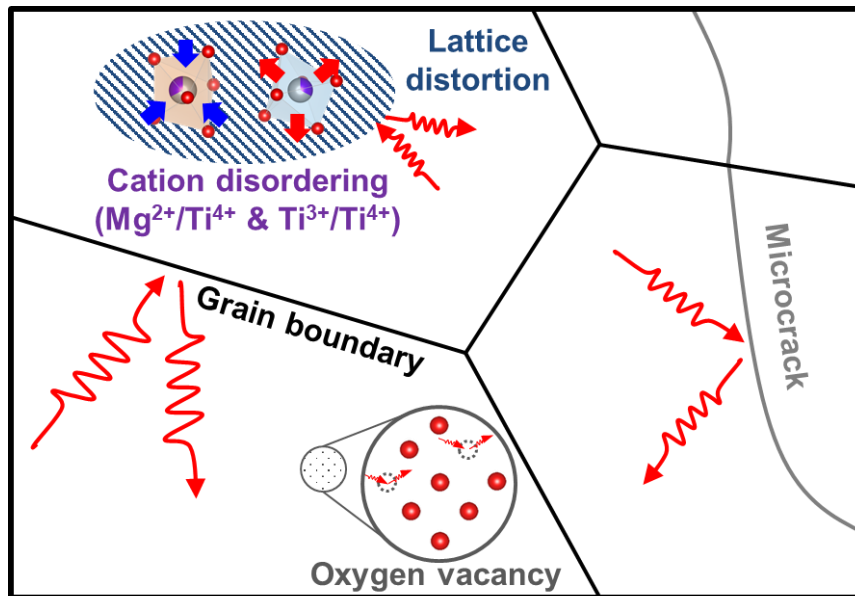


Figure 2.9. The schematic diagram for phonon scattering by defects in $Mg_{1-x}Ti_{2+x}O_5$.

Meanwhile, the thermal diffusivities and conductivities of most samples generally decreased with increasing temperature, however, that of M3N10, the lowest thermal conductivity sample, slightly increased above 673 K. This behavior might be attributed to variation in the Ti^{3+}/Ti^{4+} cation disordering from thermal activation [15,17].

2.3.3 Microstructure

Figure 2.10 shows changes of microstructure of the samples sintered with various TiN contents. Extensive internal microcracks are observed in the samples, which contains TiN 0-20 vol.%. Average grain size is reduced with increasing TiN content, indicating grain growth suppression by adding TiN. In general, small secondary phases such as precipitates and segregates in composites are predominantly positioned at grain boundaries and/or triple junctions to reduce excess energy by reducing their interfacial area.

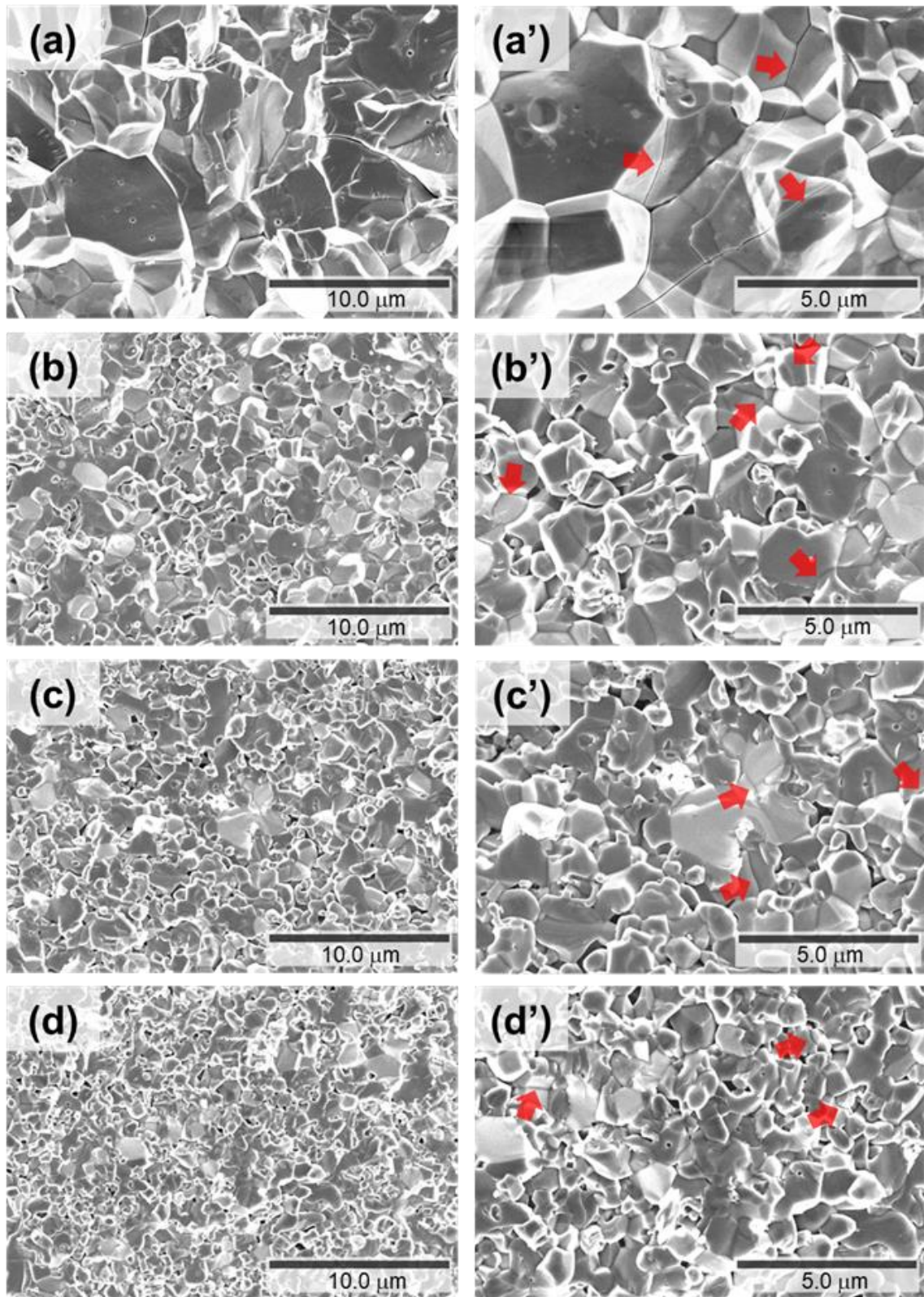


Figure 2.10. SEM images of fracture surface of the MgTi_2O_5 and $\text{MgTi}_2\text{O}_5/\text{TiN}$ composites sintered with various TiN contents; (a, a') M1N0 (0 vol.% TiN), (b, b') M1N10 (10 vol.% TiN), (c, c') M1N20 (20 vol.% TiN) and (d, d') M1N30 (30 vol.% TiN). The arrows indicate some representative microcracks.

When inclusions or precipitates are positioned at those locations, grain growth can be suppressed because it accompanies an increase of total interfacial area. Therefore, the morphology changes of MgTi₂O₅/TiN composites with increasing TiN contents might be attributed to small TiN grains pinned at grain boundaries and/or triple junctions.

M1N0 exhibited dominant transgranular microcracks with the coarsest microstructure, whereas M1N30 exhibited dominant intergranular microcracks with finest microstructure. These phenomena are based on the thermodynamics. When internal microcracks are formed, the elastic strain energy is reduced, whereas the surface energy is increased due to the formation of new fracture surfaces. Thus, for the formation of internal microcracks, the released elastic strain energy must be equal or more than increased surface energy. The energy balance for microcracking can be expressed as follows:

$$U_{\text{tot}} = U_0 - U_{\text{st}} + U_{\text{surf}} \quad (2.1)$$

where U_{tot} is the total energy of the system, U_0 is the energy of the grain which does not contain microcrack, U_{st} is the elastic strain energy, and U_{surf} is grains fracture surface energy. The energy balance amongst U_{tot} , U_{st} and U_{surf} are shown in **Fig. 2.11**.

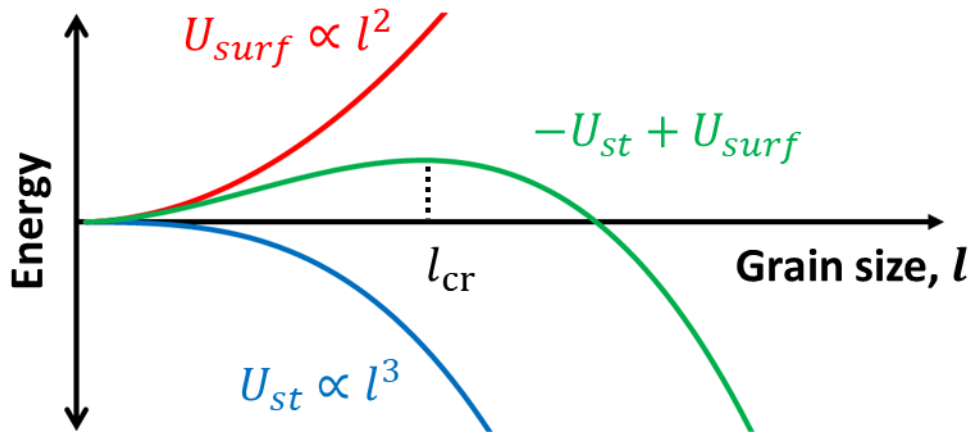


Figure 2.11. The energy balance amongst U_{tot} , U_{st} and U_{surf} . The l_{cr} indicates the critical grain size when the released elastic strain energy is equal to increased fracture surface energy.

Assuming a polycrystalline material, which consists of identical dodecahedral grains, the total energy is:

$$U_{\text{tot}} = U_0 - E_{\text{st}}\Delta V + \gamma_f\Delta A = U_0 - 7.66Nl^3E_{\text{st}} + 20.65Nl^2\gamma_f \quad (2.2)$$

where E_{st} is stored elastic strain energy, γ_f is a fracture surface energy, l is the size of the dodecahedral grain, and N is the number of grains which release their stored elastic strain energy by microcracking [22]. The critical grain size for microcracking can be derived by differentiating Eq. 2.2 with respect to the grain size, l , as follows:

$$U'_{\text{total}} = 0 = -22.98N(l_{\text{cr}})^2E_{\text{st}} + 41.30N\gamma_f l_{\text{cr}} \quad (2.3)$$

Hence, the critical grain size, l_{cr} , can be expressed as:

$$l_{\text{cr}} = 1.797 \left(\frac{\gamma_f}{E_{\text{st}}} \right) \quad (2.4)$$

Meanwhile, the elastic strain, E_{st} , is defined as:

$$E_{\text{st}} = \frac{1}{2} \sigma \varepsilon = \frac{1}{2} \left(\frac{\sigma^2}{E} \right) \quad (2.5)$$

where σ is developed stress, ε is strain, and E is elastic modulus. The relationship amongst developed stress, σ , elastic modulus, E , CTE of a single grain, α , and a temperature change, ΔT , is given by

$$\sigma = E\alpha\Delta T \quad (2.6)$$

Extending Eq. 2.6 to two adjacent grains of maximum thermal expansion mismatch yields:

$$\sigma = \frac{1}{2} E\Delta\alpha\Delta T \quad (2.7)$$

where $\Delta\alpha$ is $(\alpha_{\text{max}} - \alpha_{\text{min}})$, and α_{max} and α_{min} are maximum and minimum CTE for a single grain, respectively. In general, $\Delta\alpha$ in pseudobrookite-type MgTi_2O_5 with the $Cmcm$ space group notation is $(\alpha_c - \alpha_a)$. Substituting Eq. 2.7 into Eq. 2.5, E_{st} yields;

$$E_{\text{st}} = \frac{1}{8} E\Delta\alpha^2\Delta T^2 \quad (2.8)$$

Therefore, for a polycrystalline material, which consists of identical dodecahedral grains, the derived critical grain size for microcracking is expressed as follows [22];

$$l_{\text{cr}} = \frac{14.4\gamma_f}{E(\Delta\alpha\Delta T)^2} \quad (2.9)$$

Estimated E , γ_f and $\Delta\alpha$ for MgTi_2O_5 were reported as 250 GPa, 5 N/m and $\sim 14.6 \times 10^{-6} \text{ K}^{-1}$, respectively [1,22]. The calculated critical grain size for microcracking of polycrystalline MgTi_2O_5 sintered at 1373 K is $\sim 1.1 \mu\text{m}$. Here,

the cooling rate was kept fast enough for keeping the cation disordering. Since average grain sizes of sintered samples are significantly larger than their critical grain size, extensive microcracks are generated during SPS. The microcracking mode is also closely related to a difference between its average grain size and critical grain size for microcracking. When average grain size is much larger than critical grain size, microcracking mode follows the transgranular mode, while when it is similar, it follows the intergranular mode.

To investigate the effect of excess TiO_2 , SEM observation of fracture surfaces of M1N10 and M3N10 were conducted. As shown in **Fig. 2.12**, M3N10 exhibits transgranular and intergranular microcracks with relatively coarse microstructure, whereas M1N10 exhibits intergranular microcracks with relatively fine microstructure. This difference can be mainly attributed to an additional pinning effect by the remaining MgTiO_3 phase in M1N10. In addition, the presence of excess Ti^{3+} cations in M3N10 also might affect the morphology of its microstructure. The stronger lattice distortion caused by additional cation disordering induces a stronger anisotropic CTE. Since it means a larger $\Delta\alpha$, the required critical grain size for microcracking becomes smaller, and hence the cracking mode can be changed.

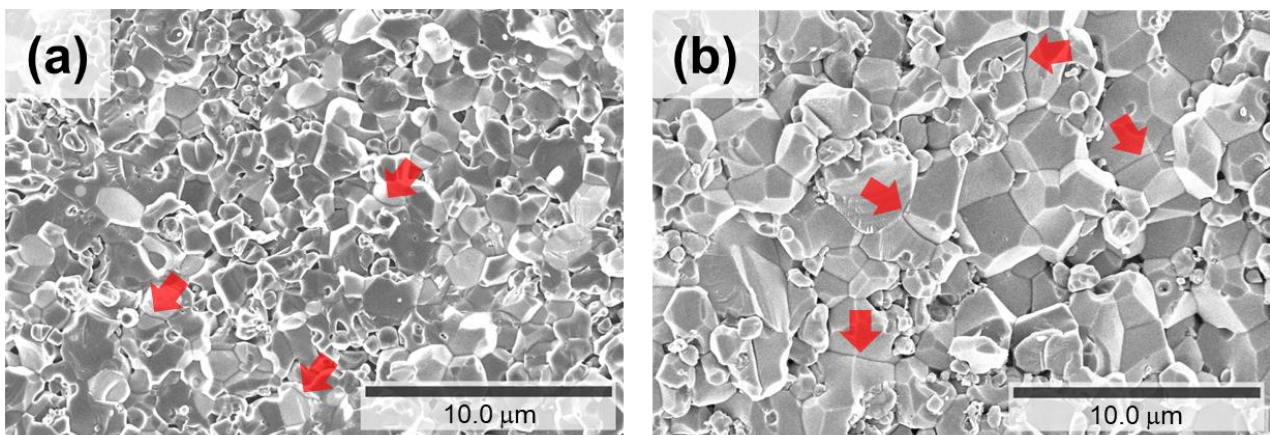


Figure 2.12. SEM images of fracture surface of the sintered samples containing 10 vol.% TiN sintered with different TiO_2/MgO ratio; (a) M1N10 and (b) M3N10. The initial molar ratios of TiO_2/MgO of M1N10 and M3N10 are 2.00 and 2.67, respectively. The arrows indicate some representative microcracks.

Typically, cracking can be a problem for ceramics under thermal cycling. However, the pseudobrookite-type materials, which contain microcracks, have some advantages in their thermomechanical properties compared to other ceramics under heat cycles. During heating, adjacent grains are thermally expanded into the cracks until they are closed. Therefore, the bulk sample exhibits a relatively low thermal expansion until cracks are closed, and hence less thermal stress is applied in the material compared to other ceramics, which do not contain microcracks. Closed cracks during heating are opening again during cooling. These phenomena are termed “microcrack healing and

reopening” [23]. Consequently, pseudobrookite-type materials exhibit an excellent level of thermal shock resistance due to the microcrack healing and reopening phenomena, and thus it can be expected that the deterioration in thermomechanical properties of MgTi_2O_5 by repeating thermal cycles is not significant.

2.3.4 Thermoelectric properties

Figure 2.13 shows the temperature dependences of electrical conductivities of sintered samples. All of the samples exhibited semiconducting behavior, with electrical conductivity increasing with temperature. The lowest electrical conductivity, $\sim 1.8 \times 10^{-2}$ S/m, was obtained for the M1N0 sample at 373 K, which is comparable to the reported value of bulk MgTi_2O_5 at 1273 K [5]. Maximum value of M1N0, ~ 4.9 S/m, at 973 K, is ~ 250 times higher than bulk MgTi_2O_5 , despite being measured at 300 K lower temperature. This remarkable improvement of electrical conductivity implies the presence of oxygen vacancies formed during SPS, which is attributed to its strong reductive atmosphere by graphite die and vacuum ($\sim 2\text{-}4$ Pa). Meanwhile, electrical conductivity increases of 3 to 5 orders at 373 K were realized by adding TiN. It is indicated that TiN acts as a path for the electrical current. The maximum electrical conductivity, 8.1×10^3 S/m, was obtained for M1N30 at 973 K.

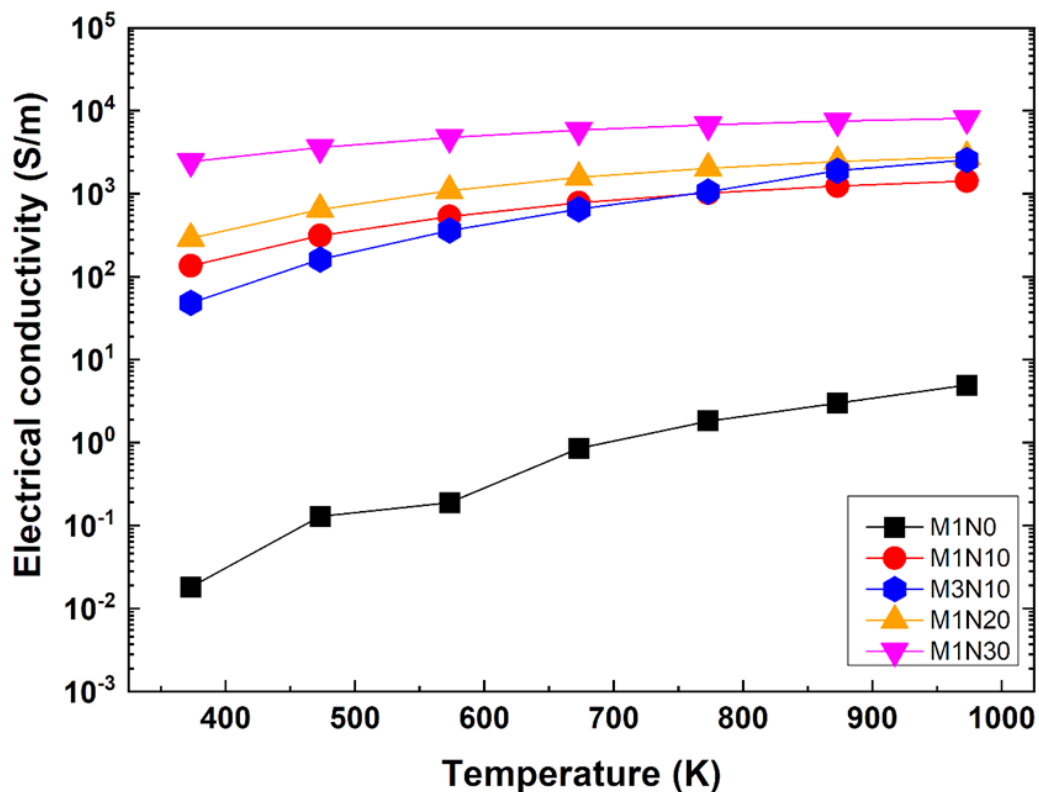


Figure 2.13. The temperature dependences of electrical conductivities of MgTi_2O_5 and $\text{MgTi}_2\text{O}_5/\text{TiN}$ composites prepared by reactive SPS.

The dominant conducting mechanism of pseudobrookite-type materials have been described as the small polaron hopping (SPH) model, since localized charge carriers in a solid induce atomic displacements of their surrounding atoms from their equilibrium positions [24,15]. For the SPH model, the conductivity is given by:

$$\sigma = \frac{\sigma_0}{T} \exp\left(-\frac{E_A}{kT}\right) \quad (2.10)$$

where σ_0 is a pre-exponential factor, E_A is the conductivity activation energy, k is Boltzmann constant, and T is the absolute temperature. For M1N0, M1N10 and M1N20 samples, the fitted lines of $\ln(\sigma T)$ to T^{-1} show that the temperature dependences of their electrical conductivities generally follow the SPH model (**Fig. 2.14**).

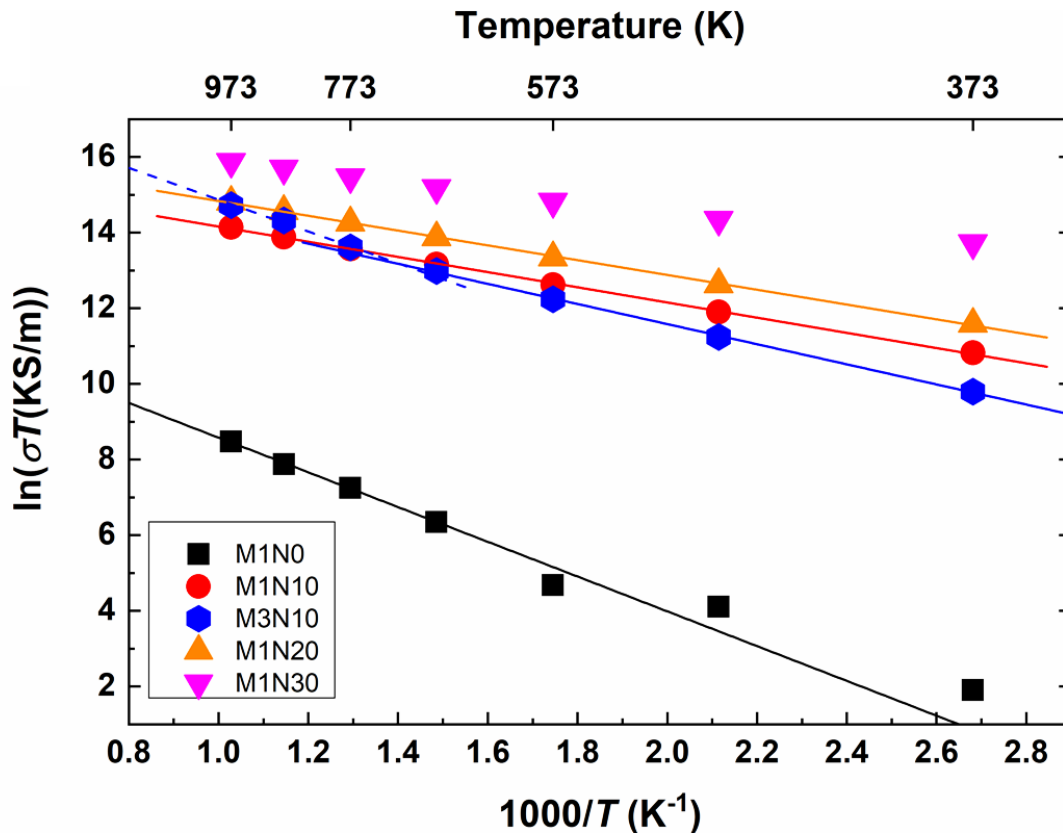


Figure 2.14. Temperature dependence of electrical conductivity of each sintered sample. The $\ln(\sigma T)$ is plotted versus T^{-1} for SPH model. The straight lines for M1N0, M1N10, M3N10 and M1N20 samples indicate the fit to Eq. 2.10.

On the other hand, for M3N10, the fitted line of $\ln(\sigma T)$ exhibits two different linearities with increasing temperature. The activation energy of M3N10 appears to be changed above 673 K. Since this temperature where the linearity is changed, matches where the temperature dependence of its thermal conductivity was changed, it is also considered that this change might be related to the cation disordering. Meanwhile, M1N30 appears to not be as good a fit to the SPH dependence as it shows a curvature over a wide temperature range. The presence of larger amount of TiN compared to other samples can be considered to influence the conduction behavior.

The measured Seebeck coefficient values are shown in **Fig. 2.15**. All samples exhibited negative Seebeck coefficient values, which indicates n-type. The absolute value decreases by adding TiN. TiN is a conductive metal with small Seebeck coefficient, so the trend is an understandable composite effect.

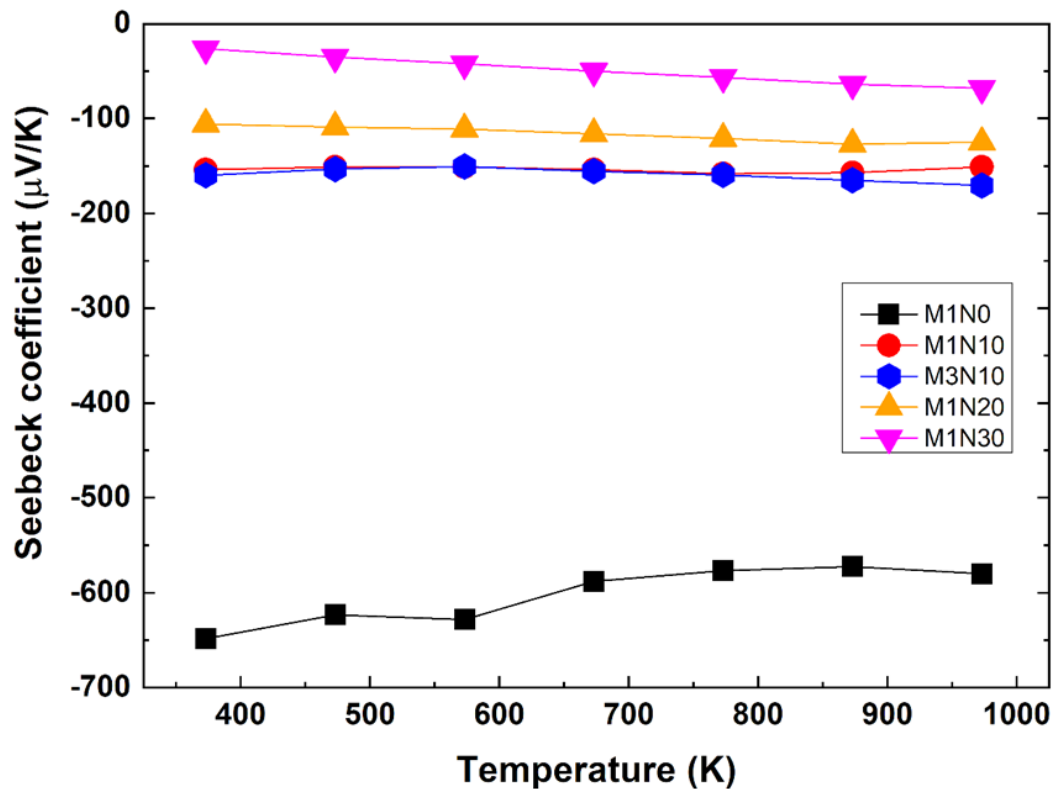


Figure 2.15. The temperature dependences of Seebeck coefficients of MgTi_2O_5 and $\text{MgTi}_2\text{O}_5/\text{TiN}$ composites prepared by reactive SPS.

Seebeck coefficients are plotted versus inverse T in **Fig. 2.16**. For an n-type semiconductor which follows SPH conduction mechanism, the Seebeck coefficient can be expressed as temperature-dependent and -independent terms. The temperature-dependent term is given by:

$$S = -\left(\frac{k}{e}\right)\left(\frac{E_S}{kT} + A\right) \quad (2.11)$$

where k is Boltzmann constant, e is the carrier charge, E_S is the characteristic carrier-generation energy, T is the absolute temperature, and A is the heat-of-transport constant.

Meanwhile, the temperature-independent term is given by Heikes formula [24]:

$$S = -\left(\frac{k}{e}\right)\ln\left(\frac{(1-c)}{c}\right) \quad (2.12)$$

where c is the carrier concentration per site. Seebeck coefficient of M1N0 decreases with increasing temperature due to an increase of carrier concentration by thermal activation. The composites show smaller values and a very broad peak behavior, which can be a combination of the SPH behavior of the host, and the metal with dependence $\propto T$ [25].

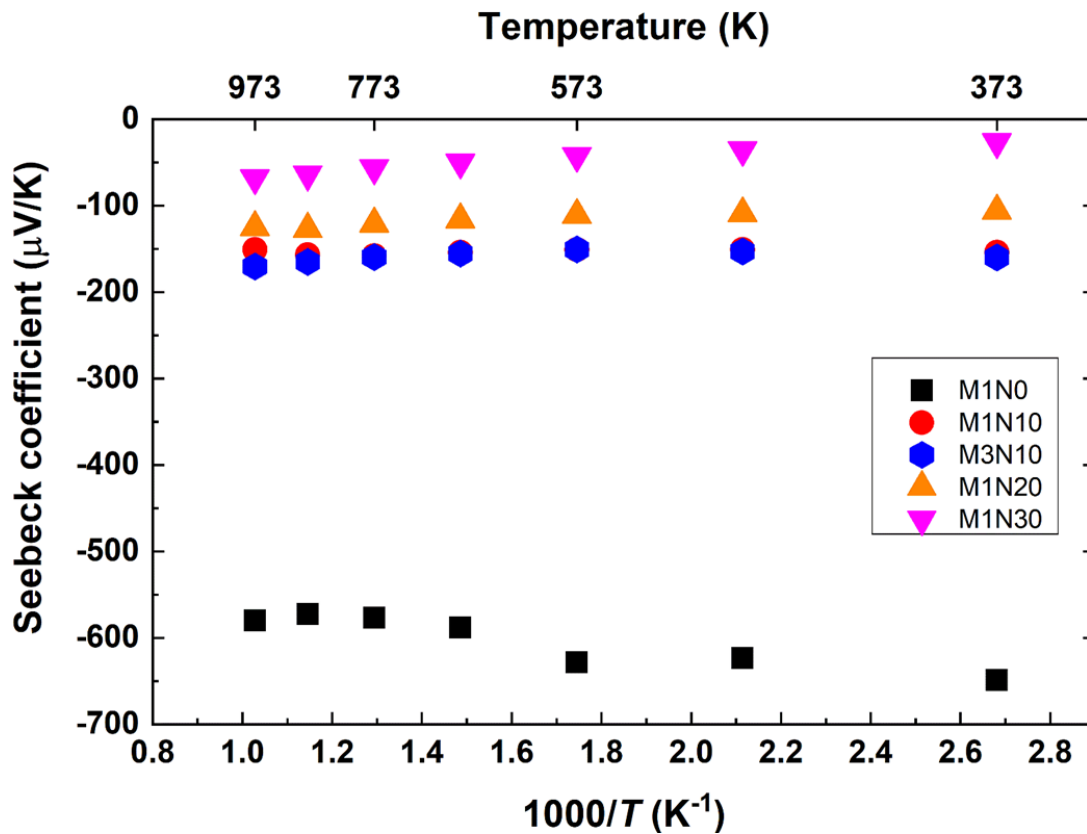


Figure 2.16. Temperature dependence of Seebeck coefficient of each sintered sample. The Seebeck coefficients are plotted versus T^{-1} for SPH model.

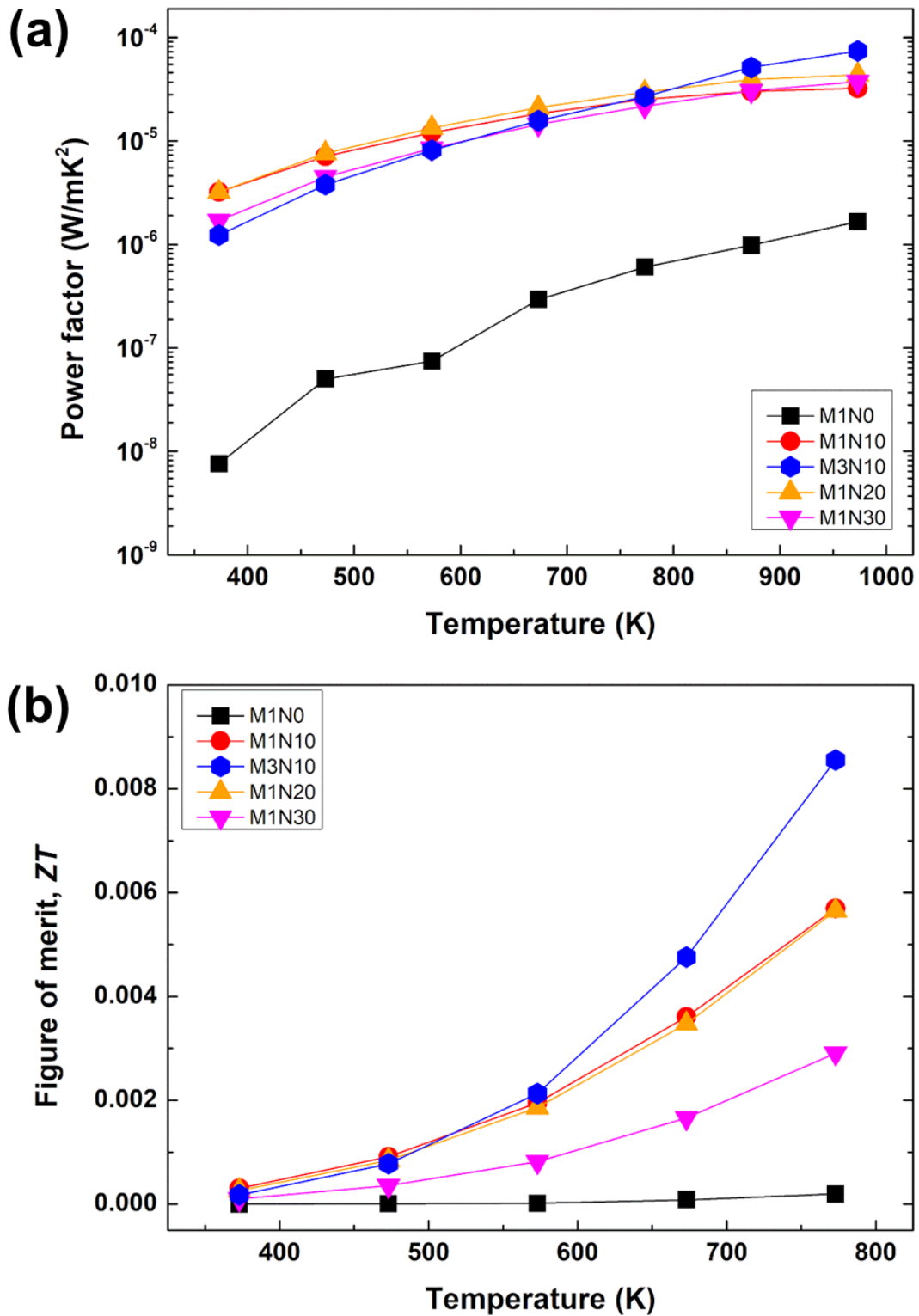


Figure 2.17. The thermoelectric properties of sintered samples; (a) power factor and (b) ZT values. The ZT values were calculated from power factors and thermal conductivities up to 773 K.

Figure 2.17 shows the power factor and ZT value of each sample. The power factor increases with increasing temperature. Though Seebeck coefficients decreased by adding TiN, electrical conductivities remarkably improved, and hence the composites exhibit higher values compared to non-composite. The maximum value of power factor, $7.4 \times 10^{-5} \text{ W/mK}^2$, was obtained for M3N10 at 973 K. Figure of merit, ZT value was calculated up to 773 K from the power factor and thermal conductivity values. The maximum ZT value, 0.009, was obtained for M3N10 at 773 K. It is expected that higher ZT values for this composite could be obtained at higher measuring temperatures.

2.4 Summary

In this study, the thermoelectric properties of MgTi₂O₅-based conductive composite materials with various TiN contents were investigated as new n-type high temperature functional materials. Regarding the electrical conductivity of MgTi₂O₅, a large enhancement (>250 times) was achieved for the first time by formation of oxygen vacancies. This unprecedented electrical conductivity for MgTi₂O₅, and the thermoelectric power factor were further remarkably improved by compositing with TiN, which yielded a conductivity enhancement of ~125,000 times. This suggests a possibility of a new kind of doping control technique for this material.

The microcracks in bulk effectively suppressed an increase of thermal conductivity. The lowest thermal conductivity was obtained for M3N10 due to lattice distortions induced by two kinds of cation disordering, Mg²⁺/Ti⁴⁺ and Ti³⁺/Ti⁴⁺. Consequently, the maximum *ZT* value, 0.009, was obtained for M3N10 at 773 K. While this value is still not high, forming such composites seems an effective strategy for enhancing thermoelectric properties of insulating materials considering its large enhancement of *ZT* compared to that of the base material, although it is likely not as straightforward to enhance materials which have high *ZT* to begin with.

2.5 References

- [1] G. Bayer, *J. Less-Common Met.*, **24**, (1971) 129-138.
- [2] N.E. Brown, A. Navrotsky, *Am. Mineral.*, **74** (1989) 902-912 .
- [3] Y. Suzuki, Y. Shinoda, *Sci. Technol. Adv. Mater.*, **12** (2011) 034301-034306.
- [4] H.-W. Son, R.S.S. Maki, B.-N. Kim, Y. Suzuki, *J. Ceram. Soc. Jpn.*, **124** (2016) 838-840.
- [5] R.S.S. Maki, Y. Suzuki, *J. Ceram. Soc. Jpn.*, **124** (2016) 1-6.
- [6] J.F. Shackelford, in: W. Alexander (Ed.), *CRC Materials Science and Engineering Handbook*, CRC Press (2001).
- [7] Y. Sugawara, Y. Kunihiro, S. Sugiyama, K. Fuda, *J. Jpn. Soc. Powder Powder Metall.*, **60** (2013) 60-65.
- [8] K. Uematsu, M. Nakamura, Z. Kato, N. Uchida, K. Saito, *J. Ceram. Soc. Jpn.*, **97** (1989) 63-67.
- [9] M. Mikami, K. Ozaki, *J. Phys.: Conf. Ser.*, **379** (2012) 012006.
- [10] H. Liu, H. Ma, T. Su, Y. Zhang, B. Sun, B. Liu, L. Kong, B. Liu, X. Jia, *J. Materiomics.*, **3** (2017) 286-292.
- [11] F. Cheng, G. Lin, X. Hu, S. Xi, K. Xie, *Nat. Commun.*, **10** (2019) 3618.
- [12] J.S. Anderson, B.G. Hyde, *J. Phys. Chem. Solids.*, **28** (1967) 1393-1408.
- [13] L. Liborio, N. Harrison, *Phys. Rev. B.*, **77** (2008) 104104.
- [14] M. Steinbrück, A. Feltz, *Z. Anorg. Allg. Chem.*, **594** (1991) 157-166.
- [15] H.-J. Steiner, X. Turrillas, B.C.H. Steele, *J. Mater. Chem.*, **2** (1992) 1249-1256.
- [16] I.E. Grey, C. Li, I.C. Madsen, *J. Sol. Stat. Chem.*, **113** (1994) 62-73.
- [17] M. He, B. Winkler, J.D. Bauer, L. Bayarjargal, J. Ruiz-Fuertes, I. Alencar, W. Morgenroth, K. Refson, V. Milman, *J. Alloy. Compd.*, **699** (2017) 16-24.
- [18] R.M. Hazen, H. Yang, *Science*, **277** (1997) 1965-1967.
- [19] M. He, B. Winkler, J.D. Bauer, L. Bayarjargal, J. Ruiz-Fuertes, I. Alencar, W. Morgenroth, K. Refson, V. Milman, *J. All. Compd.*, **699** (2017) 16-24.
- [20] H. Yang, R.M. Hazen, *J. Sol. Stat. Chem.*, **138** (1998) 238-244.

- [21] H. Yang, R.M. Hazen, *Am. Mineral.*, **84** (1999) 130-137.
- [22] J.J. Cleveland, R.C. Bradt, *J. Am. Ceram. Soc.*, **61** (1978) 478-481.
- [23] I.J. Kim, L.J. Gauckler, *J. Ceram. Process. Res.*, **9** (2008) 240-245.
- [24] C. Chen, F. Giovannelli, J.-R. Duclère, F. Delorme, *J. Eur. Ceram. Soc.*, **37** (2017) 4681-4685.
- [25] M. Jonson, G.D. Mahan, *Phys. Rev. B*, **21** (1980) 4223-4229.

Chapter 3

New Synthesis Route for Complex Borides; Rapid Synthesis of Thermoelectric Yttrium Aluminoboride via Liquid-Phase Assisted Reactive Spark Plasma Sintering

3.1 Introduction

$Y_xAl_yB_{14}$ with orthorhombic structure [1], has been found to exhibit p- and n-type characteristics. Y and Al atoms partially occupy interstitial sites among B_{12} icosahedra clusters as shown in **Fig. 3.1**. The thermoelectric behavior is changed from p-type to n-type by controlling Al occupancy. $Y_xAl_yB_{14}$ also has high melting point and excellent hardness, and thus it is expected to be a promising candidate for high temperature thermoelectric applications [2,3-6].

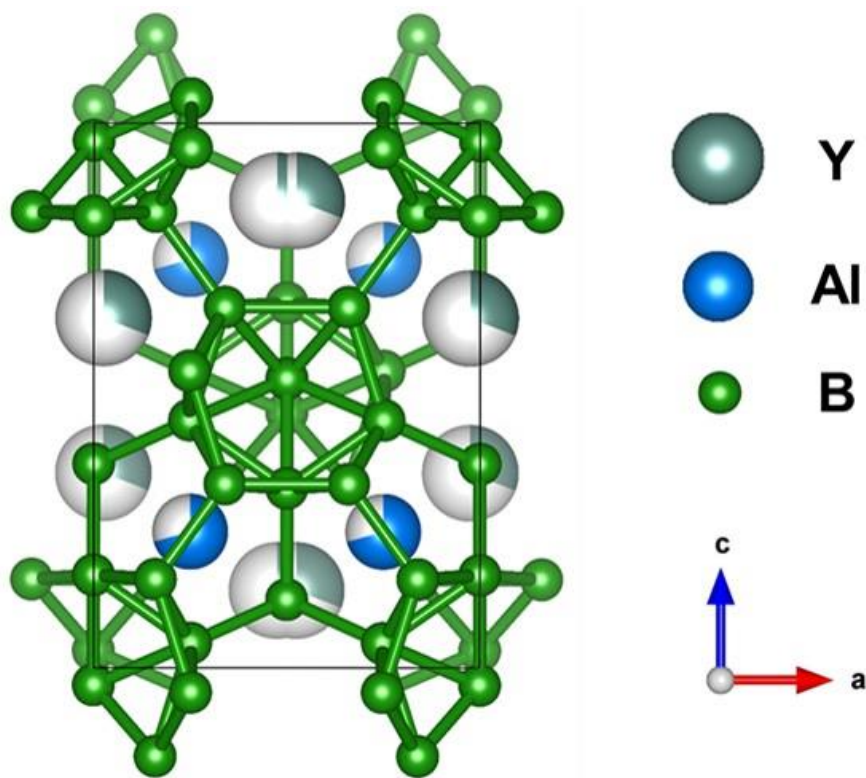


Figure 3.1. Crystal structure of $Y_xAl_yB_{14}$, which is orthorhombic structure belonging to *Imma* space group [1]. The boron atoms B1, B3, B4 and B5 form B_{12} icosahedra structures, which are interconnected via external B-B bonds or via B2 atom. Y and Al atoms partially occupy interstitial positions in the rigid three-dimensional B network.

Maruyama *et al.* and Sahara *et al.* [3-6] have reported thermoelectric properties and microstructure of polycrystalline $Y_xAl_yB_{14}$ ceramics with a various range of Al occupancy. $Y_{0.57}Al_yB_{14}$ samples were synthesized with excess Al ($y=2.8-5.6$) serving as flux, by sintering in induction furnaces for 8-12 h at 1400-1500°C. To prepare dense bulk samples, the synthesized samples were pulverized, washed in NaOH solution, dried, and then sintered again by SPS. The flow chart of conventional synthesis process for $Y_xAl_yB_{14}$ is demonstrated in **Fig. 3.2**.



Figure 3.2. Flow chart of conventional synthesis process for bulk $Y_xAl_yB_{14}$. It consists of 7 steps, and the total process time is ≥ 3 days.

However, in spite of using SPS, relative densities of obtained n-type $Y_xAl_yB_{14}$ ($x \sim 0.56$; $0.57 \leq y \leq 0.63$) samples exhibited quite low values (71.1-89.4%) due to its poor sinterability. Furthermore, the previous synthesis method required a waste of resources by evaporation of large amounts of Al during the synthesis, and more importantly also requiring a complicated and time consuming total process [3-6]. This synthesis issue can be said to be a problem for many complex borides discovered with interesting electrical, magnetic, thermoelectric, and mechanical properties [7,8]. It is thus needed to develop a new, simple and reasonable synthesis process for complex borides.

Recently, for synthesis and sintering of materials, which have poor sinterability, reactive SPS techniques and development of sintering additives have been studied. Son *et al.* reported about fabrication of translucent AlN by SPS with MgF_2 , which was used as a sintering additive [9]. In general, AlN is also difficult to attain full densification due to its high covalent bonding. In that study, the liquid phase formed by MgF_2 assisted sintering, and as a result, fully densified and translucent samples were obtained with short sintering time (20 min). Densification of complex borides which do not melt stably and have an upper limit on temperatures which can be used for sintering, are an even more difficult problem. For example, different sintering conditions [10,11] and sintering aids were tried for the metal borocarbonitrides which are attractive thermoelectric materials, with some effective sintering aids found, but which were detrimental to the properties.

In this study, a new approach with reactive SPS is investigated to synthesize and prepare dense n-type $Y_xAl_yB_{14}$ ceramics. As a new sintering additive, AlF_3 is used. It is expected that AlF_3 can enhance sinterability by forming a liquid phase during sintering due to its relatively low melting point.

3.2 Experimental procedure

3.2.1 Synthesis

Commercially available YB_4 (99.9%, Japan New Metals Co., Ltd.), AlB_2 (Sigma-Aldrich Co., Ltd.), amorphous B (99%, New Metals and Chemicals Co., Ltd.) and AlF_3 (Wako Co., Ltd.) powders were used as the starting materials. YB_4 and AlB_2 were selected as the precursor for reactive sintering, and AlF_3 was selected as the sintering additive. The powders of YB_4 , AlB_2 , B and 0-1 wt.% AlF_3 were simply mixed under ethanol for 30 min using SiO_2 mortar with nominal compositions of $Y_{0.62}Al_yB_{14}$, where $y=0.71, 1.24, 1.55$ and 1.86 . For $y=0.71$ (YA0 samples), five different sintering conditions were tested; 10 min and 1 h under the uniaxial pressure of ~ 30 MPa, each with and without AlF_3 , and 5 min under the uniaxial pressure of 80 MPa with AlF_3 . Subsequent samples YA1, YA2 and YA3 were prepared with AlF_3 additive and 1 h sintering time. The excess amount of Al ($y=1.24-1.86$) was used to prepare Al-rich n-type yttrium aluminoborides, as shown in **Fig. 3.3**.

The powder mixtures were dried at $100^\circ C$ for 3 h in an oven, and then poured into a 10 mm diameter graphite die. Herein, graphite paper was used as a release agent. The mixtures were heated up to $1500^\circ C$ in a SPS apparatus (Dr. Sinter, Fuji Denpa Koki Co., Ltd.) with heating rate of $100^\circ C/min$, and then reactively sintered at $1500^\circ C$ for 5-60 min under uniaxial pressure of 28-80 MPa in a reduced-pressure Ar atmosphere (-0.03 MPa). After sintering, the samples were cooled down with cooling rate of $200^\circ C/min$, and finally, the sintered discs, 10 mm in diameter and ~ 2 mm in thickness, were obtained.

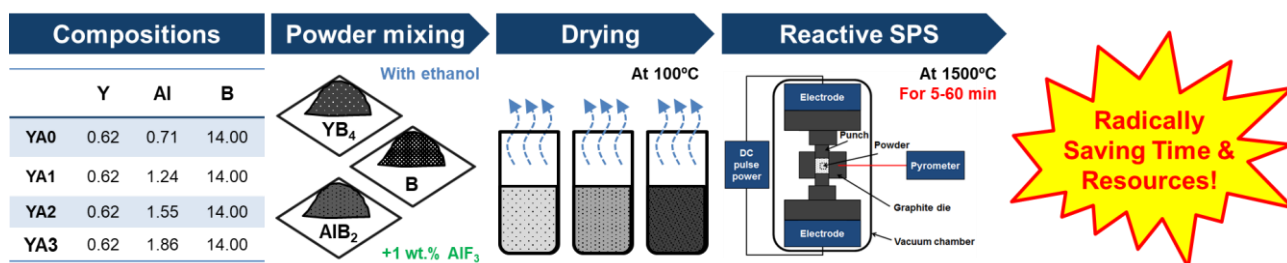


Figure 3.3. Flow chart of newly developed synthesis process for bulk $Y_xAl_yB_{14}$ in this study.

3.2.2 Characterizations

After SPS, as-sintered samples were slightly grinded by a diamond plate (#400) to remove the graphite paper on their surface. The densities of grinded samples were measured using Archimedes' method. The constituent phases of sintered samples were analyzed by X-ray diffraction (XRD, Smart lab 3, Rigaku) with $Cu K\alpha$ radiation ($\lambda=1.5418$ Å). The XRD patterns were collected at $2\theta=10-90^\circ$ with in a step of 0.01° . The compositions of the prepared

$Y_xAl_yB_{14}$ samples by reactive SPS were estimated from Rietveld refinement using FullProf software. The thermal diffusivity of each sample was measured from 373 to 973 K by using a laser flash analysis apparatus (LFA, TC-7000, ADVANCE RIKO, Inc.). Prior to the LFA, the samples were coated with carbon. After LFA, samples were cleaned to remove the carbon on their surfaces, and then machined into bar-shaped specimens by cutting machine. The electrical resistivity and Seebeck coefficient of the specimens were evaluated from 373 to 973 K using a thermoelectric tester (ZEM-2, ADVANCE RIKO, Inc.). The specific heat capacities of the samples were measured from 313 to 1073 K using a high temperature differential scanning calorimetry (STA449F3-NT24, NETZSCH Japan Co., Ltd.). As crucibles, Pt pans, Pt lids and Alumina liner were used. Microstructure of fracture surfaces of each sample was observed by scanning electron microscopy (SEM, S-4800, Hitachi High-Technologies Co.). To investigate the components of matrix and secondary phases on the fracture surface, energy-dispersive X-ray spectroscopy (EDX, Hitachi High-Technologies Co.) was used.

3.3 Results and discussion

3.3.1 Phase identification

Figure 3.4 and **3.5** show the XRD patterns measured on the surface of YA0 composition samples sintered with and without AlF_3 at 1773 K, respectively. The XRD pattern of sample sintered for 10 min without AlF_3 exhibits numerous peaks of secondary phases such as unreacted YB_4 , YB_6 , YB_{12} , α -alumina, and so on, as shown in **Fig. 3.4**. The peaks of secondary phases are still detected on the YA0 composition sample which were even sintered for 1 h. It means that the reaction for synthesis of $\text{Y}_x\text{Al}_y\text{B}_{14}$ is independent on sintering time in this case.

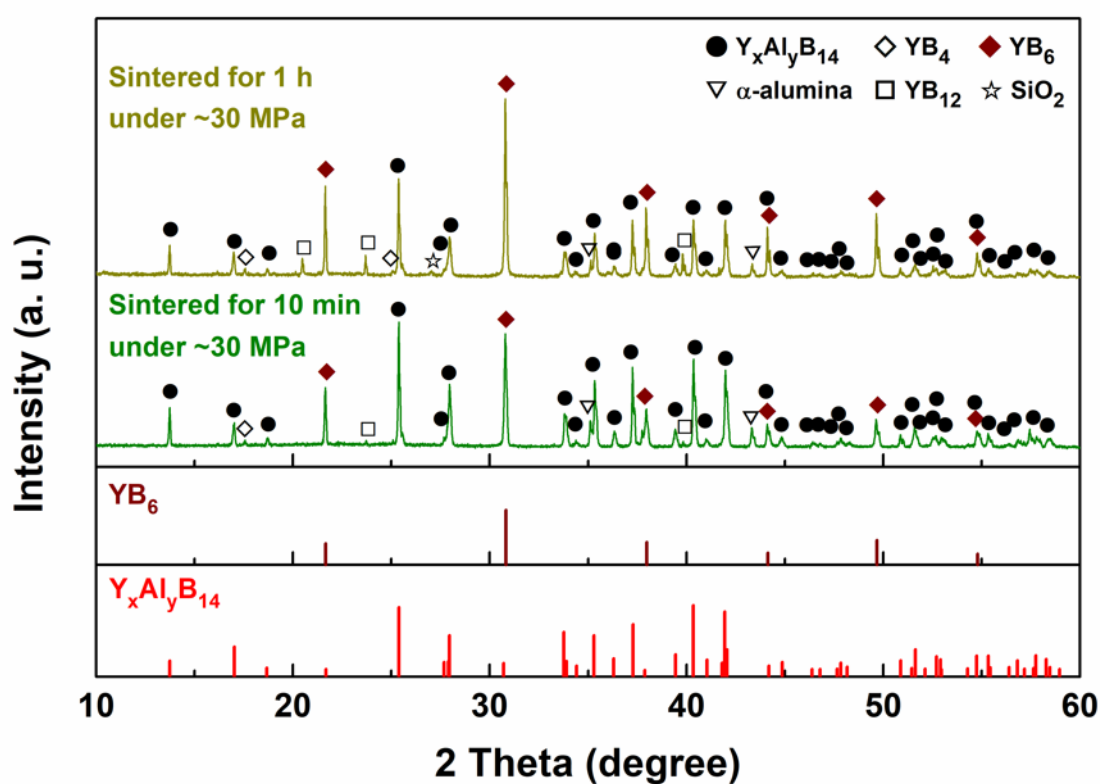


Figure 3.4. XRD patterns of YA0 composition ($\text{Y}_{0.62}\text{Al}_{0.71}\text{B}_{14}$) samples prepared by reactive SPS without AlF_3 addition. The samples were sintered at 1500°C under uniaxial pressure of ~ 30 MPa in a reduced Ar atmosphere for 1 h and 10 min, respectively. The standardized intensities for $\text{Y}_x\text{Al}_y\text{B}_{14}$ and YB_6 are shown with sample's XRD patterns.

In contrast, the XRD patterns of the same composition samples sintered with AlF_3 at the same sintering condition exhibit relatively much less peaks of secondary phases, and no peak of AlF_3 was detected. It implies that AlF_3 dramatically improves the reactivity among starting materials by liquid phase sintering, and then was completely

removed without remaining by evaporation under the reduced Ar atmosphere. The dense and relatively purest $Y_xAl_yB_{14}$ was obtained for the sample sintered for 5 min under the uniaxial pressure of 80 MPa with AlF_3 (**Fig. 3.5**). Although some peaks of α -alumina and YB_6 phases are still detected as in the previous conventional synthesis study [3,4], polycrystalline $Y_xAl_yB_{14}$ was successfully synthesized via reactive SPS with AlF_3 .

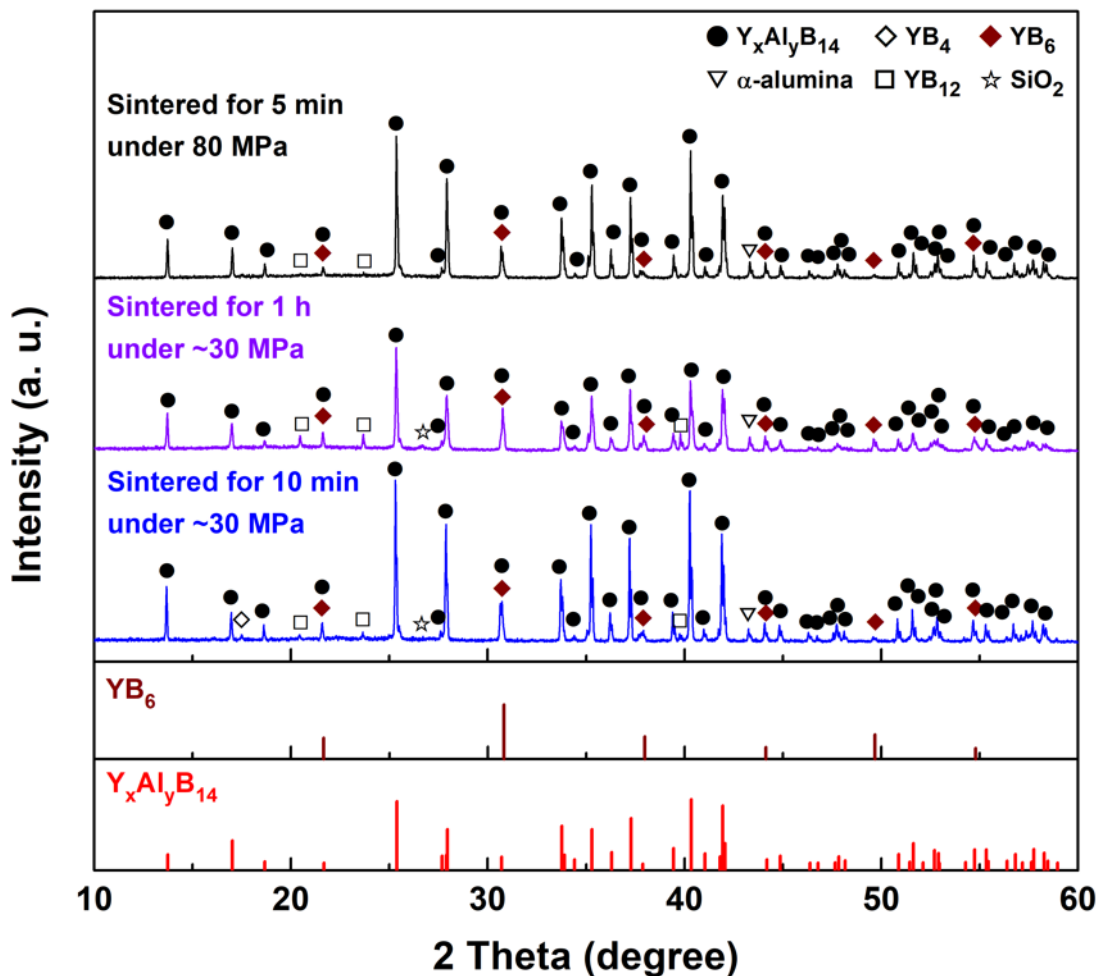


Figure 3.5. XRD patterns of YA0 composition ($Y_{0.62}Al_{0.71}B_{14}$) samples prepared by reactive SPS with AlF_3 addition. The samples were sintered at 1500°C in a reduced Ar atmosphere for 1 h and 10 min under the uniaxial pressure of ~30 MPa, and for 5 min under the uniaxial pressure of 80 MPa, respectively. The standardized intensities for $Y_xAl_yB_{14}$ and YB_6 are shown with sample's XRD patterns.

The axial displacement changes of the YA0 composition samples during SPS are shown in **Fig. 3.6**. The temperature at the minimum displacement indicates the starting initial stage of sintering. In the case of the sample sintered without AlF_3 under ~30 MPa which is the minimum pressure of SPS, the shrinkage was started at ~1280°C

but densification was not finished even at 1500°C. On the other hand, in the case of the sample sintered with AlF₃ under ~30 MPa, the shrinkage was started at ~1180°C and densification occurred well during heating process. This result suggests that the sinterability and densification behavior were remarkably improved by AlF₃. The melting point of AlF₃ is ~1300°C at 1 atm. This temperature is higher than that for the starting shrinkage (~1180°C). It is therefore considered that the reduced-pressure Ar atmosphere lowered the melting point of AlF₃, and hence the initial stage was shifted earlier, namely ~100°C lower by formation of liquid phase of AlF₃.

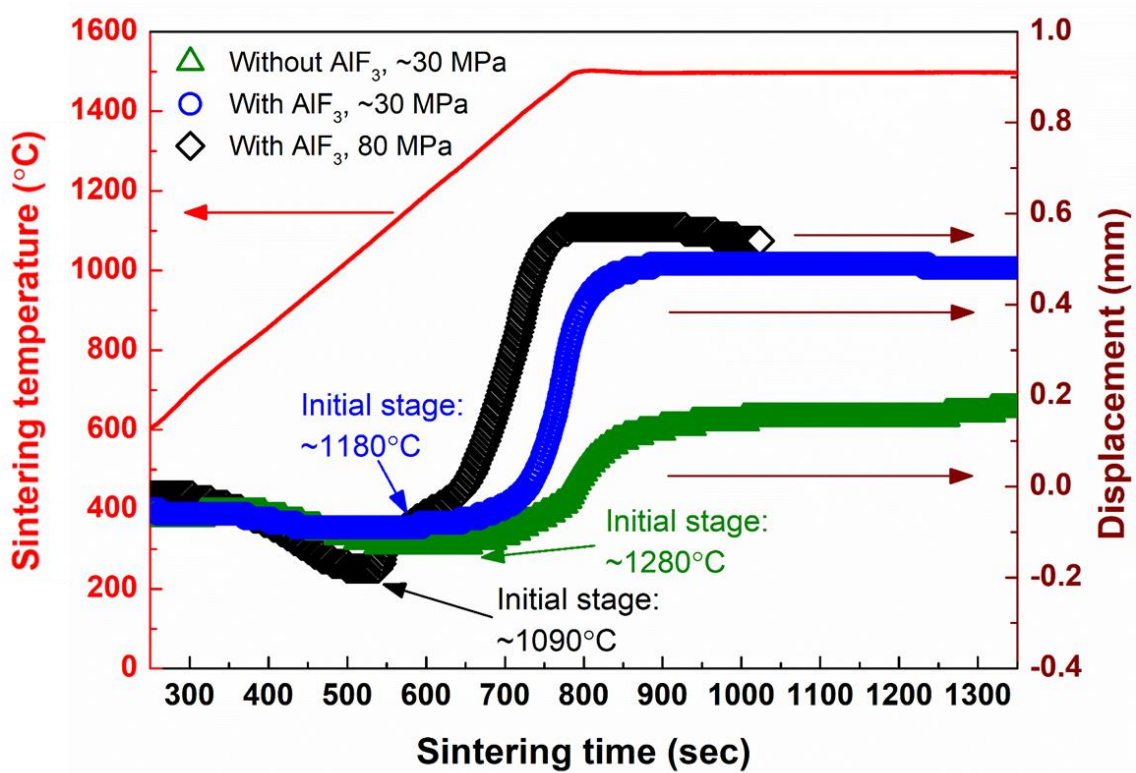


Figure 3.6. Densification behavior of Y_xAl_yB₁₄ sintered without AlF₃ under ~30 MPa, with AlF₃ under ~30MPa, and with AlF₃ under 80 MPa. To investigate the effect of AlF₃ to densification, same amount of mixture and same graphite die and spacers were used.

The densification behavior of the YA0 composition sample sintered with AlF₃ under uniaxial pressure of 80 MPa was further enhanced. The shrinkage of the pressure-assisted sample was started from ~1090°C, and the shrinkage rate was changed from ~1180°C. Since the temperature where shrinkage rate was changed is the same as the temperature of the starting initial stage of the sample sintered with AlF₃ under ~30 MPa, the shrinkage observed from 1090 to 1180°C indicates the effect of the applied pressure. All samples exhibited changes of shrinkage rate during the intermediate stage. These phenomena can be mainly attributed to the different shrinkage rate between

the main phase and the secondary phases.

Figure 3.7 shows XRD patterns of $Y_{0.62}Al_yB_{14}$ samples (YA0-3; $y=0.71-1.86$) sintered at 1500°C with AlF_3 for 1 h under ~ 30 MPa. Together with the prominent peaks of $Y_xAl_yB_{14}$, weak peaks of several secondary phases such as α -alumina, σ -alumina, YB_4 , YB_6 , YB_{12} and SiO_2 were detected. The Al-poor sample (YA0) exhibited peaks of α -alumina, YB_6 , YB_{12} and SiO_2 , whereas the Al-rich samples (YA1, YA2 and YA3) exhibited peaks of σ -alumina in addition.

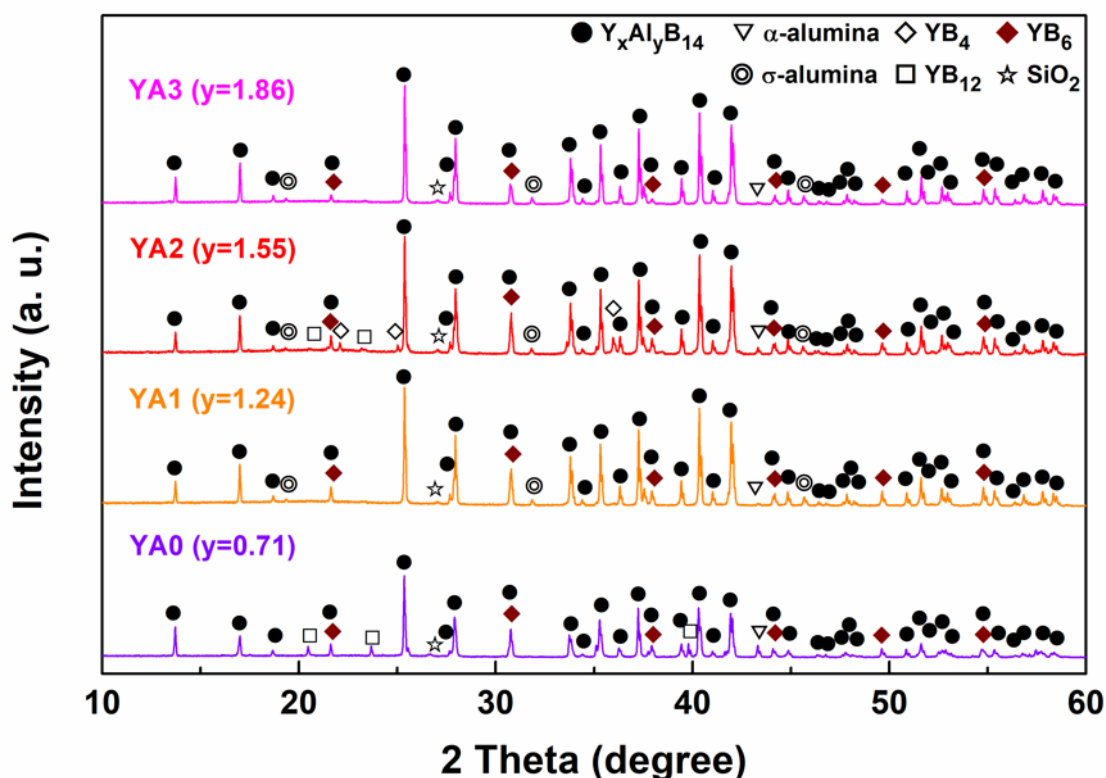


Figure 3.7. XRD patterns of YA0, YA1, YA2 and YA3 composition ($Y_{0.62}Al_yB_{14}$; $y=0.71-1.86$) samples prepared by reactive SPS with AlF_3 addition. The samples were sintered at 1500°C under uniaxial pressure of ~ 30 MPa in a reduced Ar atmosphere for 1 h.

The structure of σ -alumina ($Al_{2.667}O_4$) is described as a defect cubic spinel in which Al cations randomly and partially occupy its octahedral and tetrahedral sites [12]. The result thus implies that addition of Al and reductive atmosphere affects formation of σ -alumina during sintering of Al-rich samples. For Al-rich samples, the intensity of the detected YB_6 and YB_{12} peaks decreased with increasing Al content. It indicates that the excess Al compensated the Al loss caused by the formation of alumina phase during sintering. Relatively homogeneous yttrium aluminoborides were obtained for the YA₃ composition. The XRD pattern for the YA₂ sample shows the

presence of YB_4 . It is attributed to inhomogeneous mixing of starting materials. To obtain $Y_xAl_yB_{14}$ without secondary phases, such as SiO_2 , YB_4 , YB_6 and YB_{12} , optimization of the mixing process is required. We also found out that the SiO_2 in the XRD patterns of the samples came from the agate mortar, which was used to pulverize each sample before powder XRD measurement. This was indicated because the intensity of the peak at $2\theta=26-27^\circ$ increased with increasing pulverization time.

The fractional occupancies of x and y , of Y and Al, in the Al-poor (YA0-P) and -rich samples (YA1, YA2 and YA3) prepared by reactive SPS with AlF_3 were estimated from Rietveld refinement within the technique limit (**Fig. 3.8**). At first starting atom position from Korsukova *et al.* [1] model was used to perform refinements. Ultimately, atom positions were refined, together with partial occupancies for Y and Al positions. The synthesis conditions and the results of Rietveld refinement of each sample are summarized in **Table 3.1** and **Table 3.2**, respectively.

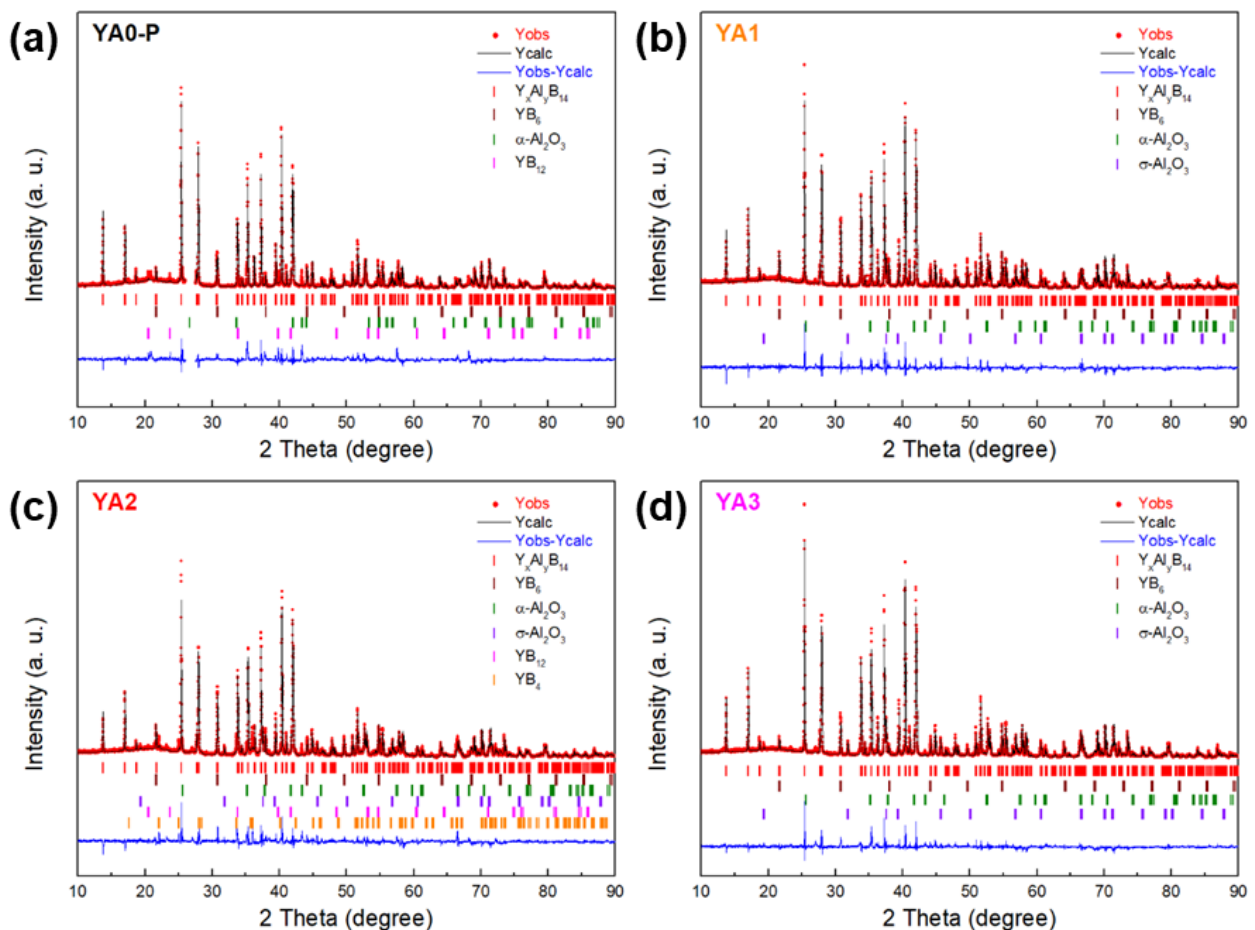


Figure 3.8. XRD pattern and the results of Rietveld refinement of YA0-P, YA1, YA2 and YA3 samples prepared by reactive SPS with AlF_3 addition. The YA0-P sample was sintered at $1500^\circ C$ for 5 min under 80 MPa, whereas the YA1, YA2 and YA3 samples were sintered at $1500^\circ C$ for 60 min under ~ 30 MPa.

Table 3.1. The synthesis conditions of $Y_xAl_yB_{14}$ samples.

Sample name	Starting composition	Sintering conditions (Temperature \times time)	Pressure (MPa)	Atmosphere
YA0-P	$Y_{0.62}Al_{0.71}B_{14}$	1500°C \times 5 min	80	Ar
YA1	$Y_{0.62}Al_{1.24}B_{14}$	1500°C \times 60 min	~30	Ar
YA2	$Y_{0.62}Al_{1.55}B_{14}$	1500°C \times 60 min	~30	Ar
YA3	$Y_{0.62}Al_{1.86}B_{14}$	1500°C \times 60 min	~30	Ar

Table 3.2. Compositions and lattice parameters of sintered samples, which were estimated from Rietveld analysis.

Sample name	Starting composition	Refined composition	a (Å)	b (Å)	c (Å)	Volume of lattice (Å ³)
YA0-P	$Y_{0.62}Al_{0.71}B_{14}$	$Y_{0.66}Al_{0.52}B_{14}$	5.825	10.401	8.205	497.107
YA1	$Y_{0.62}Al_{1.24}B_{14}$	$Y_{0.64}Al_{0.67}B_{14}$	5.812	10.416	8.190	495.805
YA2	$Y_{0.62}Al_{1.55}B_{14}$	$Y_{0.62}Al_{0.66}B_{14}$	5.811	10.414	8.188	495.503
YA3	$Y_{0.62}Al_{1.86}B_{14}$	$Y_{0.65}Al_{0.67}B_{14}$	5.811	10.413	8.189	495.516

The refined Y contents (x in $Y_xAl_yB_{14}$) of all samples are ~0.64, which is almost the same value as that of the starting materials. This result implies that no Y loss during reactive SPS occurred. The refined Al content (y in $Y_xAl_yB_{14}$) of YA0-P is 0.52 though the starting content was 0.71. It suggests that Al was lost during sintering by the formation of alumina phase, and evaporation due to high sintering temperature and reduced Ar atmosphere. Meanwhile, the refined Al contents of YA1, YA2 and YA3 are ~0.67, which are much less than their initial Al contents (1.24, 1.55 and 1.86). Since these compositions are quite similar to those determined from single crystal x-ray diffractometry $Y_{0.62}Al_{0.71}B_{14}$ [1], it is considered that the Y and Al atoms occupy their interstitial sites as maximumly as possible to satisfy the 4 electron deficient nature [7,8], and thus excess Al could not occupy Al sites.

The phase fractions and the theoretical and relative density of each sample are given in **Table 3.3**. At around 5%, the largest impurity phase is the alumina phase. As raw materials, amorphous boron is used for many sintering synthesis of complex borides which are difficult to synthesize by simple arc melting, for example [8]. There is some oxidation of the sensitive amorphous boron and in combination with aluminum for the present compound, alumina is formed. We tried to remove the oxygen by heating the amorphous boron and evaporation of BO, but found that handling in air, the amorphous boron is easily oxidized again. Therefore, in this case, the alumina impurity phase is intrinsically difficult to eliminate. However, together with metallic YB_6 , etc. which typically appear since mixing is generally not ideal, it is indicated that these secondary phases do not have a significant effect on the thermoelectric properties, as discussed below.

Table 3.3. Phase fraction of constituent phases of each sample. Both are estimated by Rietveld refinement.

Sample name	$Y_xAl_yB_{14}$ (wt.%)	YB_6 (wt.%)	$\alpha-Al_2O_3$ (wt.%)	$\sigma-Al_2O_3$ (wt.%)	YB_{12} (wt.%)	YB_4 (wt.%)
YA0-P	91.53	1.30	6.33	-	0.85	-
YA1	92.65	2.52	0.16	4.67	-	-
YA2	91.15	2.41	0.21	4.04	~0.00	2.19
YA3	93.07	0.89	0.15	5.89	-	-

3.3.2 Thermoelectric properties

The temperature dependence of electrical conductivities for Al-poor (YA0-P) and -rich samples (YA1, YA2 and YA3) prepared by reactive SPS is shown in **Fig. 3.9**. At the low temperature region, the Al-poor sample exhibits extremely low electrical conductivity compared to Al-rich samples. However, a particularly large increase of electrical conductivity is observed with increasing temperature due to its conducting mechanism which will be described below. On the other hand, all the Al-rich samples exhibit several orders higher electrical conductivities.

The highest electrical conductivity values are obtained for YA3 sample which is ~5 times higher than that of the YA1 sample. We consider the possibilities of the secondary phases having any effect on the thermoelectric properties. Amongst the thermoelectric properties, the electrical conductivity can be considered to have the potential to be most sensitive to small amounts of metallic phases or insulating phases, considering that these phases may have orders different resistivity than the main material. As an illustrative example, we compare YA1 and YA3. From the Rietveld analysis, the composition (**Table 3.2**) and phase fraction (**Table 3.3**) of the main $Y_xAl_yB_{14}$ phase is quite similar, as are the relative densities of the samples which are both close to 100% (**Table 3.3**). YA1 has a significantly larger amount of metallic YB_6 impurities and also slightly less amount of insulating alumina impurities compared to YA3. However, as noted above, the conductivity of YA1 is actually around 5 times lower than YA3, indicating that the secondary phases in this case are not having a significant effect on the thermoelectric properties.

We consider the origin of the difference in properties. The large difference between YA1 and YA3 is only the starting composition (**Table 3.2**), where the amount of initial excess Al is around 1.5 times higher for YA3. Since Al itself cannot be seen in the XRD patterns, we speculate that Al atoms may be seeded in the grain boundaries and result in an enhancement of the electrical conductivity. Such an effect has been proposed before⁵⁸ and observed in Ba seeding of $Ca_3Co_4O_9$ for example [13].

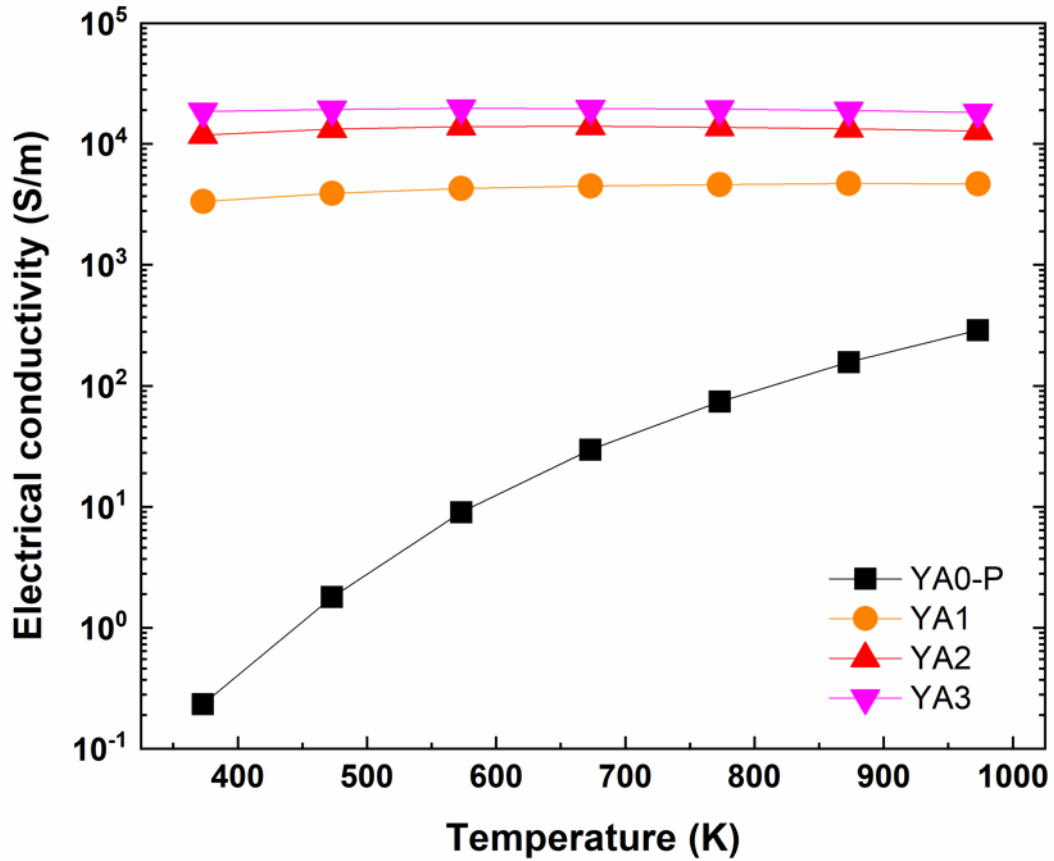


Figure 3.9. Temperature dependence of logarithmic electrical conductivities of Al-poor (YA0-P) and -rich samples (YA1, YA2 and YA3) prepared by reactive SPS. The YA0-P sample was sintered at 1500°C for 5 min under 80 MPa, whereas the YA1, YA2 and YA3 samples were sintered at 1500°C for 60 min under ~30 MPa. Error bars represent a measurement uncertainty range ($\pm 7\%$).

Figure 3.10 shows the temperature dependence of Seebeck coefficients for each sintered sample. The Seebeck coefficient of Al-poor sample exhibits positive values, whereas those of Al-rich samples exhibit negative values. This indicates that the thermoelectric behavior of $Y_xAl_yB_{14}$ samples are changed from p-type to n-type with increasing Al occupancy. The Seebeck coefficient values for Al-poor sample increases up to 473 K, and then decreases with increasing temperature. In contrast, the absolute values of negative Seebeck coefficients for Al-rich samples increase with increasing temperature. The maximum positive and negative values, 530 $\mu\text{V/K}$ and -160 $\mu\text{V/K}$, are obtained for YA0-P at 473 K and for YA1 at 973 K, respectively.

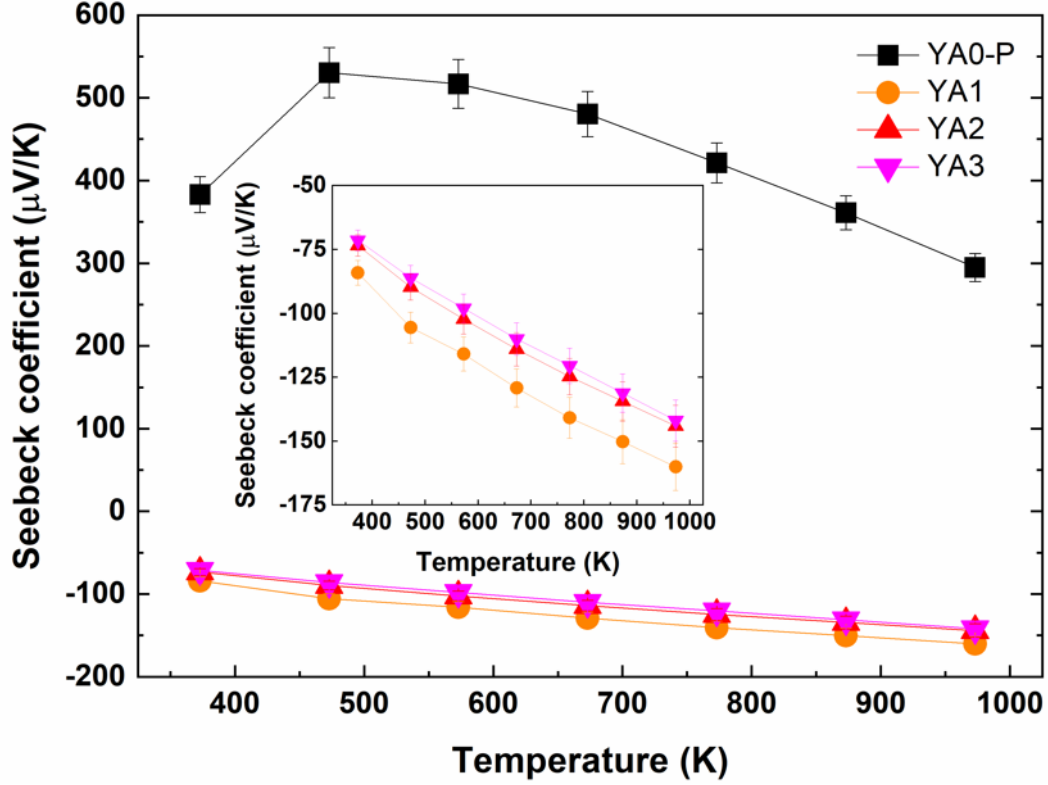


Figure 3.10. Temperature dependence of Seebeck coefficients of Al-poor (YA0-P) and -rich samples (YA1, YA2 and YA3) prepared by reactive SPS. The YA0-P sample was sintered at 1500°C for 5 min under 80 MPa, whereas the YA1, YA2 and YA3 samples were sintered at 1500°C for 60 min under ~30 MPa. The Seebeck coefficients of Al-rich samples are shown in the inset. Error bars represent a measurement uncertainty range ($\pm 7\%$).

Figure 3.11 (a) and (b) show the temperature dependence of electrical conductivity of each sintered sample in accordance with thermally activated conduction (TAC) mode and variable range hopping (VRH) mode, respectively. According to the TAC model, the conductivity is expressed as the following:

$$\sigma_{\text{TAC}} = \sigma_{0,\text{TAC}} \exp\left(-\frac{E_A}{kT}\right) \quad (3.1)$$

Meanwhile, in disordered systems, according to the VRH model, the conductivity for three dimensional systems is given by:

$$\sigma_{\text{VRH}} = \sigma_{0,\text{VRH}} \exp\left(-\frac{T_0}{T}\right)^{\frac{1}{4}} \quad (3.2)$$

where $\sigma_{0,\text{TAC}}$ and $\sigma_{0,\text{VRH}}$ are constants which do not depend on temperature, E_A is the thermal activation energy, T_0 is the characteristic temperature determined by the density of localized states near the Fermi level, k is the Boltzmann's constant and T is the absolute temperature [14].

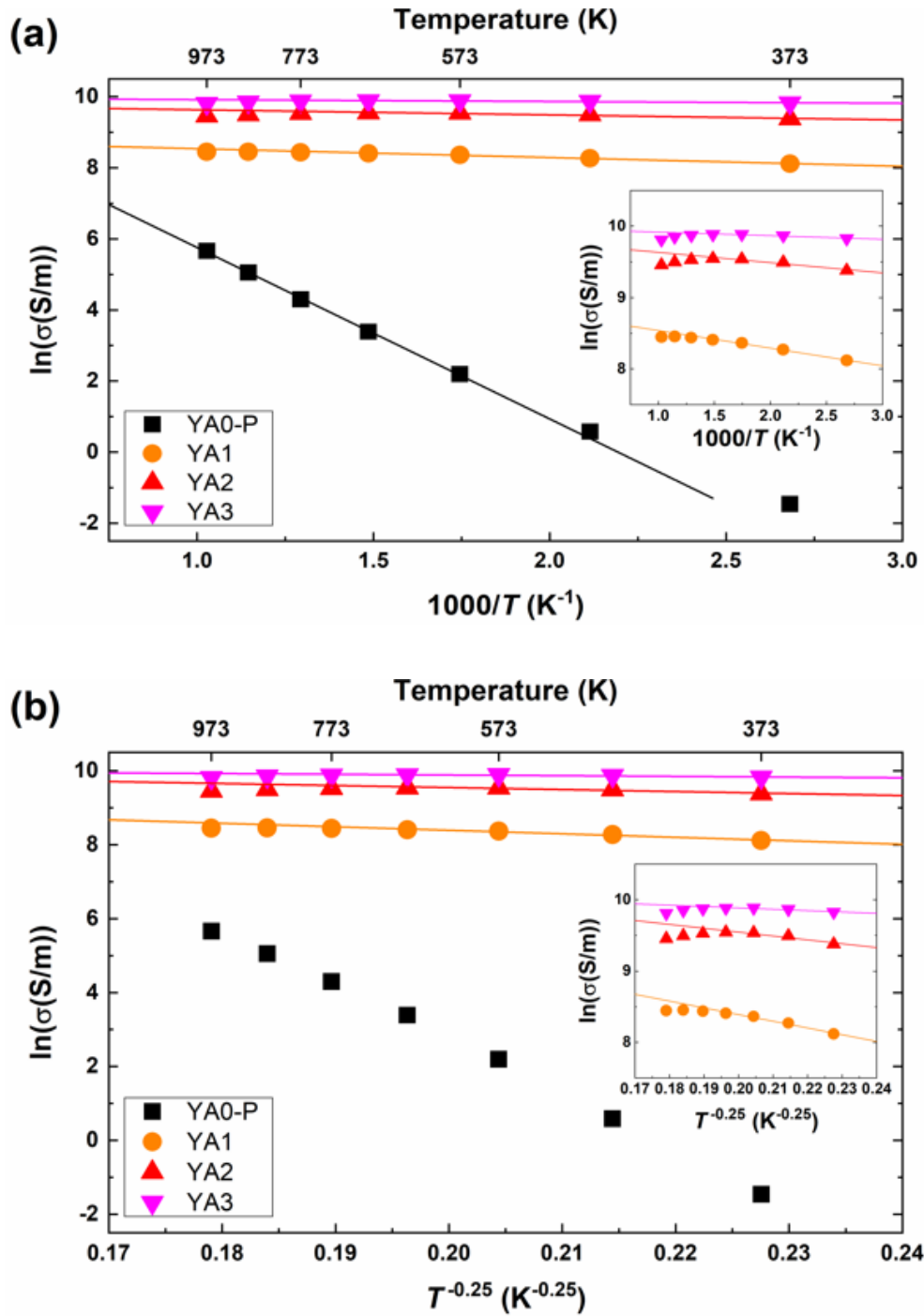


Figure 3.11. Temperature dependence of electrical conductivity of each sintered sample. The $\ln\sigma$ is plotted versus (a) T^{-1} for TAC mode and (b) $T^{-0.25}$ for VRH mode, respectively. The straight line for Al-poor sample in TAC mode expresses the fit to Eq. 1 for the temperature range from 573 K to 973 K. Also, the straight lines for Al-rich samples in TAC mode and VRH mode express the fit to Eq. 1 and to Eq. 2 for the temperature range from 373 K to 673 K, respectively.

We consider the validity of the two different conduction models for our samples. In **Fig. 3.11 (a)**, the temperature dependence of the electrical conductivity of the Al-poor sample appears to generally follow the TAC dependence, except it appears to deviate from a straight line below 573 K. In contrast, in **Fig. 3.11 (b)**, the temperature dependence of the electrical conductivity appears to not be as good a fit to the VRH dependence as it shows a curvature over a wider temperature range. This implies that TAC is the dominant conduction mechanism for Al-poor $Y_xAl_yB_{14}$ above 573 K. In this case, the calculated E_A and $\sigma_{0,TAC}$ from the fitted line are 0.4 eV and 3.95×10^4 S/m, respectively. This activation energy value is similar to the band gap energy in the result of band structure calculation for $Y_{0.50}Al_{0.75}B_{14}$ [5].

We will consider the mechanism for the low temperature deviation below together with the discussion on the Seebeck coefficient. For Al-rich samples, neither the TAC (**Fig. 3.11 (a)**) or VRH (**Fig. 3.11 (b)**) is a good fit, with the rate of increase of the electrical conductivity apparently suppressed at higher temperatures. We speculate that the reason of this suppression may be due to the presence of the Al segregation. This effect only appears to be noticeable for the highest conductive samples (i.e. Al-rich samples at high temperatures) and does not appear to be pronounced for the Al-poor sample where the level of electrical conductivity is much lower to begin with. For the Al-rich samples we attempt to obtain insight on the conduction mechanism through the temperature dependence of the Seebeck coefficient discussed below.

The temperature dependences of Seebeck coefficients for TAC and VRH are shown in **Fig. 3.12**. When the carrier concentration is increased by thermal activation, the Seebeck coefficient is generally expressed as the following [15,16]:

$$S = -\left(\frac{k}{e}\right)\left(\frac{E_s}{kT} + A\right) \quad (3.3)$$

where e is carrier charge, k is Boltzmann constant, E_s is the characteristic carrier-generation energy, T is the absolute temperature, and A is the heat-of-transport constant. However, the plots of Seebeck coefficients of all samples do not appear to have a clear T^{-1} component, not only for n-type but also for p-type $Y_xAl_yB_{14}$ (**Fig. 3.12 (a)**) which generally follows TAC for the electrical conductivity as discussed above.

The reason can be elucidated by considering the mixed conduction case in semiconductors. In that case, the total Seebeck coefficient is given by [15]:

$$S = \frac{(S_n\sigma_n + S_p\sigma_p)}{(\sigma_n + \sigma_p)} \quad (3.4)$$

where σ_n and σ_p are the electrical conductivity due to electrons and holes, and S_n and S_p are the Seebeck coefficient for n-type and p-type conduction, respectively.

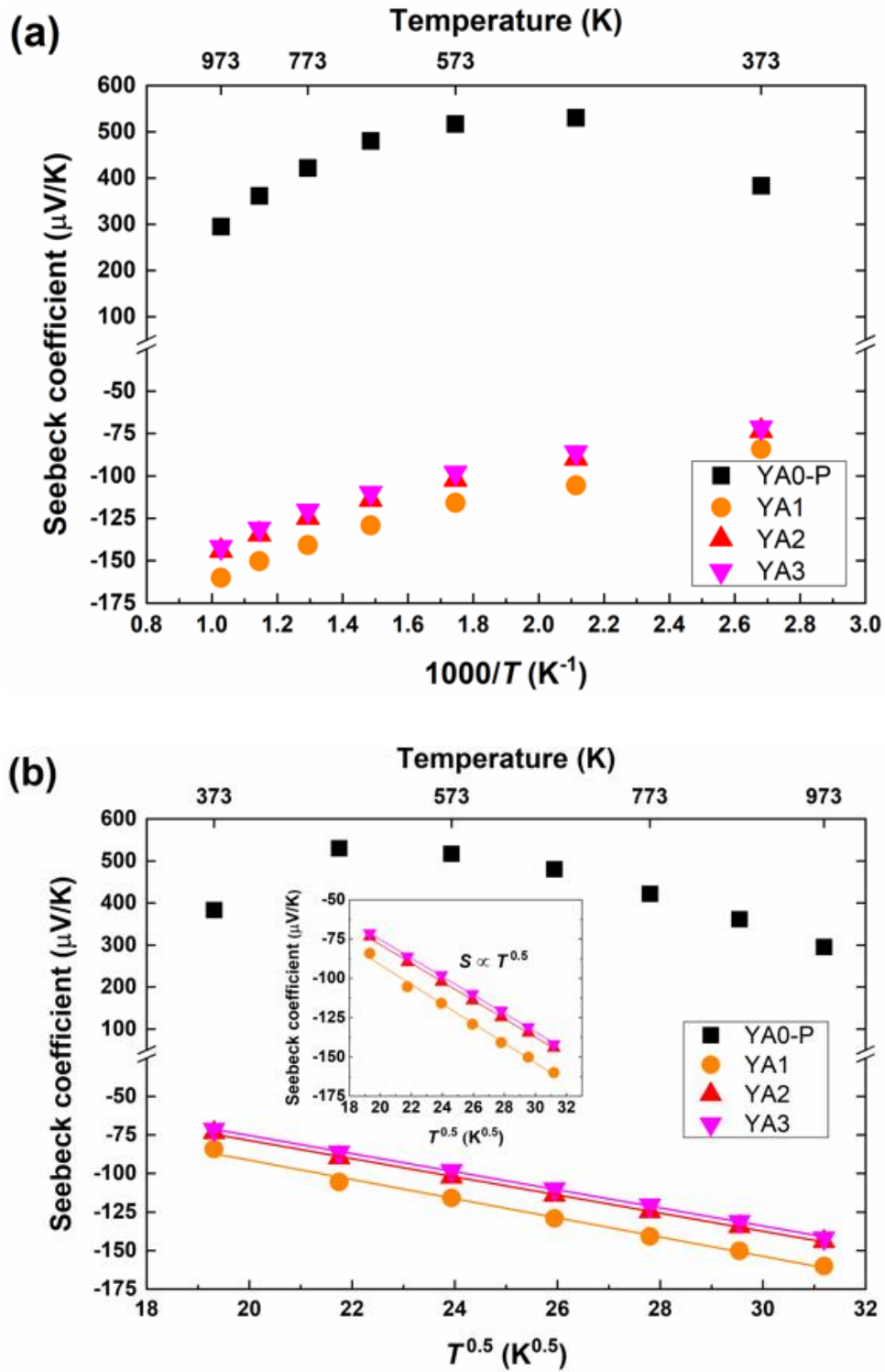


Figure 3.12. Temperature dependence of the Seebeck coefficients of all samples in accordance with (a) TAC mode and (b) VRH mode. The inset shows the Seebeck coefficients of Al-rich samples in accordance with VRH mode. The straight lines for Al-rich samples in VRH mode express the fit to Eq. 3.5 for the temperature range from 373 K to 973 K.

Considering the temperature dependence of electrical conductivity discussed above, namely, the deviation to higher electrical conductivity at higher temperatures, the decrease of Seebeck coefficient of the Al-poor YA0-P above 573 K can therefore be attributed to the increase of thermally excited electrons.

In VRH systems, the temperature dependence of the Seebeck coefficient can be approximated by the following [16]:

$$S \propto (T_0 T)^{\frac{1}{2}} \left(\frac{d \ln N(E)}{dE} \right) \Big|_{E=E_F} \quad (3.5)$$

where $N(E)$ is the density of states at the Fermi level. For Al-rich samples, the temperature dependence of the Seebeck coefficients is almost proportional to $T^{0.5}$, as shown in **Fig. 3.12 (b)**. From this temperature dependence of the Seebeck coefficient it is indicated that the Al-rich samples are VRH systems, since insulating or metallic impurities have less effect on the Seebeck coefficient. The calculated T_0 and $\sigma_{0,VRH}$ values for Al-rich samples are listed in **Table 3.4**.

Table 3.4. T_0 and $\sigma_{0,VRH}$ values of Al-rich samples, which are calculated from the linear fitted lines for $\ln \sigma$ versus $T^{-0.25}$ plots.

Sample name	T_0 (K)	$\sigma_{0,VRH}$ (S/m)
YA1	5.3×10^3	2.4×10^4
YA2	2.6×10^2	3.1×10^4
YA3	2.9	2.5×10^4

To summarize what we have concluded from the data, the conduction mechanism of the Al-poor sample appears to follow TAC dependence, with deviations in the temperature dependences above 573 K indicated from thermally excited electrons. With the large increase of Al inserted atoms, and thereby electrons, for the Al-rich samples, not to mention a speculated effect of excess segregated Al atoms for YA3 in particular, the magnitude of electrical conductivity increases greatly compared to the Al-poor sample. However, despite this, it is indicated that the conduction mechanism follows the VRH mechanism, indicating that the electrical carriers have some localization due to disorder.

3.3.3 Densities and thermal properties

Figure 3.13 shows the densities of the sintered bodies measured by Archimedes' method. All samples prepared by reactive SPS exhibit rather high densities, 2.97-3.07 g/cm³, compared to that of the reference sample (2.43 g/cm³) [4], and are close to the theoretical density of the single crystal Y_{0.62}Al_{0.71}B₁₄, 3.02 g/cm³. The measured densities for Al-rich samples are a little bit higher than the reported theoretical density of single crystal due to the presence of secondary phases. However, even taking into consideration the presence of a relatively small amount of secondary phases, highly dense samples were obtained (**Table 3.5**). This result suggests that the new synthesis process via reactive SPS with AlF₃ is also much more effective for densification of yttrium aluminoboride than the conventional process.

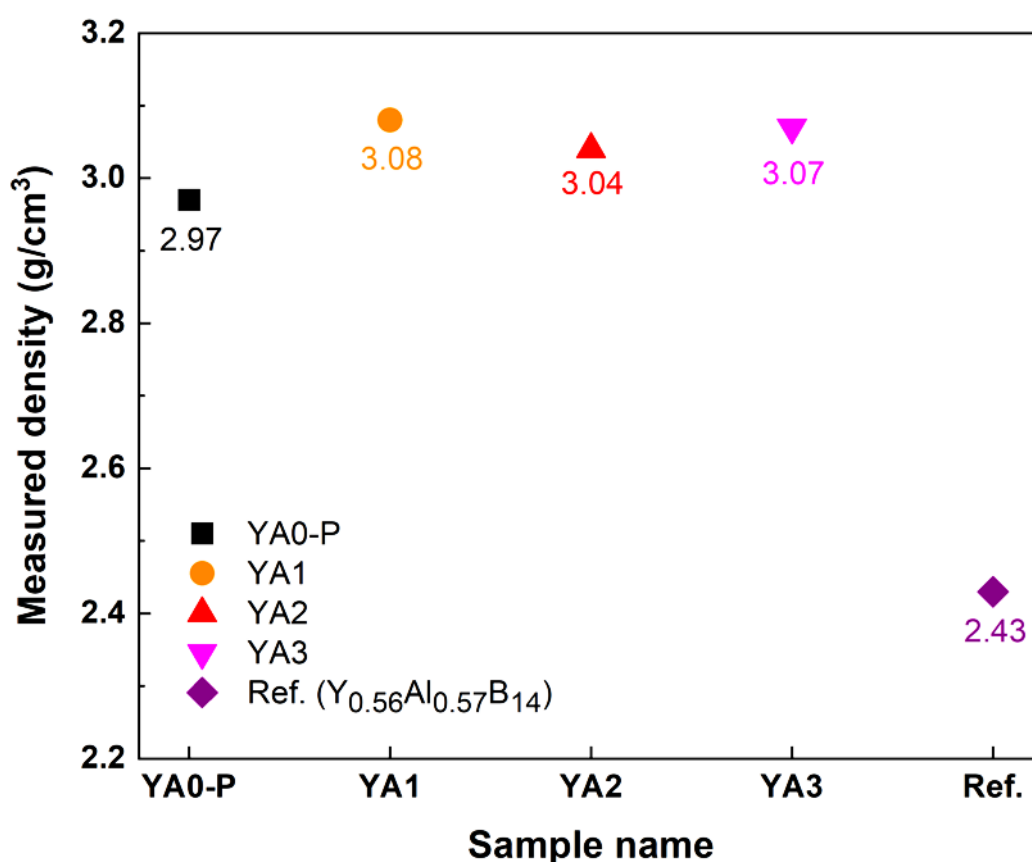


Figure 3.13. Measured densities of as-sintered Y_xAl_yB₁₄ (x~0.64) samples, which are compared with the reported value of Y_{0.56}Al_{0.57}B₁₄ [4]. The theoretical and relative densities of the samples prepared by reactive SPS in present study are given in **Table 3.5**.

Table 3.5. Phase fraction of constituent phases and theoretical and relative density of each sample. Both are estimated by Rietveld refinement.

Sample name	Measured density (g/cm ³)	Theoretical density (g/cm ³)	Relative density (%)
YA0-P	2.97	3.09	96.1
YA1	3.08	3.08	100.0
YA2	3.04	3.08	98.7
YA3	3.07	3.08	99.7

The thermal properties of n-type $Y_xAl_yB_{14}$ samples are shown in **Fig. 3.14** and **3.15**. Thermal conductivities generally decrease with increasing temperature indicating Umklapp scattering (**Fig. 3.14**). YA2 and YA3 show some difference in the temperature dependence, with relatively less temperature dependence compared to YA0-P and YA1.

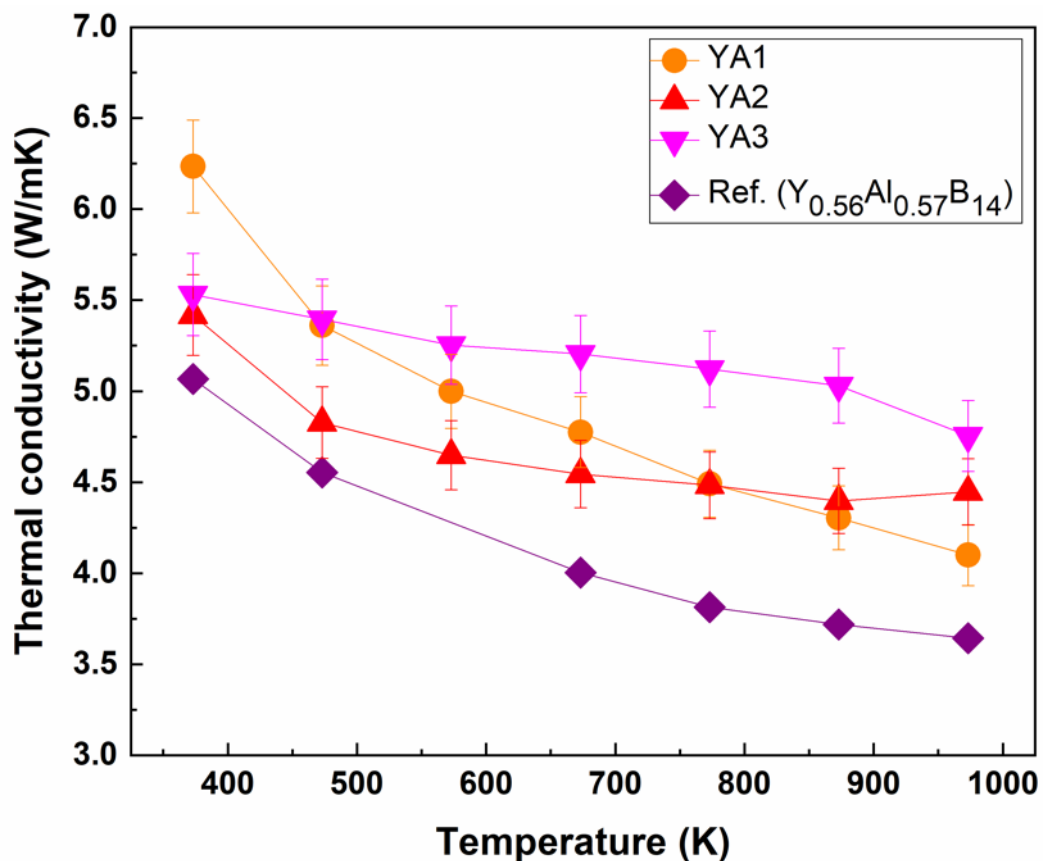


Figure 3.14. Thermal conductivities of n-type $Y_xAl_yB_{14}$ ($x \sim 0.64$) samples prepared by reactive SPS, which are compared with the reported value of $Y_{0.56}Al_{0.57}B_{14}$ [4]. Error bars represent a measurement uncertainty range ($\pm 5\%$).

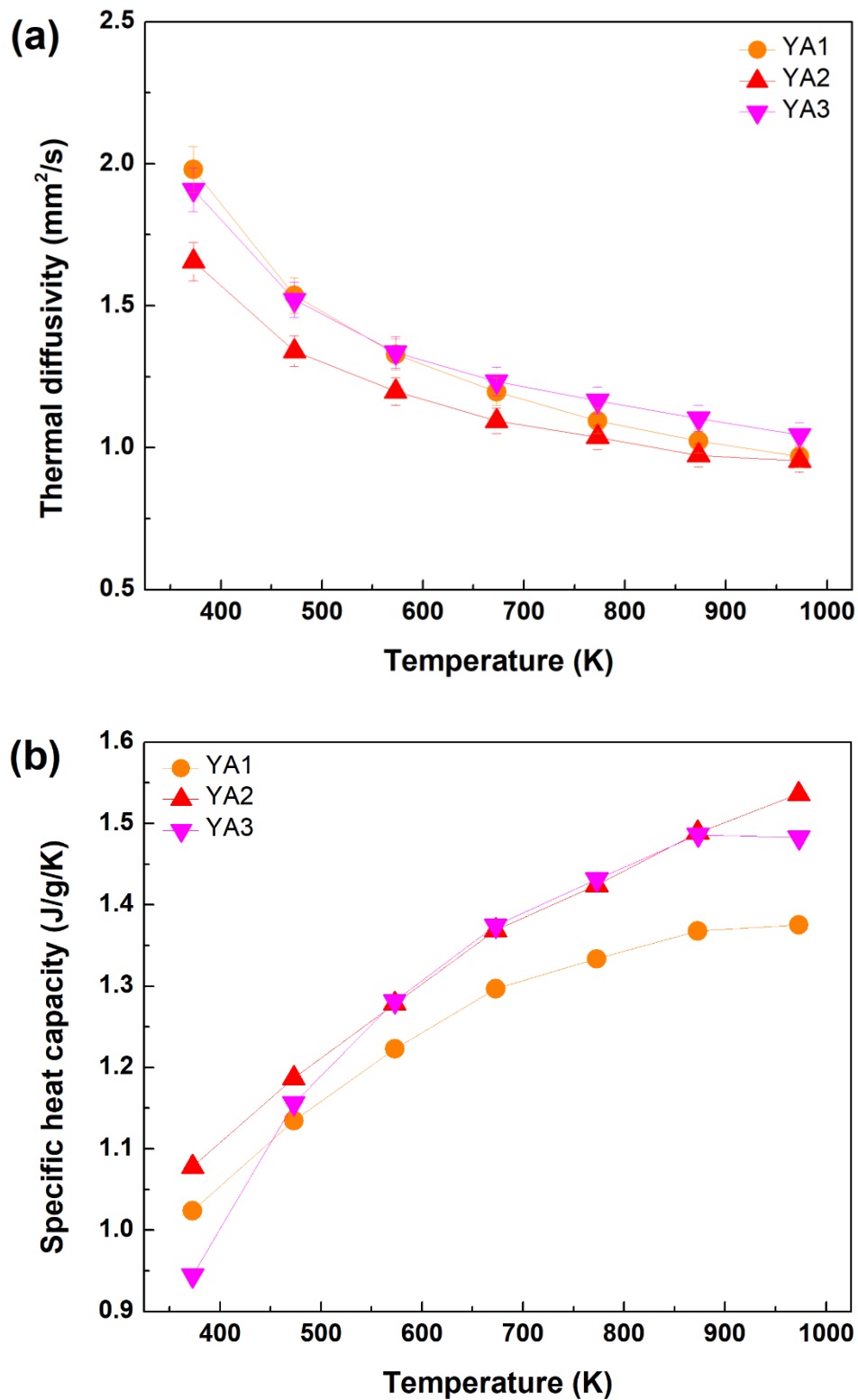


Figure 3.15. (a) Thermal diffusivities and (b) specific heat capacities of n-type $Y_xAl_{1-y}B_{14}$ ($x \sim 0.64$) samples prepared by reactive SPS. Error bars for thermal diffusivities represent a measurement uncertainty range ($\pm 5\%$).

This trend is also reflected to a lesser extent in the intrinsic thermal diffusivities (**Fig. 3.15 (a)**). The behavior may be due to the Al segregation speculated before, since both YA2 and YA3 have higher Al starting compositions, but it is not clear at present. In comparison to reported samples, all samples exhibit slightly higher thermal conductivities due to their relatively higher densities than what has previously been obtained.

3.3.4 Microstructure

To investigate the microstructure, SEM observation for fracture surface of the samples was carried out (**Fig. 3.16**). The samples synthesized by reactive SPS exhibit highly dense microstructure compared to that of previous samples [6] though a minor amount of small pores are observed. All samples show coarse microstructure due to the high sintering temperature and liquid phase introduced during sintering.

The microstructures generally consist of two phases, which are observed as a dark region and a bright region. The components in both regions are revealed by EDX analysis, as shown in **Fig. 3.17**. The result shows the presence of main elements, Y, Al, B and O. The dark region contains Y, Al and B but not O, whereas the bright region contains Al and O but not Y and B. It thus can be considered that the matrix and the secondary phase are $Y_xAl_yB_{14}$ and alumina, respectively. In the matrix phase, some differences in the contrast are observed. It implies an inhomogeneity of the metal atoms which occupy the interstitial sites in $Y_xAl_yB_{14}$.

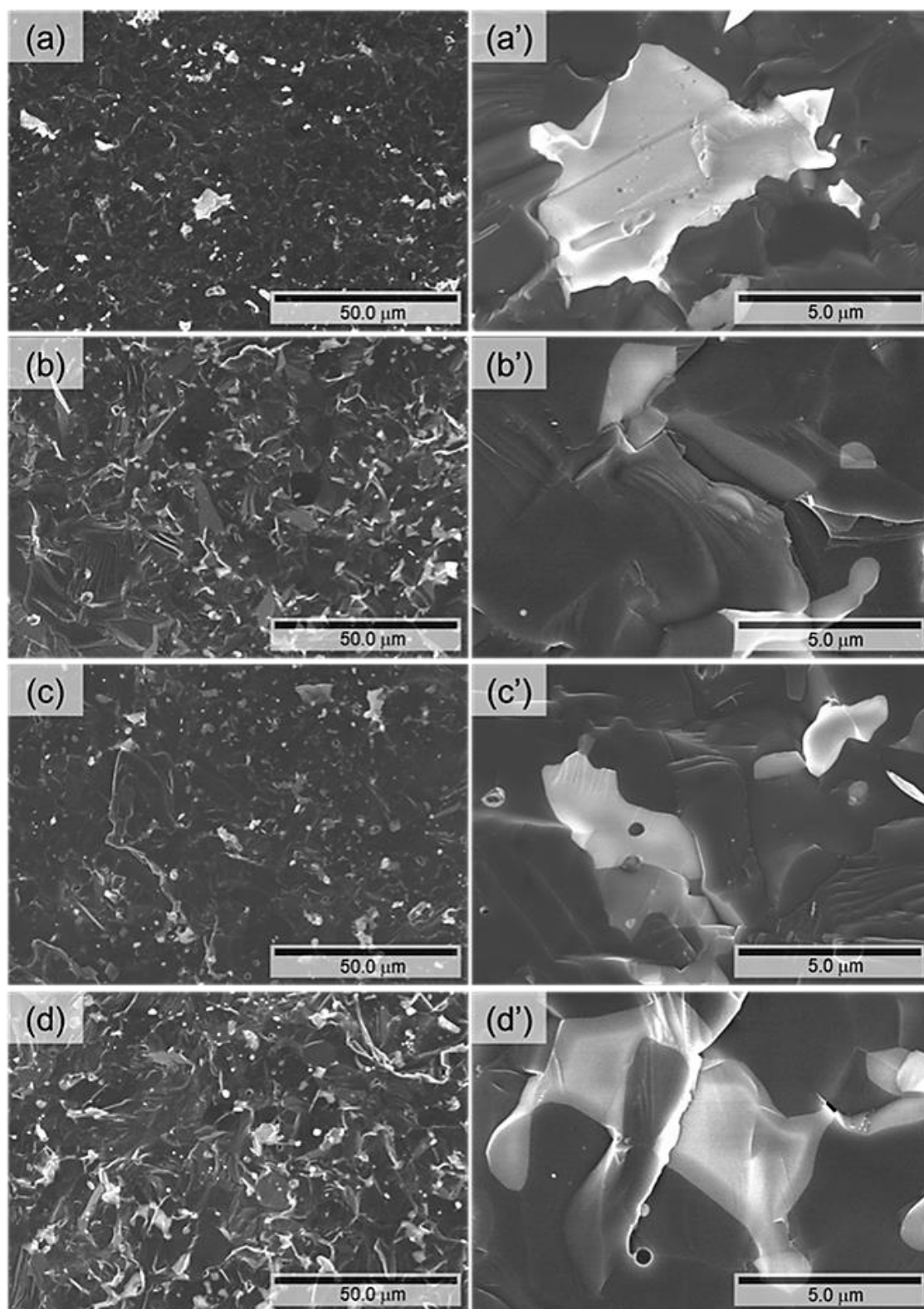


Figure 3.16. SEM images of fracture surface for $Y_xAl_3B_{14}$ samples prepared by reactive SPS, (a, a') YA0-P, (b, b') YA1, (c, c') YA2 and (d, d') YA3.

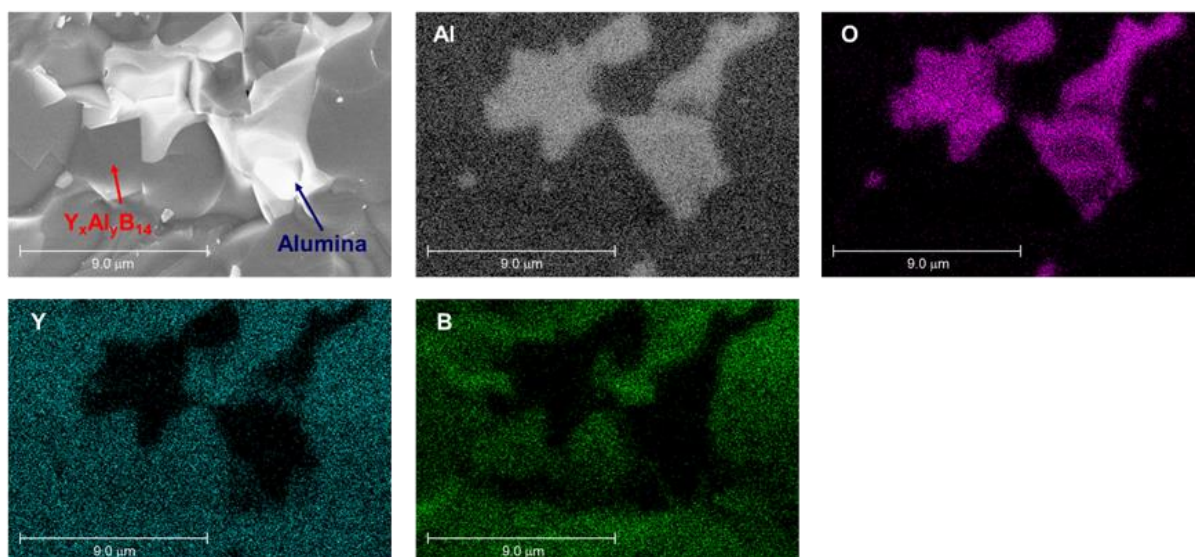


Figure 3.17. The result of EDX analysis on the microstructure in fracture surface of YA1. The distribution of Y, Al, B and O atoms were investigated by the mapping technique.

3.3.5 Thermodynamic calculations

Standard molar enthalpy of formation (ΔH_f^0) and standard molar entropy (S^0) of each material are listed in **Table 3.6** [17]. The calculated free energies of formations (ΔG^0) for AlB_2 , Al_2O_3 and B_2O_3 are listed and plotted in **Table 3.7** and **Fig. 3.18**, respectively.

Table 3.6. Standard molar enthalpies of formation and standard molar entropies at 298 K [17].

Material	ΔH_f^0 (kJ/mol)	S^0 (J/molK)
O_2 (g)	0	205.15
B (s)	0	5.9
Al (s)	0	28.3
Al_2O_3 (s)	-1675.7	50.92
AlB_2 (s)	-151	34.7
B_2O_3 (s)	1273.5	53.97

Table 3.7. Gibbs free energy of formation changes accompanied by each reactions.

Reaction	Gibbs free energy of formation (J/mol)
$\text{Al}(s) + 2\text{B}(s) \rightarrow \text{AlB}_2(s)$	$\Delta G^0 = -151 + 0.0054T$
$2\text{Al}(s) + 3/2\text{O}_2(g) \rightarrow \text{Al}_2\text{O}_3(s)$	$\Delta G^0 = -1675.7 + 0.3134T$
$2\text{B}(s) + 3/2\text{O}_2(g) \rightarrow \text{B}_2\text{O}_3(s)$	$\Delta G^0 = -1273.5 + 0.2420T$

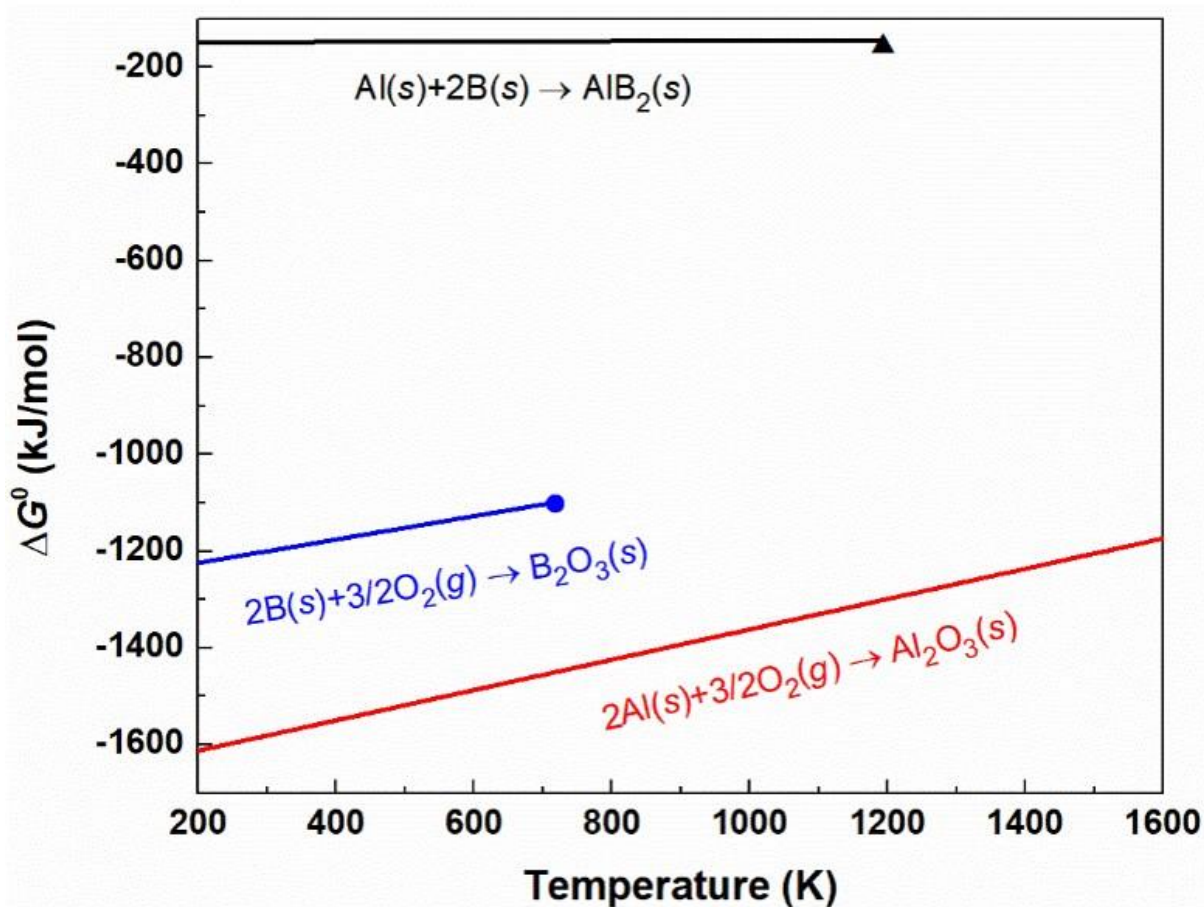


Figure 3.18. Gibbs free energy of formation of AlB_2 , B_2O_3 and Al_2O_3 with temperature range. The point positioned at the end of B_2O_3 line indicates melting temperature of B_2O_3 (723 K), and the triangle positioned at the end of AlB_2 line indicates decomposition temperature (~1193 K) [18].

The results of thermodynamic calculations show that ΔG^0 of α -alumina is much lower than AlB_2 and B_2O_3 . As discussed previously, it is considered that the presence of boron oxide layer coated on the surface of particles of the starting material of amorphous boron reacted with Al during sintering, and thus the alumina phase was formed. We have found that even after removing the boron oxide by the pre-treatment of heating, the amorphous boron powder can have oxidation in air again. To suppress the formation of alumina phase, using a closed system to enable heating of the raw material amorphous boron and then continuously, the mixing process and reactive SPS is desirable.

3.3.6 Power factor and ZT

Figure 3.19 (a), (b) show the power factors and ZT values of $\text{Y}_x\text{Al}_y\text{B}_{14}$ samples with the reference sample [4], respectively. The power factor is dramatically improved by increasing Al occupancy. The maximum power factor, $3.7 \times 10^{-4} \text{ W/mK}^2$, was obtained for YA3 at 973 K, which is significantly higher than that of the reference $\text{Y}_{0.56}\text{Al}_{0.57}\text{B}_{14}$ sample (**Fig. 3.19 (a)**). The large improvement in power factor can be attributed to the high density achieved by the new synthesis process.

The maximum ZT value, 0.08 was also obtained for YA3, as shown in **Fig. 3.19 (b)**. This value is comparable with those reported by previous study, because of the higher thermal conductivity. However, looking forward, it can be said that in general it is more straightforward to find ways to selectively lower the thermal conductivity [19,20], rather than enhance the power factor [21,22], Although the ZT is not high, there are very few materials which potentially can be used for very high temperature thermoelectric applications [2], and we succeeded to prepare $\text{Y}_x\text{Al}_y\text{B}_{14}$ by developing a new sintering process, which is much shorter, simpler and more cost-effective.

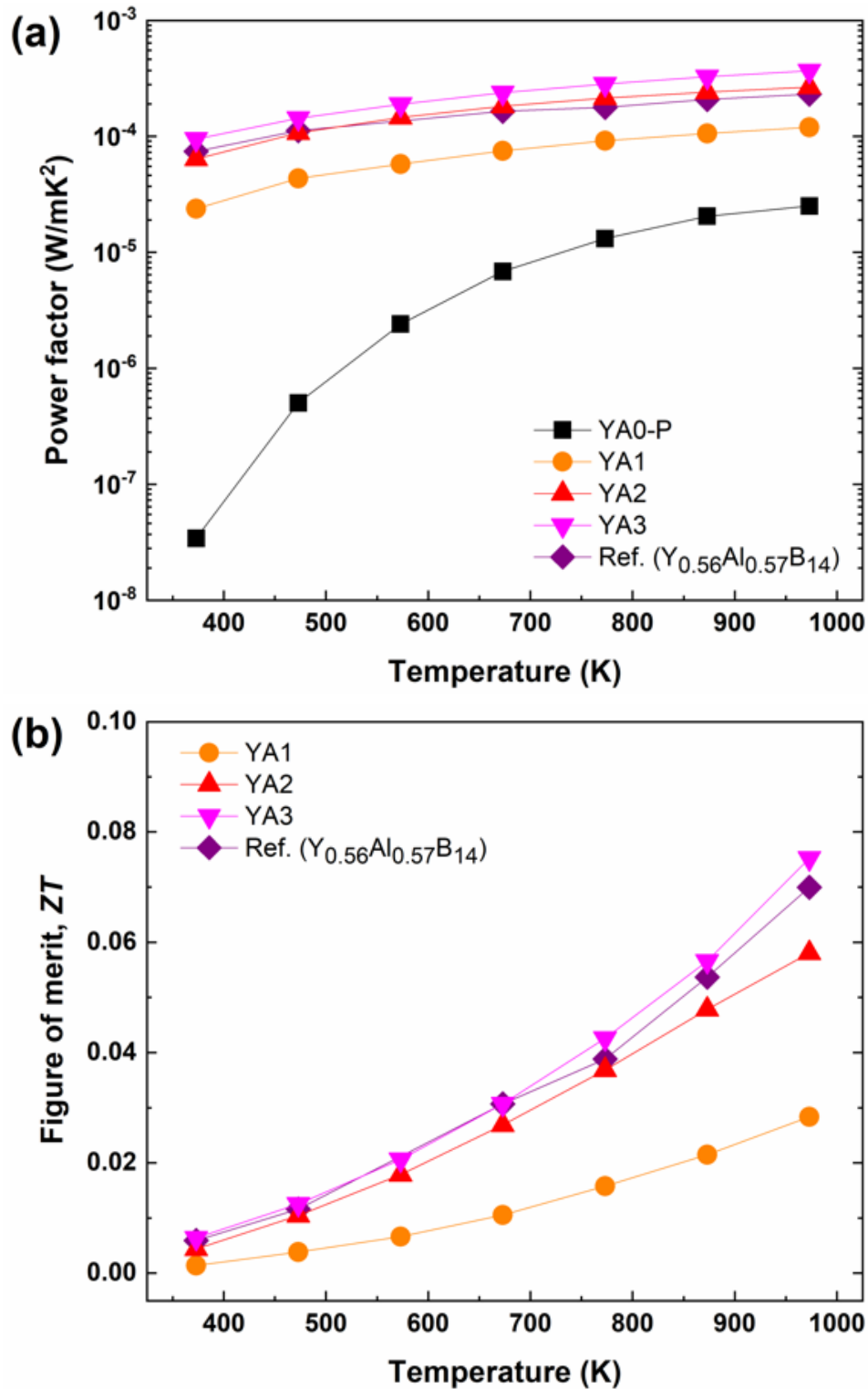


Figure 3.19. (a) Power factor and (b) figure of merits for $Y_xAl_yB_{14}$ ($x \sim 0.64$) samples prepared by reactive SPS, which are compared with the reported value of $Y_{0.56}Al_{0.57}B_{14}$ [4].

3.4 Summary

In this study, a new synthesis process with SPS and sintering additive for synthesis of dense yttrium aluminoboride was developed. The addition of 1 wt.% AlF_3 effectively and dramatically enhanced the sinterability and densification behavior of yttrium aluminoboride by the formation of liquid phase during SPS. Consequently, the process was remarkably simplified and total process time was shortened from ≥ 3 days to only $\sim 4-5$ h.

For p-type $\text{Y}_x\text{Al}_y\text{B}_{14}$, the thermally activated conduction mechanism was proposed rather than the usually assumed variable range hopping (VRH) mechanism, to explain the experimental results of the temperature dependence of electrical conductivity and Seebeck coefficient. Conversely, the VRH mechanism appears to be a good match for the observed properties of the n-type $\text{Y}_x\text{Al}_y\text{B}_{14}$. Because of the increasing Al occupancy and thereby electron carrier content, the n-type samples have much higher conductivity, however, despite this it is indicated that the electrical carriers have some localization due to disorder. ZT values of yttrium aluminoboride prepared by reactive SPS exhibits overall similar thermoelectric properties as the previously reported best samples prepared by conventional processes. The power factor is significantly enhanced because of the high density achieved by the present discovered method. The higher thermal conductivity balances out the ZT , however, in thermoelectric research there are many methods to selectively lower the thermal conductivity. In any case, the present synthesis method that we discovered radically shortens the time necessary for synthesis, e.g. from 8 h to 5 min for the p-type sample. This breakthrough technique is expected to be able to be applied to synthesize other borides also.

3.5 References

- [1] M.M. Korsukova, T. Lundstrom, L.-E. Tergenius, *J. Alloys Compd.*, **187** (1992) 39-48.
- [2] T. Mori, *JOM*, **68** (2016) 2673-2679.
- [3] S. Maruyama, Y. Miyazaki, K. Hayashi, T. Kajitani, T. Mori, *Appl. Phys. Lett.*, **101** (2012) 152101.
- [4] S. Maruyama, A. Prytuliak, Y. Miyazaki, K. Hayashi, T. Kajitani, T. Mori, *J. Appl. Phys.*, **115** (2014) 123702.
- [5] R. Sahara, T. Mori, S. Maruyama, Y. Miyazaki, K. Hayashi, T. Kajitani, *Sci. Technol. Adv. Mater.*, **15** (2014) 035012.
- [6] S. Maruyama, T. Nishimura, Y. Miyazaki, K. Hayashi, T. Kajitani, T. Mori, *Mater. Renew. Sustain Energy.*, **3:31** (2014) 1-6.
- [7] T. Mori, *J. Solid State Chem.*, **275** (2019) 70-82.
- [8] T. Mori, Higher Borides, in: K.A. Gschneidner Jr., J.-C.G. Bünzli, V.K. Pecharsky (Eds.), *Handbook on the Physics and Chemistry of Rare Earths*, Elsevier (2008) 105-173.
- [9] H.-W. Son, B.-N. Kim, T.S. Suzuki, Y. Suzuki, *J. Am. Ceram. Soc.*, **101** (2018) 4430-4433.
- [10] D. Berthebaud, T. Nishimura, T. Mori, *J. Electron. Mater.*, **40** (2011) 682-686.
- [11] T. Mori, T. Nishimura, K. Yamaura, E. Takayama-Muromachi, *J. Appl. Phys.*, **101** (2007) 093714.
- [12] W. Guse, H.X. Saalfelds, *N. Jb. Miner. Mn. H.*, **5** (1990) 217-226.
- [13] C. Boyle, L. Liang, Y. Chen, J. Prucz, E. Cakmak, T.R. Watkins, E. Lara-Curzio, X.Y. Song, *Ceram. Int.*, **43** (2017) 11523-11528.
- [14] N.F. Mott, *J. Non-Cryst. Solids*, **1** (1968) 1-17.
- [15] S.S. Li, *Semiconductor Physical Electronics*, 2th edition, Springer (2006).
- [16] I.P. Zvyagin, *Phys. Status. Solidi. B*, **58** (1973) 443-449.
- [17] J.D. Cox, D.D. Wagman, V.A. Medvedev, *CODATA key values for thermodynamics*, Hemisphere Pub. Corp. (1989).
- [18] D.R. Lide, *CRC Handbook of Chemistry and Physics*, 84th edition, CRC Press (2003).

- [19] A.U. Khan, K. Kobayashi, D.-M. Tang, Y. Yamauchi, K. Hasegawa, M. Mitome, Y. Xue, B. Jiang, K. Tsuchiya, D. Golberg, Y. Bando, T. Mori, *Nano Energy*, **31** (2017) 152-159.
- [20] F. Ahmed, N. Tsujii, T. Mori, *J. Materiomics*, **4** (2018) 221-227.
- [21] B. Hinterleitner, I. Knapp, M. Poneder, Y. Shi, H. Müller, G. Eguchi, C. Eisenmenger-Sittner, M. Stöger-Pollach, Y. Kakefuda, N. Kawamoto, Q. Guo, T. Baba, T. Mori, S. Ullah, X.-Q. Chen, E. Bauer, *Nature*, **576** (2019) 85-90.
- [22] F. Ahmed, N. Tsujii, T. Mori, *J. Mater. Chem. A*, **5** (2017) 7545-7554.

Chapter 4

Rapid synthesis of thermoelectric $\text{YB}_{22}\text{C}_2\text{N}$ via spark plasma sintering with gas/solid reaction technology

4.1 Introduction

The rare earth borides are a rich class of materials exhibiting interesting structural and physical properties such as superconductivity, magnetism, and thermoelectricity, for example [1-9]. The homologous series of rare earth borocarbonitrides; $\text{RB}_{15.5}\text{CN}$, $\text{RB}_{22}\text{C}_2\text{N}$, $\text{RB}_{28.5}\text{C}_4$ were found to exhibit unexpectedly strong magnetic coupling for dilute magnetic insulators [10,11], and interesting two-dimensional (2D) spin glass-like behavior [12,14]. This series of compounds were also found to be the long-awaited thermoelectric n-type counterpart to boron carbide [15,17].

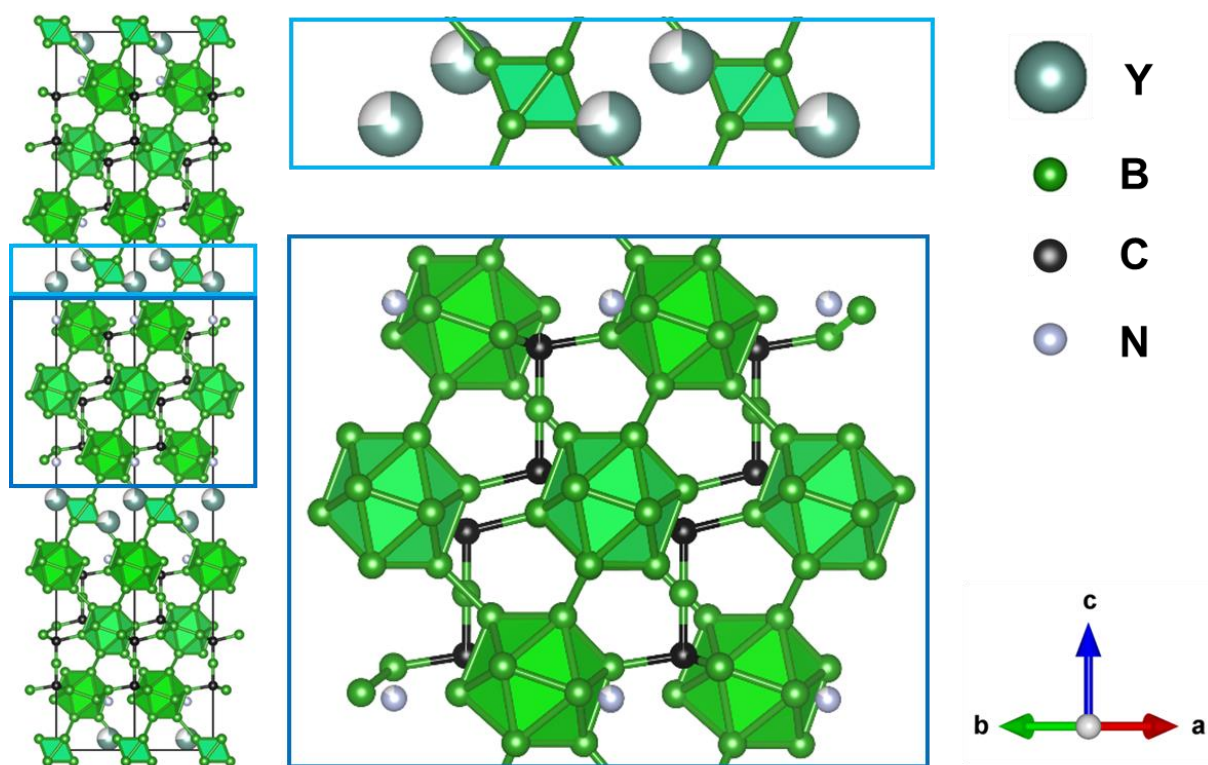


Figure 4.1. The crystal structure of $\text{YB}_{22}\text{C}_2\text{N}$, which is hexagonal structure belonging to $R-3m$ space group [10].

Despite the attractive properties, the synthesis of these compounds has always been noted to be difficult, necessitating a complex and time consuming process (≥ 9 steps; ≥ 4 days) involving long-time sintering (≥ 10 h), typically multiple re-sintering, crushing and washing processes [10,18-20]. Densification of the material was also found to be difficult, with initial spark plasma sintering (SPS) experiments only yielding a maximum $\sim 75\%$ density [16]. Several sintering aids were found to lead to highly densified samples, but these additives were found to be detrimental to the thermoelectric properties [19,20].

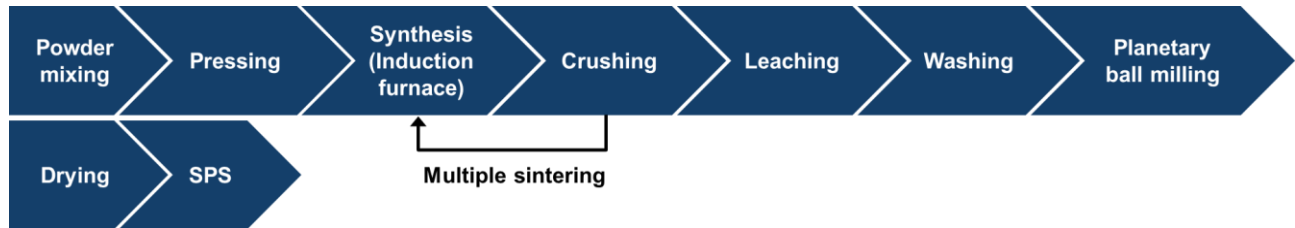


Figure 4.2. Flow chart of conventional synthesis process for bulk $\text{YB}_{22}\text{C}_2\text{N}$. It consists of more than 9 steps, and the total process time is ≥ 4 days.

In this study, we report on the first attempt of direct synthesis of complex borocarbonitrides through reactive SPS with gas/solid reaction. A new synthesis method for $\text{YB}_{22}\text{C}_2\text{N}$ from raw materials (except N) was developed to shorten the synthesis time and to attain dense samples. In order to introduce nitrogen into the mixture and to help the formation of the objective phase, gas/solid reaction technology was used during the heating process. Such in situ nitridation during SPS has already been reported for titanium alloy-based composites [21], but to our knowledge, this is the first example of direct nitride synthesis of borocarbonitrides through reactive SPS.

4.2 Experimental procedure

4.2.1 Synthesis

Commercially available YB_4 (99.9%, Japan New Metals Co., Ltd.), amorphous B (99%, New Metals and Chemicals Co., Ltd.) and graphite (Sigma-Aldrich Co., Ltd.) powders were used as the starting materials. The powders were simply mixed under ethanol using an agate mortar with the initial nominal composition; $Y_{0.73}B_{22}C_2$, which corresponds to the average refined composition in the previous reports [10,18]. After drying, the powder mixtures were reactively sintered using an SPS machine (Dr. Sinter, Fuji Denpa Koki Co., Ltd.), as shown in **Fig. 4.3**.

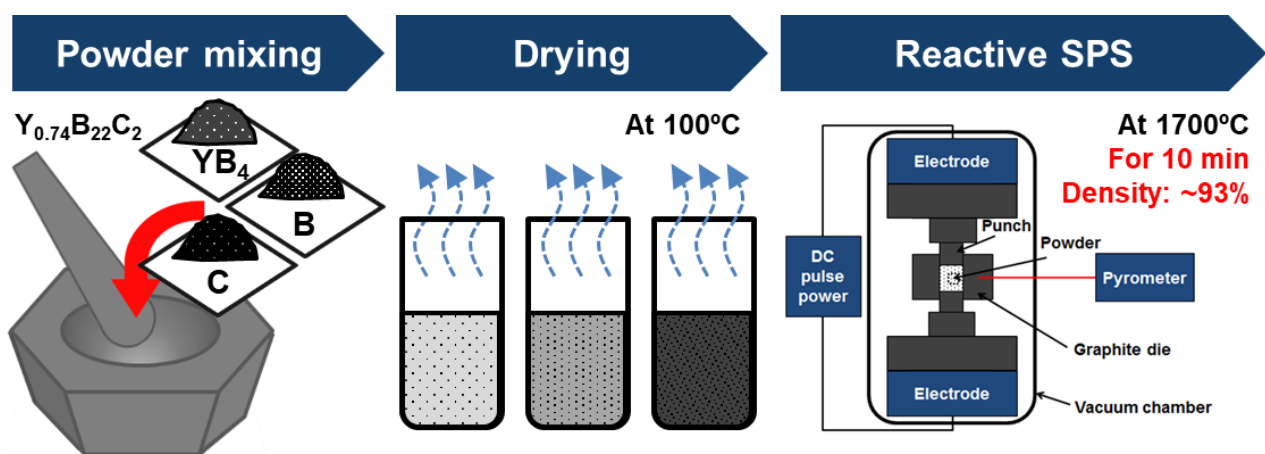


Figure 4.3. Flow chart of newly developed synthesis process for bulk $YB_{22}C_2N$ in this study.

For sintering, the mixtures were poured into a 10 mm diameter graphite die and pressed using graphite punches. A graphite paper was used as a release agent for ejecting the sample from the graphite die after sintering, and no BN was used. The sintering was carried out in a two-step process at the temperatures of T1 and T2 (**Fig. 4.4**). The mixtures were heated up to T1 of $1100\text{--}1300^\circ\text{C}$ in vacuum to remove volatile gases and B_2O_3 from surface oxidation of amorphous B, and then kept for 0-60 min in reduced N_2 gas atmosphere (-0.03 MPa) to introduce nitrogen into the mixtures. After that, they were heated up to T2 of $1650\text{--}1750^\circ\text{C}$, and then kept for 0-10 min under a uniaxial pressure of ~ 30 MPa.

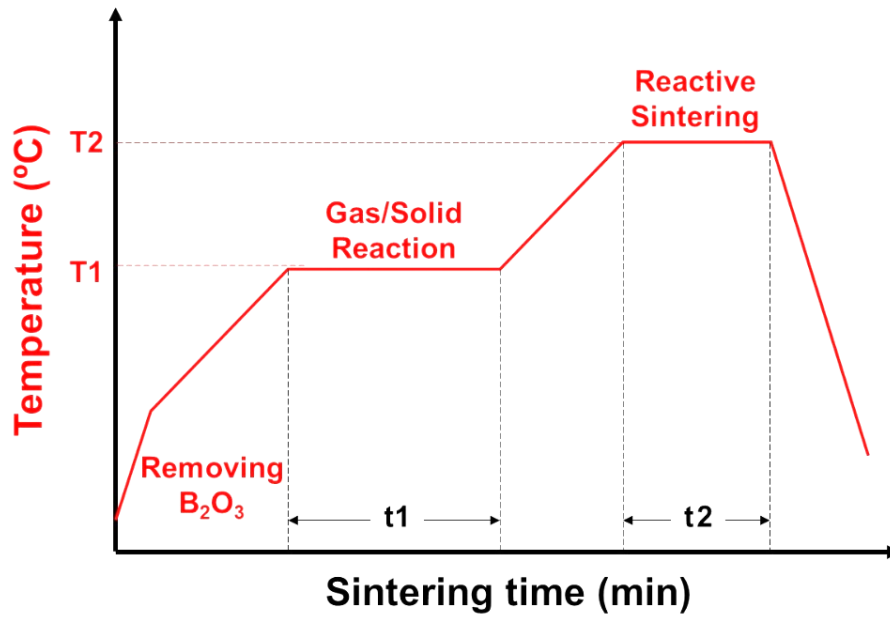


Figure 4.4. The sintering schedule for synthesis of YB₂₂C₂N by reactive SPS.

4.2.2 Characterizations

The constituent phases of the sintered samples were analyzed by X-ray diffraction (XRD, Smart lab 3, Rigaku) with Cu K α radiation. The lattice parameters and the ratio of phases of the sintered samples were estimated by FullProf and PowderCell software, respectively. The electrical resistivities and Seebeck coefficients were evaluated in the temperature range of 373-573 K using the standard 4-probe measurement setup of the ZEM-2 instrument (ADVANCE RIKO, Inc.).

4.3 Results and discussion

4.3.1 Development of N_2 gas/solid reaction step

Figure 4.5 shows the XRD patterns of the samples prepared at 1700°C for 10 min by reactive SPS with different nitrogen treatment temperature (T1). The SPS1, SPS2 and SPS3 samples were kept at 1100 , 1200 and 1300°C for 30 min in N_2 gas atmosphere during heating, respectively. The $YB_{22}C_2N$ phase was successfully synthesized when the samples were kept at 1200 or 1300°C although they contained some amount of secondary phases including YB_6 and B_4C . The result implies that the N_2 gas/solid reaction is activated above 1200°C .

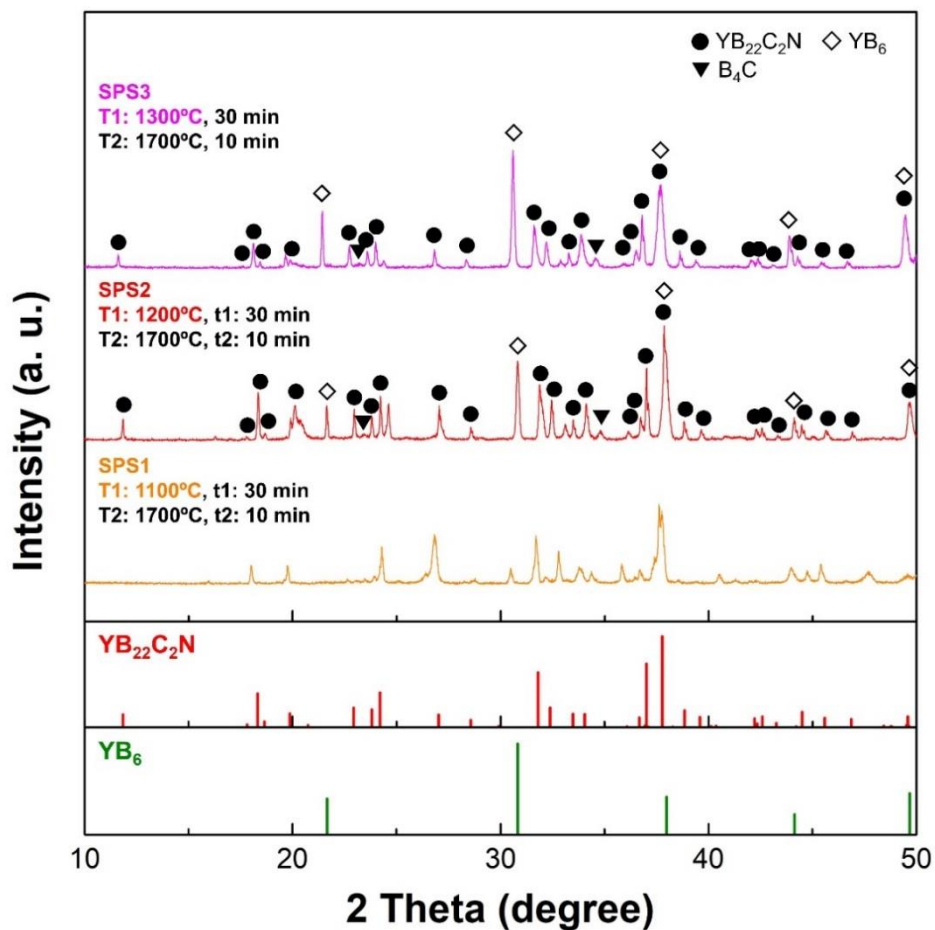


Figure 4.5. The XRD patterns of the SPS1, SPS2 and SPS3 samples prepared with different nitrogen treatment temperature (T1) by reactive SPS.

The XRD pattern of the SPS3 sample showed a higher amount of YB_6 than the SPS2 sample. The transition from amorphous boron to crystalline α -rhombohedral boron occurs above 1300°C [22]. It is thus considered that the reactivity among the YB_4 precursor, carbon and boron decreased when the mixture was kept at 1300°C due to the transition of amorphous boron to crystalline boron, and hence less $YB_{22}C_2N$ was formed. Furthermore, the reaction rate is closely related to the surface area. Therefore, the decrease of reactivity is also attributed to a decrease of the surface area of particles due to particle growth with increasing T1. Meanwhile, the formation of B_4C is attributed to not only the relatively low boron/carbon ratio originated from boron loss by evaporation of B_2O_3 occurred below T1 [10], but also carbon diffusion activated at high temperature during SPS due to its carbon-rich atmosphere.

Figure 4.6 shows the XRD patterns of the samples prepared at 1700°C for 10 min by reactive SPS with different nitrogen treatment time (t_1). In order to investigate the effect of the time on the gas/solid reaction, the SPS4, SPS5, SPS2 and SPS6 samples were kept at T1 for 0, 10, 30 and 60 min (t_1) in N_2 gas atmosphere during heating, respectively. Herein, 1200°C was selected for T1 with considering the aforementioned results.

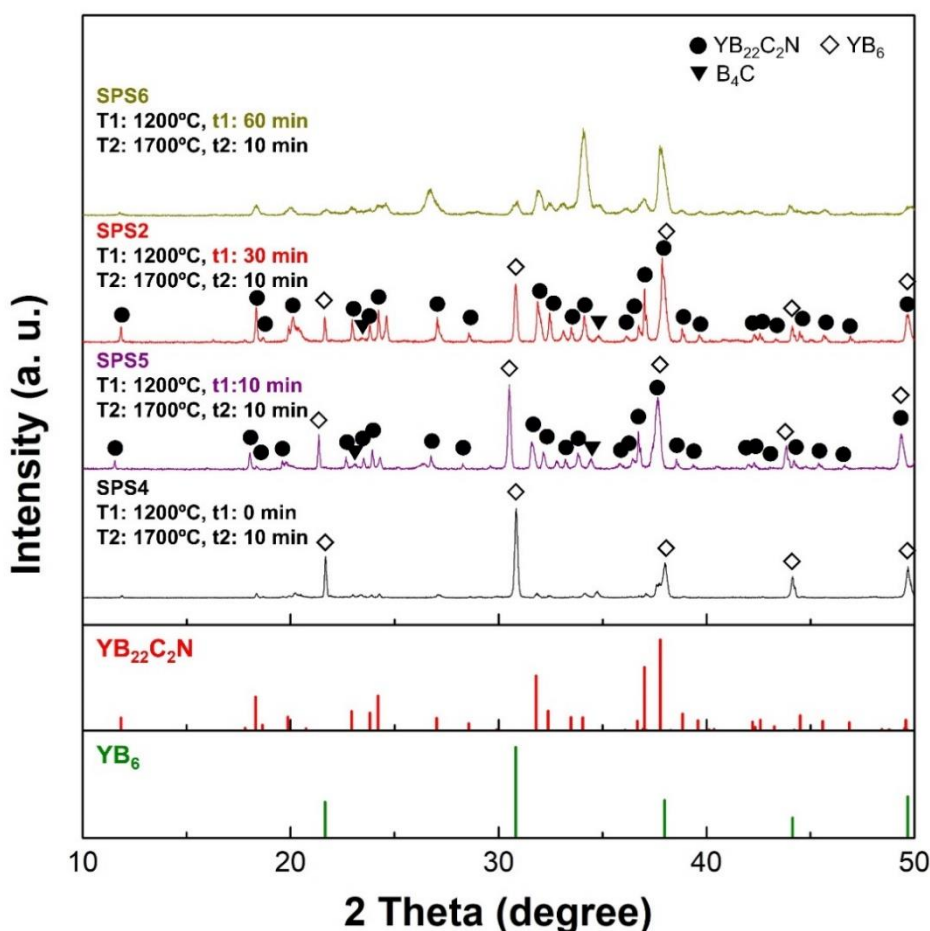


Figure 4.6. The XRD patterns of the SPS4, SPS5, SPS2 and SPS6 samples prepared with different nitrogen treatment time (t_1) by reactive SPS.

When the mixture was heated up to the sintering temperature without holding at T1, the XRD pattern of the sample (SPS4) mainly exhibited strong peaks of YB_6 with very weak peaks of $YB_{22}C_2N$. The ratio of peaks of $YB_{22}C_2N$ to YB_6 increased with increasing dwell time up to 30 min (SPS5 and SPS2). The results indicate that the gas/solid reaction step is beneficial for the synthesis of $YB_{22}C_2N$. Meanwhile, a dwell time exceeding 60 min (SPS6) at the gas/solid reaction step does not benefit for the synthesis of $YB_{22}C_2N$. Since the axial displacement of SPS6 sample continuously changed during the gas/solid reaction step for 60 min although the nitrogen treatment was carried out at the isothermal temperature (**Fig. 4.7**), it is assumed that the deterioration is attributed to a reaction (or reactions) accompanying a volume change between amorphous boron and introduced nitrogen, which could be activated by long-time treatment. Therefore, 30 min was selected as t1 for the N_2 gas/solid reaction step.

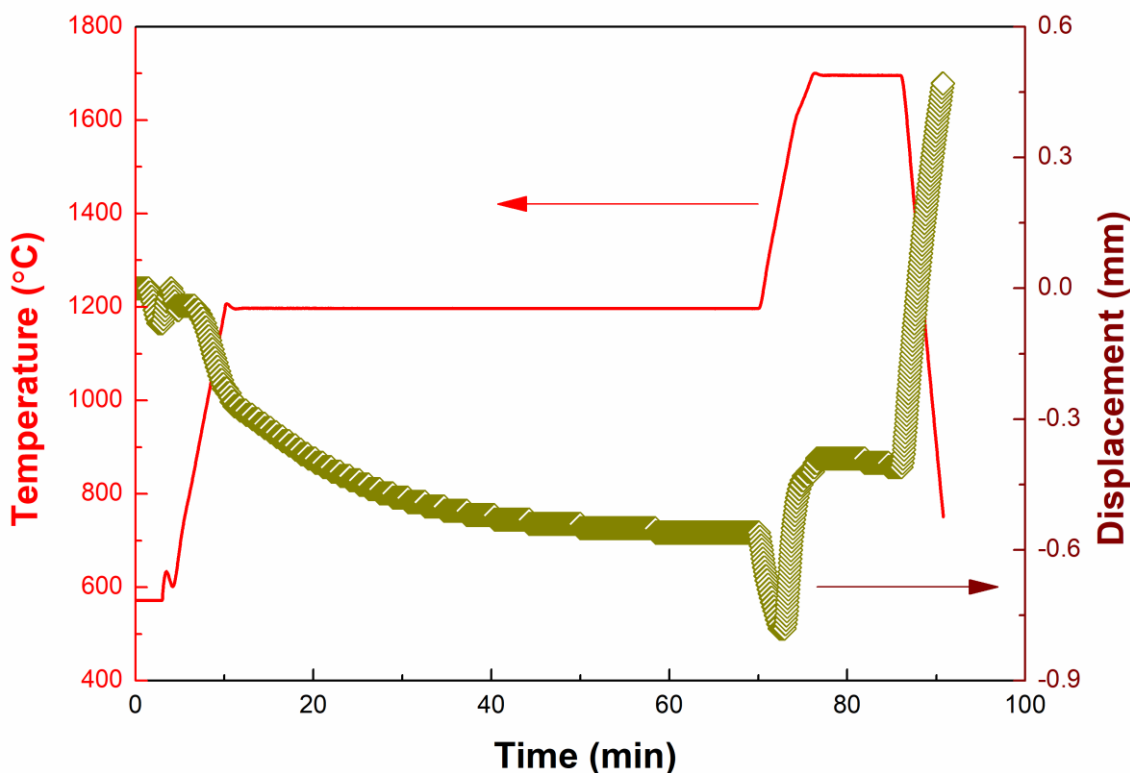


Figure 4.7. Displacement change of the SPS6 sample during reactive SPS. The SPS6 sample was reactively sintered at 1700°C for 10 min after gas/solid reaction step carried out at 1200°C for 60 min. The decrease and increase of displacement change indicate expansion and shrinkage, respectively.

The estimated lattice parameters and measured densities of the SPS2 and SPS5 samples are given in the **Table 4.1**. The lattice parameters are well matched to those of the samples prepared at 1700°C under 30 MPa by SPS in the previous study [19]. The measured densities of the samples consolidated by reactive SPS were also comparable to those of the samples prepared by conventional process with sintering additives, YB₄, YB₂₅(C), Si, SiC, Al and TiC [19,20], even though no sintering additive available for densification was used. Since additives can often be detrimental to thermoelectric properties [19,20], it indicates that reactive SPS has some advantages to densification of the bulk samples compared to the conventional process. However, since the present process involves volume changes attributed to several continuous reactions among starting materials, various shrinkage rates of multiple constituent phases and thermal expansion of graphite spacers, it is difficult to discuss on the densification behavior clearly. To investigate the reaction steps and densification behavior occurred during reactive SPS with gas/solid reaction technology, further study is required.

Table 4.1. Lattice parameters and measured densities of the SPS2 and SPS5 samples prepared by reactive SPS.

Sample name	a (Å)	c (Å)	Density (g/cm ³)
*YB ₂₂ C ₂ N	5.6230	44.7853	2.97
SPS2	5.6068	44.7506	2.55
SPS5	5.6012	44.7722	2.79
**Reference	5.6066	44.7678	2.84

4.3.2 Development of reactive sintering process

Next, the effect of the sintering temperature T₂ on the reactive SPS for the synthesis of YB₂₂C₂N was investigated. The SPS7, SPS2 and SPS8 samples were kept at 1200°C for 30 min in N₂ gas atmosphere before sub-subsequent heating, and then sintered at 1650, 1700 and 1750°C for 10 min, respectively. All samples exhibited peaks of YB₂₂C₂N, as shown in **Fig. 4.8**. However, the YB₂₂C₂N phase was decomposed when it was sintered above 1750°C. Considering the densification during SPS, 1700°C was selected as the temperature for the reactive sintering.

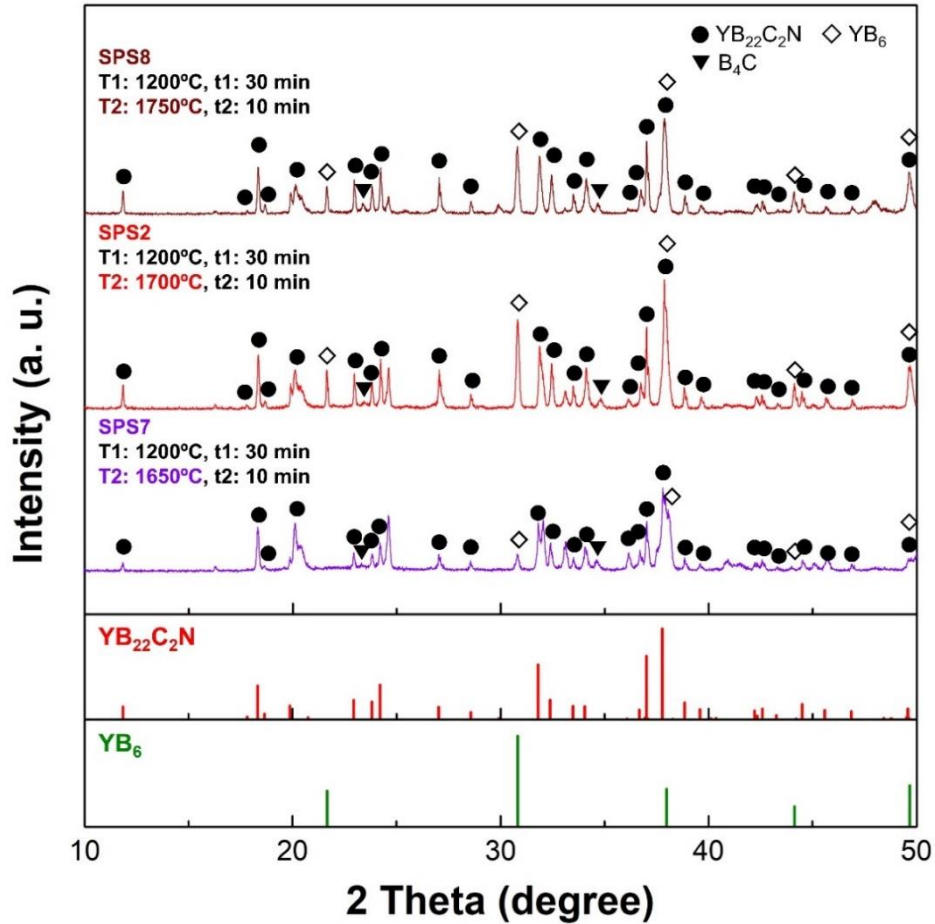


Figure 4.8. The XRD patterns of the SPS7, SPS2 and SPS8 samples prepared with different sintering temperature (T2) by reactive SPS.

To determine the optimal sintering time t_2 for the reactive SPS process, XRD measurements were carried out for the SPS9, SPS10 and SPS2 samples after sintering at 1700°C for 0, 5 and 10 min, respectively (**Fig. 4.9**). For the SPS9 sample, which was heated up to 1700°C and cooled down immediately without holding after the gas/solid reaction step, no peaks of $\text{YB}_{22}\text{C}_2\text{N}$ were identified. It implies that the gas/solid reaction step only helps introduce nitrogen into the mixture, and $\text{YB}_{22}\text{C}_2\text{N}$ is not synthesized during that step. The formation of the $\text{YB}_{22}\text{C}_2\text{N}$ phase started when the sample was kept at 1700°C for 5 min. The amount of the $\text{YB}_{22}\text{C}_2\text{N}$ phase increased when it was kept at 1700°C for 10 min. Therefore, 10 min was selected as t_2 , which is the dwell time for the preparation of $\text{YB}_{22}\text{C}_2\text{N}$ by reactive SPS. Consequently, the SPS condition for the SPS2 sample was determined as the optimal condition for the synthesis of $\text{YB}_{22}\text{C}_2\text{N}$ via reactive SPS with gas/solid reaction in this study.

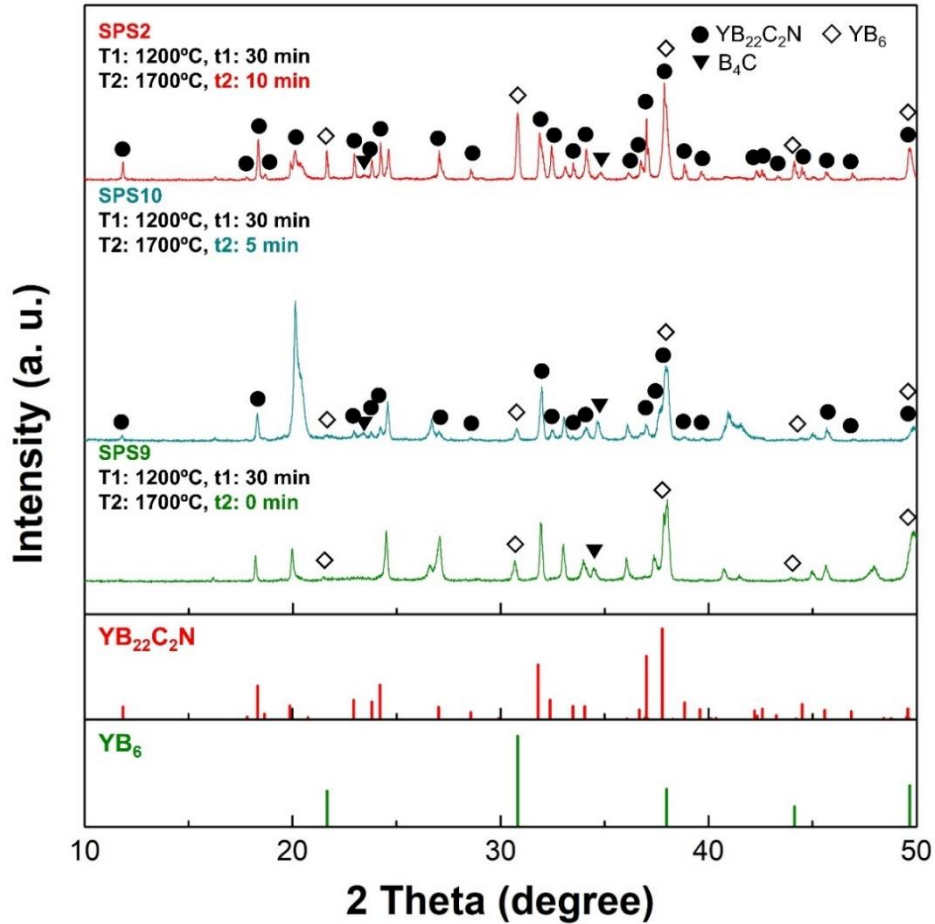


Figure 4.9. The XRD patterns of the SPS9, SPS10 and SPS2 samples prepared with different sintering time (t_2) by reactive SPS.

4.3.3 Phase ratio and thermoelectric properties

Figure 4.10 (a) shows the ratio of $\text{YB}_{22}\text{C}_2\text{N}$, B_4C and YB_6 phases in the SPS2 and SPS5 samples. The result of quantitative analysis with approximation only considering these 3 phases seems to indicate that the SPS2 sample contains more amount of $\text{YB}_{22}\text{C}_2\text{N}$ and less amounts of secondary phases compared to the SPS5 sample. The temperature dependence of the thermoelectric properties of the SPS2 and SPS5 samples are plotted in **Fig. 4.10 (b)**, **(c)** and **(d)**. As shown in **Fig. 4.10 (b)**, both samples exhibit semiconducting behavior in their electrical conductivities, which increase with increasing temperature. The SPS2 sample exhibited lower electrical conductivity values in all measured temperature range compared to those of the SPS5 sample. The lower electrical conductivity is attributed to less amount of electrically conductive secondary phases, B_4C and YB_6 , and its lower density.

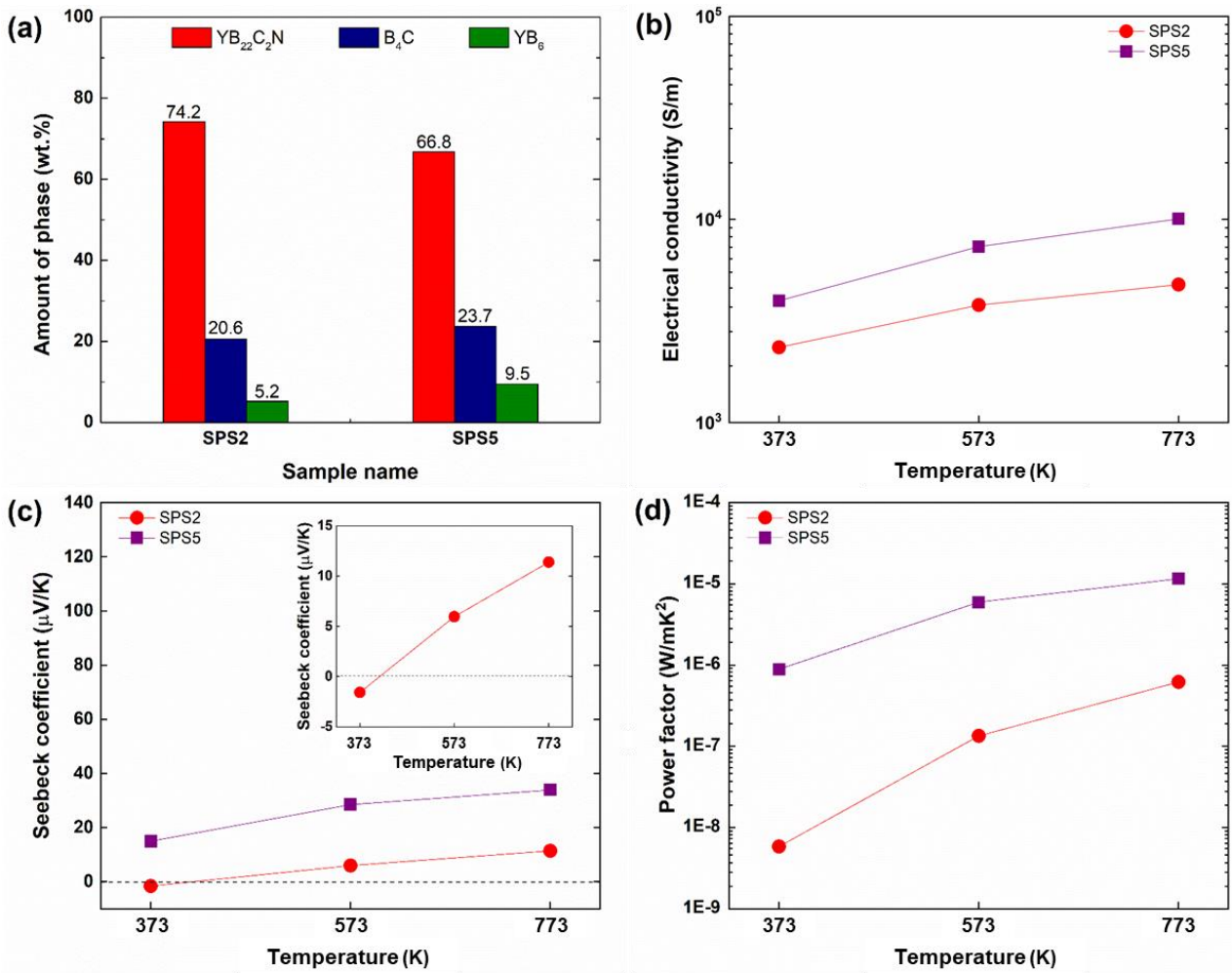


Figure 4.10. (a) The amount of YB₂₂C₂N, B₄C and YB₆ phases, (b) the electrical conductivities, (c) Seebeck coefficients and (d) the power factors of the SPS2 and SPS5 samples.

The measured Seebeck coefficient values are shown in **Fig. 4.10 (c)**. At 100°C, the SPS5 sample exhibited a positive value, whereas the SPS2 sample exhibited a negative value. The SPS2 sample shows a general shift toward n-type behavior over the whole temperature region. It indicates that the thermoelectric behavior of the sintered sample is changed from p-type to n-type with increasing amount of YB₂₂C₂N, which is known as an n-type material [15,16,18]. The Seebeck coefficient of SPS2 sample was changed from negative to positive value between 100 and 300°C, and then increased with increasing temperature. It is considered that the increase of positive Seebeck coefficients with the temperature are attributed to the presence of B₄C [9,17,23]. Small amounts of B₄C secondary phase have been previously shown to shift this type of material from n-type behavior to p-type behavior [15,17].

Figure 4.10 (d) shows the temperature dependence of power factors of each sample. The amount of B_4C could be reduced by controlling boron/carbon ratios in the synthesis [10]. Through developing an initial composition containing the optimal boron/carbon ratio and reducing the effect of carbon-rich atmosphere with using BN as the release agent instead of the graphite paper, improvements of the absolute value of the negative Seebeck coefficient and power factor are expected.

4.4 Summary

In this study, a new synthesis route for preparation of polycrystalline $\text{YB}_{22}\text{C}_2\text{N}$ by reactive SPS was developed. N_2 gas/solid reaction technology carried out at 1200°C for 30 min during SPS effectively helped the formation of the objective phase. The most homogeneous $\text{YB}_{22}\text{C}_2\text{N}$ was synthesized when it was sintered at 1700°C for 10 min after the gas/solid reaction step, and it exhibited n-type thermoelectric behavior at low temperature. Consequently, by developing the present synthesis method, the total process steps and the whole process time required to synthesize $\text{YB}_{22}\text{C}_2\text{N}$ were dramatically shortened from ≥ 9 to only 3 steps, and from ≥ 4 days to only ~ 3 hours, respectively. This new method is expected to open the door for more effective synthesis of complex borocarbonitrides.

4.5 References

- [1] B.T. Matthias, T.H. Geballe, K. Andres, E. Corenzwit, G.W. Hull, J.P. Maita, *Science*, **159** (1968) 530.
- [2] K.H.J. Buschow, Boron and Refractory Borides, in: V.I. Matkovich, G.V. Samsonov, P. Hagenmuller, T. Lundstrøm (Eds.), Springer (1977) 494-515.
- [3] J. Etourneau, P. Hagenmuller, *Philos. Mag. B*, **52** (1985) 589-610.
- [4] R.J. Cava, H. Takagi, H.W. Zandbergen, J.J. Krajewski, W.F. Peck Jr, T. Siegrist, B. Batlogg, R.B. Van Dover, R.J. Felder, K. Mizuhashi, J.O. Lee, H. Eisaki, S. Uchida, *Nature*, **367** (1994) 252-253.
- [5] T. Mori, Handbook on the Physics and Chemistry of Rare Earths, in: K.A. Gschneidner Jr., J.-C.G. Bünzli, V.K. Pecharsky (Eds.), Elsevier (2008) 105-173.
- [6] D.J. Kim, J. Xia, Z. Fisk, *Nat. Mater.*, **13** (2014) 466-470.
- [7] A. Koitzsch, N. Heming, M. Knupfer, B. Büchner, P.Y. Portnichenko, A.V. Dukhnenko, N.Y. Shitsevalova, V.B. Filipov, L.L. Lev, V.N. Strocov, J. Ollivier, D.S. Inosov, *Nat. Commun.*, **7** (2016) 10876.
- [8] N.E. Sluchanko, A.N. Azarevich, M.A. Anisimov, A.V. Bogach, S.Y. Gavrilkin, M.I. Gilmanov, V.V. Glushkov, S.V. Demishev, A.L. Khoroshilov, A.V. Dukhnenko, K.V. Mitsen, N.Y. Shitsevalova, V.B. Filippov, V.V. Voronov, K. Flachbart, *Phys. Rev. B*, **93** (2016) 085130.
- [9] T. Mori, *J. Solid State Chem.*, **275** (2019) 70-82.
- [10] F. Zhang, A. Leithe-Jasper, J. Xu, T. Mori, Y. Matsui, T. Tanaka, S. Okada, *J. Solid State Chem.*, **159** (2001) 174-180.
- [11] F. Zhang, F. Xu, A. Leithe-Jasper, T. Mori, T. Tanaka, J. Xu, A. Sato, Y. Bando, Y. Matsui, *Inorg. Chem.*, **40** (2001) 6948-6951.
- [12] T. Mori, A. Leithe-Jasper, *Phys. Rev. B*, **66** (2002) 214419.
- [13] T. Mori, H. Mamiya, *Phys. Rev. B*, **68** (2003) 214422.
- [14] T. Mori, R. Sahara, Y. Kawazoe, K. Yubuta, T. Shishido, Y. Grin, *J. Appl. Phys.*, **113** (2013) 17E156.
- [15] T. Mori, T. Nishimura, *J. Solid State Chem.*, **179** (2006) 2908-2915.
- [16] T. Mori, T. Nishimura, K. Yamaura, E. Takayama-Muromachi, *J. Appl. Phys.*, **101** (2007) 093714.
- [17] T. Mori, T. Nishimura, W. Schnelle, U. Burkhardt, Y. Grin, *Dalton Trans.*, **43** (2014)15048-15054.

- [18] O. Sologub, T. Mori, *J. Phys. Chem. Solids*, **74** (2013) 1109-1114.
- [19] D. Berthebaud, T. Nishimura, T. Mori, *J. Mater. Res.*, **25** (2010) 665-669.
- [20] D. Berthebaud, T. Nishimura, T. Mori, *J. Electron. Mater.*, **40** (2011) 682-686.
- [21] T. Borkar, S. Nag, Y. Ren, J. Tiley, R. Banerjee, *J. Alloy. Compd.*, **617** (2014) 933-945.
- [22] T. Machaladze, M. Samkharadze, N. Kakhidze, M. Makhviladze, *Open J. Inorg. Chem.*, **4** (2014) 18-20.
- [23] C. Wood, D. Emin, *Phys. Rev. B*, **29** (1984) 4582-4587.

Chapter 5

Conclusion

In this thesis, we developed the three different reactive SPS processes for synthesis of $\text{MgTi}_2\text{O}_5/\text{TiN}$ composites, $\text{Y}_x\text{Al}_y\text{B}_{14}$ and $\text{YB}_{22}\text{C}_2\text{N}$. Regarding the electrical conductivity of MgTi_2O_5 , a large enhancement (>250 times) was achieved for the first time by formation of oxygen vacancies. This unprecedented electrical conductivity for MgTi_2O_5 , and the thermoelectric power factor were further remarkably improved by compositing with TiN, which yielded a conductivity enhancement of $\sim 125,000$ times. This suggests a possibility of a new kind of doping control technique for this material.

The microcracks in bulk effectively suppressed an increase of thermal conductivity. The lowest thermal conductivity was obtained for M3N10 due to lattice distortions induced by two kinds of cation disordering, $\text{Mg}^{2+}/\text{Ti}^{4+}$ and $\text{Ti}^{3+}/\text{Ti}^{4+}$. Consequently, the maximum ZT value, 0.009, was obtained for M3N10 at 773 K. While this value is still not high, forming such composites seems an effective strategy for enhancing thermoelectric properties of insulating materials considering its large enhancement of ZT compared to that of the base material, although it is likely not as straightforward to enhance materials which have high ZT to begin with.

For synthesis of dense yttrium aluminoboride, a new process with SPS and sintering additive was developed. The addition of 1 wt.% AlF_3 effectively and dramatically enhanced the sinterability and densification behavior of yttrium aluminoboride by the formation of liquid phase during SPS. Consequently, the process was remarkably simplified and total process time was shortened from ≥ 3 days to only ~ 4 -5 h.

For p-type $\text{Y}_x\text{Al}_y\text{B}_{14}$, the thermally activated conduction mechanism was proposed rather than the usually assumed variable range hopping (VRH) mechanism, to explain the experimental results of the temperature dependence of electrical conductivity and Seebeck coefficient. Conversely, the VRH mechanism appears to be a good match for the observed properties of the n-type $\text{Y}_x\text{Al}_y\text{B}_{14}$. Because of the increasing Al occupancy and thereby electron carrier content, the n-type samples have much higher conductivity, however, despite this it is indicated that the electrical carriers have some localization due to disorder. ZT values of yttrium aluminoboride prepared by reactive SPS exhibits overall similar thermoelectric properties as the previously reported best samples prepared by conventional processes. The power factor is significantly enhanced because of the high density achieved by the present discovered method. The higher thermal conductivity balances out the ZT , however, in thermoelectric research there are many methods to selectively lower the thermal conductivity. In any case, the present synthesis method that we discovered radically shortens the time necessary for synthesis, e.g. from 8 h to 5 min for the p-type sample. This breakthrough technique is expected to be able to be applied to synthesize other borides also.

For preparation of polycrystalline $\text{YB}_{22}\text{C}_2\text{N}$, a new synthesis route by reactive SPS was also developed. N_2 gas/solid reaction technology carried out at 1200°C for 30 min during SPS effectively helped the formation of the objective phase. The most homogeneous $\text{YB}_{22}\text{C}_2\text{N}$ was synthesized when it was sintered at 1700°C for 10 min after

the gas/solid reaction step, and it exhibited n-type thermoelectric behavior at low temperature. Consequently, by developing the present synthesis method, the total process steps and the whole process time required to synthesize $\text{YB}_{22}\text{C}_2\text{N}$ were dramatically shortened from ≥ 9 to only 3 steps, and from ≥ 4 days to only ~ 3 hours, respectively. This new method is expected to open the door for more effective synthesis of complex borocarbonitrides.

The present synthesis methods radically shortened the time necessary for synthesis of the objective materials, especially in borides. These breakthrough techniques are expected to be applicable to synthesize other oxide-based composites, higher borides and rare earth borocarbonitrides. Furthermore, it is also expected that the newly developed direct synthesis technique by in-situ nitridation via reactive SPS utilizing N_2 gas/solid reaction could open the door for more accessible synthesis of not only borocarbonitrides but also other nitrides.

List of Publications

1. “Thermoelectric properties of MgTi₂O₅/TiN conductive composites prepared via reactive spark plasma sintering for high temperature functional applications”

Hyoung-Won Son, Quansheng Guo, Yoshikazu Suzuki, Byung-Nam Kim, Takao Mori

Scripta Materialia, **178** (2020) 44-50.

2. “Rapid synthesis of thermoelectric YB₂₂C₂N via spark plasma sintering with gas/solid reaction technology”

Hyoung-Won Son, Philipp Sauerchnig, David Berthebaud, Takao Mori

Journal of the Ceramic Society of Japan, **128** (2020) 181-185.

3. “New Synthesis Route for Complex Borides; Rapid Synthesis of Thermoelectric Yttrium Aluminoboride via Liquid-Phase Assisted Reactive Spark Plasma Sintering”

Hyoung-Won Son, David Berthebaud, Kunio Yubuta, Akira Yoshikawa, Toetsu Shishido, Keiko Suzuta, Takao Mori

Scientific Reports (Accepted)

List of Figures

Figure 1.1. Schematic diagram of (a) a thermoelectric generator module and (b) a single thermoelectric couple. The red circle at the thermoelectric generator module indicates the single thermoelectric couple.	1
Figure 1.2. Correlations between thermoelectric properties and the charge carrier concentration. Copyright Nature Publishing Group.....	2
Figure 1.3. Literature ZT values of representative (a) p-type and (b) n-type high temperature thermoelectric materials.	4
Figure 1.4. The model for calculating the pressure in a bubble produced by surface tension and positive surface curvature.	7
Figure 1.5. The model for bubble growth. Each bubble is ideally spherical, and $r_A > r_B$	8
Figure 1.6. The conventional model which has been used to derive the chemical potential of atoms under a curved surface. In this model, atoms move from the flat surface of a semi-infinite solid to the curved surface of a spherical solid particle with a radius r	9
Figure 1.7. The seven common possible sintering mechanisms in solid-state sintering. Herein, D_g , D_s , D_{gb} , $D_{l,gb}$, $D_{l,s}$, η , and PF indicate evaporation-condensation, surface diffusion, grain boundary diffusion, lattice diffusion from grain boundary, lattice diffusion from surface, viscous flow, and plastic flow, respectively.	10
Figure 1.8. Schematic diagram of vacancy concentrations under the convex and concave surfaces. The blue and black arrows indicate vacancy flow, and diffusion of atoms and ions, respectively.	12
Figure 1.9. Schematic diagram for stages of sintering; (a) packed particles before sintering, (b) initial stage, (c) intermediate stage, and (d) final stage.	14
Figure 1.10. Schematic diagram of isolated pores positioned at (a) grain boundary, and (b) triple junction.	15
Figure 1.11. The wetting behavior for two droplets of different liquids on a horizontal solid surface with contact angle θ ; (a) good wetting with low θ , and (b) poor wetting with high θ	16
Figure 1.12. Simple model for the evolution of the microstructure during liquid phase sintering; (a) packed mixtures before sintering, (b) preliquid stage, (c) incipient liquid formation, (d) solution-reprecipitation, and (e) final stage. For this model, it is assumed that 1) the liquid phase was completely removed during sintering, 2) the sintered body is fully densified, and 3) the additive has lower melting point than particles.....	17
Figure 1.13. Flow chart of whole processes of conventional sintering (left) and reactive sintering (right).	18

Figure 1.14. Schematic diagram of (a) SPS machine and (b) mechanism during SPS.....	19
Figure 2.1. Crystal structure of $MgTi_2O_5$ (in the $Cmcm$ space group notation).....	24
Figure 2.2. Schematic diagram of $MgTi_2O_5/TiN$ conductive composites for a new type thermoelectric material.	25
Figure 2.3. XRD patterns of the $MgTi_2O_5$ (M1N0) and $MgTi_2O_5/TiN$ samples (M1N10, M1N20 and M1N30) prepared by reactive SPS at 1100°C for 10 min under a uniaxial pressure of 80 MPa in vacuum (~2-4 Pa). The TiN contents in M1N10, M1N20 and M1N30 are 10, 20 and 30 vol.%, respectively. The initial molar ratio of TiO_2/MgO of all samples is 2.00.	27
Figure 2.4. XRD patterns of the $MgTi_2O_5/10$ vol.% TiN samples sintered with various molar ratio of TiO_2/MgO . The samples were prepared by reactive SPS at 1100°C for 10 min under a uniaxial pressure of 80 MPa in vacuum (~2-4 Pa). The initial molar ratios of TiO_2/MgO of M1N10, M2N10 and M3N10 are 2.00, 2.50 and 2.67, respectively. The TiN content in all samples is fixed as 10 vol.%.	28
Figure 2.5. The observed pattern, calculated pattern, and differences between observed and calculated patterns of the XRD profiles of the M3N10 sample; (●) symbols represent the observed pattern; the black solid line represents the calculated pattern; the blue solid line represents the difference between observed and calculated patterns. The green and purple vertical bars indicate the Bragg positions of $MgTi_2O_5$ -based solid solution and TiN, respectively.	29
Figure 2.6. The temperature dependence of thermal diffusivities of sintered samples. The maximum measured temperature, 773 K is the measurement limit of the equipment.	30
Figure 2.7. The temperature dependence of thermal conductivities of sintered samples. The maximum measured temperature, 773 K is the measurement limit of the equipment.	31
Figure 2.8. The crystal structure of (a) ordered $MgTi_2O_5$, (b) disordered $MgTi_2O_5$ and (c) disordered $Mg_{1-x}Ti_{2+x}O_5$	32
Figure 2.9. The schematic diagram for phonon scattering by defects in $Mg_{1-x}Ti_{2+x}O_5$	33
Figure 2.10. SEM images of fracture surface of the $MgTi_2O_5$ and $MgTi_2O_5/TiN$ composites sintered with various TiN contents; (a, a') M1N0 (0 vol.% TiN), (b, b') M1N10 (10 vol.% TiN), (c, c') M1N20 (20 vol.% TiN) and (d, d') M1N30 (30 vol.% TiN). The arrows indicate some representative microcracks.	34
Figure 2.11. The energy balance amongst U_{tot} , U_{st} and U_{surf} . The l_{cr} indicates the critical grain size when the released elastic strain energy is equal to increased fracture surface energy.	35

Figure 2.12. SEM images of fracture surface of the sintered samples containing 10 vol.% TiN sintered with different TiO ₂ /MgO ratio; (a) M1N10 and (b) M3N10. The initial molar ratios of TiO ₂ /MgO of M1N10 and M3N10 are 2.00 and 2.67, respectively. The arrows indicate some representative microcracks.	37
Figure 2.13. The temperature dependences of electrical conductivities of MgTi ₂ O ₅ and MgTi ₂ O ₅ /TiN composites prepared by reactive SPS.	38
Figure 2.14. Temperature dependence of electrical conductivity of each sintered sample. The ln(σT) is plotted versus T^{-1} for SPH model. The straight lines for M1N0, M1N10, M3N10 and M1N20 samples indicate the fit to Eq. 2.10.	39
Figure 2.15. The temperature dependences of Seebeck coefficients of MgTi ₂ O ₅ and MgTi ₂ O ₅ /TiN composites prepared by reactive SPS.	40
Figure 2.16. Temperature dependence of Seebeck coefficient of each sintered sample. The Seebeck coefficients are plotted versus T^{-1} for SPH model.	41
Figure 2.17. The thermoelectric properties of sintered samples; (a) power factor and (b) ZT values. The ZT values were calculated from power factors and thermal conductivities up to 773 K.	42
Figure 3.1. Crystal structure of Y _x Al _y B ₁₄ , which is orthorhombic structure belonging to <i>Imma</i> space group. The boron atoms B1, B3, B4 and B5 form B ₁₂ icosahedra structures, which are interconnected via external B-B bonds or via B2 atom. Y and Al atoms partially occupy interstitial positions in the rigid three-dimensional B network.	47
Figure 3.2. Flow chart of conventional synthesis process for bulk Y _x Al _y B ₁₄ . It consists of 7 steps, and the total process time is ≥ 3 days.	48
Figure 3.3. Flow chart of newly developed synthesis process for bulk Y _x Al _y B ₁₄ in this study.	49
Figure 3.4. XRD patterns of YA0 composition (Y _{0.62} Al _{0.71} B ₁₄) samples prepared by reactive SPS without AlF ₃ addition. The samples were sintered at 1500°C under uniaxial pressure of ~30 MPa in a reduced Ar atmosphere for 1 h and 10 min, respectively. The standardized intensities for Y _x Al _y B ₁₄ and YB ₆ are shown with sample's XRD patterns.	51
Figure 3.5. XRD patterns of YA0 composition (Y _{0.62} Al _{0.71} B ₁₄) samples prepared by reactive SPS with AlF ₃ addition. The samples were sintered at 1500°C in a reduced Ar atmosphere for 1 h and 10 min under the uniaxial pressure of ~30 MPa, and for 5 min under the uniaxial pressure of 80 MPa, respectively. The standardized intensities for Y _x Al _y B ₁₄ and YB ₆ are shown with sample's XRD patterns.	52

Figure 3.6. Densification behavior of $Y_xAl_yB_{14}$ sintered without AlF_3 under ~ 30 MPa, with AlF_3 under ~ 30 MPa, and with AlF_3 under 80 MPa. To investigate the effect of AlF_3 to densification, same amount of mixture and same graphite die and spacers were used.....	53
Figure 3.7. XRD patterns of YA0, YA1, YA2 and YA3 composition ($Y_{0.62}Al_yB_{14}$; $y=0.71-1.86$) samples prepared by reactive SPS with AlF_3 addition. The samples were sintered at $1500^\circ C$ under uniaxial pressure of ~ 30 MPa in a reduced Ar atmosphere for 1 h.	54
Figure 3.8. XRD pattern and the results of Rietveld refinement of YA0-P, YA1, YA2 and YA3 samples prepared by reactive SPS with AlF_3 addition. The YA0-P sample was sintered at $1500^\circ C$ for 5 min under 80 MPa, whereas the YA1, YA2 and YA3 samples were sintered at $1500^\circ C$ for 60 min under ~ 30 MPa.....	55
Figure 3.9. Temperature dependence of logarithmic electrical conductivities of Al-poor (YA0-P) and -rich samples (YA1, YA2 and YA3) prepared by reactive SPS. The YA0-P sample was sintered at $1500^\circ C$ for 5 min under 80 MPa, whereas the YA1, YA2 and YA3 samples were sintered at $1500^\circ C$ for 60 min under ~ 30 MPa. Error bars represent a measurement uncertainty range ($\pm 7\%$).....	58
Figure 3.10. Temperature dependence of Seebeck coefficients of Al-poor (YA0-P) and -rich samples (YA1, YA2 and YA3) prepared by reactive SPS. The YA0-P sample was sintered at $1500^\circ C$ for 5 min under 80 MPa, whereas the YA1, YA2 and YA3 samples were sintered at $1500^\circ C$ for 60 min under ~ 30 MPa. The Seebeck coefficients of Al-rich samples are shown in the inset. Error bars represent a measurement uncertainty range ($\pm 7\%$).....	59
Figure 3.11. Temperature dependence of electrical conductivity of each sintered sample. The $\ln \sigma$ is plotted versus (a) T^{-1} for TAC mode and (b) $T^{-0.25}$ for VRH mode, respectively. The straight line for Al-poor sample in TAC mode expresses the fit to Eq. 1 for the temperature range from 573 K to 973 K. Also, the straight lines for Al-rich samples in TAC mode and VRH mode express the fit to Eq. 1 and to Eq. 2 for the temperature range from 373 K to 673 K, respectively.....	60
Figure 3.12. Temperature dependence of the Seebeck coefficients of all samples in accordance with (a) TAC mode and (b) VRH mode. The inset shows the Seebeck coefficients of Al-rich samples in accordance with VRH mode. The straight lines for Al-rich samples in VRH mode express the fit to Eq. 3.5 for the temperature range from 373 K to 973 K.	62
Figure 3.13. Measured densities of as-sintered $Y_xAl_yB_{14}$ ($x \sim 0.64$) samples, which are compared with the reported value of $Y_{0.56}Al_{0.57}B_{14}$. The theoretical densities of the samples prepared by reactive SPS in present study are given in Table 3.5	64

Figure 3.14. Thermal conductivities of n-type $Y_xAl_yB_{14}$ ($x \sim 0.64$) samples prepared by reactive SPS, which are compared with the reported value of $Y_{0.56}Al_{0.57}B_{14}$. Error bars represent a measurement uncertainty range ($\pm 5\%$).	65
Figure 3.15. (a) Thermal diffusivities and (b) specific heat capacities of n-type $Y_xAl_yB_{14}$ ($x \sim 0.64$) samples prepared by reactive SPS. Error bars for thermal diffusivities represent a measurement uncertainty range ($\pm 5\%$).	66
Figure 3.16. SEM images of fracture surface for $Y_xAl_yB_{14}$ samples prepared by reactive SPS, (a, a') YA0-P, (b, b') YA1, (c, c') YA2 and (d, d') YA3.	68
Figure 3.17. The result of EDX analysis on the microstructure in fracture surface of YA1. The distribution of Y, Al, B and O atoms were investigated by the mapping technique.	69
Figure 3.18. Gibbs free energy of formation of AlB_2 , B_2O_3 and Al_2O_3 with temperature range. The point positioned at the end of B_2O_3 line indicates melting temperature of B_2O_3 (723 K), and the triangle positioned at the end of AlB_2 line indicates decomposition temperature (~ 1193 K).	70
Figure 3.19. (a) Power factor and (b) figure of merits for $Y_xAl_yB_{14}$ ($x \sim 0.64$) samples prepared by reactive SPS, which are compared with the reported value of $Y_{0.56}Al_{0.57}B_{14}$	72
Figure 4.1. The crystal structure of $YB_{22}C_2N$, which is hexagonal structure belonging to $R-3m$ space group.....	76
Figure 4.2. Flow chart of conventional synthesis process for bulk $YB_{22}C_2N$. It consists of more than 9 steps, and the total process time is ≥ 4 days.	77
Figure 4.3. Flow chart of newly developed synthesis process for bulk $YB_{22}C_2N$ in this study.....	78
Figure 4.4. The sintering schedule for synthesis of $YB_{22}C_2N$ by reactive SPS.	79
Figure 4.5. The XRD patterns of the SPS1, SPS2 and SPS3 samples prepared with different nitrogen treatment temperature (T1) by reactive SPS.	80
Figure 4.6. The XRD patterns of the SPS4, SPS5, SPS2 and SPS6 samples prepared with different nitrogen treatment time (t1) by reactive SPS.	81
Figure 4.7. Displacement change of the SPS6 sample during reactive SPS. The SPS6 sample was reactively sintered at $1700^\circ C$ for 10 min after gas/solid reaction step carried out at $1200^\circ C$ for 60 min. The decrease and increase of displacement change indicate expansion and shrinkage, respectively.	82
Figure 4.8. The XRD patterns of the SPS7, SPS2 and SPS8 samples prepared with different sintering temperature (T2) by reactive SPS.	84

Figure 4.9. The XRD patterns of the SPS9, SPS10 and SPS2 samples prepared with different sintering time (t_2) by reactive SPS..... 85

Figure 4.10. (a) The amount of $YB_{22}C_2N$, B_4C and YB_6 phases, (b) the electrical conductivities, (c) Seebeck coefficients and (d) the power factors of the SPS2 and SPS5 samples..... 86

List of Tables

Table 1.1. The correlations between each mass transport mechanism and densification behavior in solid-state sintering. The routes for each mass transport mechanism are illustrated in Fig. 1.7	13
Table 2.1. Coefficients of thermal expansion (CTE) of pseudobrookite-type MgTi_2O_5 , shown within <i>Cmcm</i> (63) space group.....	25
Table 2.2. Initial molar ratio of TiO_2/MgO and TiN content of each sample.	26
Table 3.1. The synthesis conditions of $\text{Y}_x\text{Al}_y\text{B}_{14}$ samples.	56
Table 3.2. Compositions and lattice parameters of sintered samples, which were estimated from Rietveld analysis.	56
Table 3.3. Phase fraction of constituent phases of each sample. Both are estimated by Rietveld refinement.	57
Table 3.4. T_0 and $\sigma_{0,VRH}$ values of Al-rich samples, which are calculated from the linear fitted lines for $\ln\sigma$ versus $T^{-0.25}$ plots.....	63
Table 3.5. Phase fraction of constituent phases and theoretical and relative density of each sample. Both are estimated by Rietveld refinement.	65
Table 3.6. Standard molar enthalpies of formation and standard molar entropies at 298 K.	69
Table 3.7. Gibbs free energy of formation changes accompanied by each reactions.....	70
Table 4.1. Lattice parameters and measured densities of the SPS2 and SPS5 samples prepared by reactive SPS... ..	83